

# **The Micro and Nano Scale Characterization and Identification of Tablet Formulations**

**Zheng Jin Bsc., Msc.**

**Thesis submitted to the University of Nottingham for the degree  
of Doctor of Philosophy, September 2009**

## **Acknowledgement**

I would like to thank my supervisors: Prof. Clive Roberts and Prof. Martyn Davies for their continuous guidance and advice during the whole project and the writing period. I want to thank my industry supervisor Dr. Steve Cosgrove from AstraZeneca for providing experiment materials and opportunities to use the NIR and ATR-IR instruments in Charnwood. I thank the University of Nottingham and AstraZeneca for funding this project.

I wish to acknowledge all the members in LBSA who have been supporting and helping me during the project. I thank Prof. Xinyong Chen for the instructions on AFM and other instruments, Dr. Barry Crean for instructions on colloid probe preparation, Dr. David Scurr for experiments with ToF-SIMS, Mischa Zelzer for instructions on plasma polymerize coating and Michael Taylor for instructions on contact angle measurements.

Finally, I need to acknowledge my family for their support all the time. I would like to thank my wife Ji Li for her understanding and help during the time in UK.

## **Abstract**

The aim of this project was to characterize the surface properties of materials used in tablet formulations with sub-micron resolution by the techniques of Atomic Force Microscopy (AFM), Scanning Electron Microscopy (SEM), Scanning Thermal Microscopy (SThM), Nano-TA system, Differential Scanning Calorimeter (DSC), Attenuated Total Reflectance Infrared (ATR-IR), Near-Infrared Spectroscopy (NIR) and Time-of-Flight Secondary Ion Mass Spectrometry (ToF-SIMS). In particular, the work aimed to develop new AFM based methodologies to advance this method both in terms of quantification and mapping. AFM was employed to investigate properties of solid materials such as surface free energy, Young's modulus, melting point and phase transition temperatures from pharmaceutical materials in blend mixtures with the nanoscale resolution. These approaches developed here provide new tools to understand the process induced changes and stability issues in solid dosage forms such as tablets and inhalation formulations from minute amounts of materials.

The surface free energy values of solid materials obtained from AFM adhesion force measurements were described in Chapter 3. The adhesion forces obtained with AFM in low relative humidity environments were used to derive the surface free energy values using the Hertzian and JKR based models. The

surface free energy was proposed to be close to the so called dispersion surface free energy since the adhesion forces at low relative humidity mainly resulted from van der Waals forces in the systems studied here. The comparison of surface free energy between AFM and those derived from a contact angle method showed that the dispersion surface free energy values derived from the contact angle method were generally higher than those from AFM. For example, the surface free energy value derived from AFM adhesion force measurements for lactose monohydrate was  $33.0 \text{ mJ/m}^2$ , while from contact angle method the value was  $46.8 \text{ mJ/m}^2$ . Whilst in reasonable agreement, the variation was believed to result from the differences in probe substance (liquid in contact angle and solid in AFM method), scale of measurements (contact area  $200 \text{ nm}^2$  in AFM, several  $\text{mm}^2$  in contact angle) and possible polar interactions. However, the surface free energy values derived from direct solid-solid interactions in AFM adhesion force measurements may have more relevances in applications that relate to solid-solid interactions, such as in pharmaceuticals.

The influence of polar interaction in AFM adhesion force measurements at low relative humidity was further investigated in Chapter 4. The techniques of colloid probe and plasma polymerized coating were employed: Plasma polymerized hexane and allylamine were coated on the surfaces of glass beads mounted on AFM cantilevers. Plasma Polymerized Hexane had only a

dispersion surface free energy while plasma polymerized allylamine had both dispersion and polar surface free energy components. The differences in normalized adhesion forces between these two kinds of colloid probes can reveal the influence of polar interactions at low relative humidity in AFM adhesion force measurements. For most samples, the experimental adhesion forces with plasma polymerized allylamine colloid probes were smaller than the theoretical values calculated from dispersion interactions. The polar interactions in such conditions were repulsive so they had decreased the experimental adhesion forces. So in AFM adhesion force measurements, the polar interactions existed even at very low humidity. However the relative magnitude of polar interactions were smaller than the dispersion interactions and for silicon sample the polar interactions were negligible.

In Chapter 5, properties including Young's modulus, melting points and phase transition temperature were measured at the nanoscale with AFM, SThM and the nano-TA system. The variation of Young's modulus with temperature, for the excipients hydroxypropylmethylcellulose (HPMC), dibasic calcium phosphate dihydrate (DCPD) was studied. The differences in Young's modulus between DCPD and its anhydrous form were revealed with AFM measurements. The melting point and phase transition temperature were measured by nano-TA system with sub-100 nm spatial resolution. The thermal properties obtained from nano-TA system were consistent with those from bulk

measurements using DSC: e.g. the dehydration of lactose monohydrate (150 °C) was confirmed by nano-TA system and DSC measurements.

In Chapter 6, the methods to derive surface free energy and thermal properties described in previous chapters were employed to spatially locate and characterize an API (AZD 3409 malate salt) and excipient (lactose monohydrate) on the surface of a model tablet at the nanoscale using AFM and the nano-TA system. The API and excipient were mixed with the ratio of 20:80, 50:50 and 80:20 w/w and compressed into discs to create the model tablets. The surfaces of model tablets were first characterized by ATR-IR, NIR and ToF-SIMS. Then AFM adhesion force measurements were carried out to map the location of each component in the mixed discs. In addition, in situ topography AFM images of the discs were recorded. At the position of force mapping, the nano-TA system was employed to correlate the thermal properties including the melting points of both materials and the dehydration of the lactose monohydrate with surface free energy information from force mapping. The surface free energy and thermal properties data were consistent with bulk measurements in previous chapters. In situ correlation between AFM force mapping (surface energy) and nano-TA system (thermal properties) at 5 different positions on a model disc surface showed consistent identification of the two materials. This proof of principal work can be extended to more complex formulations and has the potential to be employed in early stage solid

state stability testing to identify the appearance of new species at surfaces or solid-solid interfaces.

# Contents

Contents .....	1
List of Figures .....	6
List of Tables .....	20
Chapter 1: Introduction.....	22
1.1 Surface Forces and Surface Free Energy .....	24
1.1.1 The Origins of Surface Free Energy .....	25
1.1.2 Surface Free Energy from Contact Angle Measurements .....	28
1.1.3 Surface Free Energy from Solid Adhesion Measurements.....	33
1.2 Mechanical Properties of Pharmaceutical Materials .....	36
1.2.1 Contact Theory Modified with Material Mechanical Properties.	39
1.2.2 Young's Modulus Measurements with the Indentation Method ..	41
1.3 The Applications of AFM Imaging and Force Measurements in Pharmaceutical Applications .....	43
1.3.1 The AFM System.....	44
1.3.2 The Applications of AFM Imaging to Pharmaceutical and Biopharmaceutical Research .....	45
1.3.2 The Applications of AFM Local Force Measurements.....	49
1.4 Solid State Surface Characterizations in Pharmaceutical Applications .....	57
1.4.1 Attenuated Total Reflection Infrared (ATR-IR) and Near Infrared (NIR) Spectroscopy .....	58

1.4.2 Time-of-Flight Secondary Ion Mass Spectrometry (ToF-SIMS)	61
1.5 Thermal Properties and Thermal Measurements on Solid Pharmaceutical Materials	64
1.6 Aims of the Thesis	69
References	70
Chapter 2: Materials and Methods	91
2.1 Materials	91
2.1.1 Samples for AFM Surface Free Energy and Mechanical (Young's modulus) Measurements	92
2.1.2 Samples for Contact Angle Measurements	92
2.1.3 Lactose Recrystallization for Nano-Thermal Analysis	92
2.1.4 Model Formulation for AFM Adhesion Force Mapping and Nano-Thermal Analysis	93
2.2 Atomic Force Microscopy	93
2.2.1 AFM Imaging	95
2.2.2 AFM Force Measurements	97
2.3 Nano-Thermal Analysis	100
2.4 Contact Angle Measurements	102
2.5 Infrared Spectroscopy	104
2.6 Other Complementary Characterization Methods	106
2.6.1 SEM Imaging and Image Analysis	106
2.6.2 DSC Thermal Measurements	106

2.6.3 ToF-SIMS Chemical Mapping.....	107
References .....	108
Chapter 3: Solid Surface Free Energy Measurements with AFM Adhesion Force and Contact Angle Methods .....	111
3.1 Introduction .....	111
3.2 Materials and Methods .....	111
3.3 Results and Discussions.....	115
3.3.1 AFM Sample Tapping Imaging and Roughness Analysis .....	115
3.3.2 AFM Adhesion Force Measurements on APIs and Excipients..	118
3.3.3 Surface Free Energy from AFM Force Measurements.....	121
3.3.4 Surface Free Energy Measured via Contact Angle Measurements .....	124
3.3.5 Surface Free Energy Comparison between AFM Adhesion Force Measurements and Contact Angle measurements .....	128
3.4 General Conclusions.....	132
References .....	134
Chapter 4: Colloid Probe AFM Forces Measurements on APIs and Excipients .....	138
4.1 Introduction .....	138
4.2 Materials and Methods .....	139
4.3 Results and Discussions.....	143
4.3.1 SEM and AFM Reverse Images of Colloid Probes .....	143

4.3.2 Uncoated Colloid Probes Adhesion Forces Measurements and Surface Energy Calculation .....	146
4.3.3 Plasma Polymer Coated Glass Beads Colloid Probes Adhesion Forces Measurements and Surface Free Energy Calculations.....	149
4.4 General Conclusions.....	163
References .....	166
Chapter 5: Nanoscale Mechanical (Young's modulus) and Thermal Properties Characterization of Formulation Components .....	168
5.1 Introduction .....	168
5.2 Materials and Methods .....	168
5.3 Results and Discussions.....	173
5.3.1 Young's Modulus Measurements on Materials Used for Tablet Formulation .....	173
5.3.2 HPMC and DCPD Young's Modulus with Temperature.....	175
5.3.3 Materials Melting Points Determined with SThM and Nano-TA System .....	180
5.3.4 Lactose Monohydrate Dehydration and Rehydration Study with the Nano-TA System.....	187
5.4 General Conclusions.....	189
References .....	191
Chapter 6: Surface Energy and Thermal Nanoscale Characterization and Mapping of a Model Solid Formulation.....	195

6.1 Introduction .....	195
6.2 Materials and Methods .....	197
6.3 Results and Discussions.....	199
6.3.1 Characterization of Model Binary Mixtures Discs.....	199
6.3.2 Force Mapping on a Binary Model Formulation.....	213
6.3.3 Thermal Mapping on a Binary Model Formulation .....	219
6.3.4 Force and Thermal Correlation Mapping on a Binary Model Formulation .....	223
6.4 General Conclusions.....	227
References .....	229

## List of Figures

Figure 1.1 Contact angle ( $\theta$ ) formation of liquid droplet in gas on solid surface.....	29
Figure 1.2 Contact angle goniometer (KSV CAM 200) used in the LBSA (image from KSV website).....	31
Figure 1.3 A Schematic representation of the two big rigid spheres located at a distance of D.....	34
Figure 1.4 The geometry of the contact between a sphere and a flat surface. F is the applied loading force.....	39
Figure 1.5 Schematic of basic AFM operation and real micro-cantilever and components [88].....	45
Figure 1.6 Visualization of the interaction between linear DNA and PprA protein by AFM [100]. The arrows represent the end and internal bound PprA proteins.....	46
Figure 1.7 A SEM image of a carbon nanotube tip attached to a standard AFM tip.....	47
Figure 1.8 An AFM image of spherical aggregates and fibril structure in 0.25% concentration gelatin [107].....	48
Figure 1.9 AFM images of AmpB prepared in (A) Peceol alone (B) Peceol/DSPE-PEG2000. Droplets applied to the substrate exhibit phase separation of components in (A) but not in (B) [108].....	48
Figure 1.10 A representative force distance curve. From positions 1 to 2,	

the tip is approaching the surface, and at position 2 contact is made. From positions 2 to 3, the cantilever bends until it reaches the specified force limit that is to be applied; it is then withdrawn during positions 4 and 5. At position 5, the tip loses contact with the surface but the adhesion force between tip and surface still bends the cantilever until at position 6 where the adhesion force becomes “zero”. From positions 6 to 7, the cantilever returns to its resting position and ready for another measurement..... 50

Figure 1.11 A schematic image of asperities effect of contact geometry on rough probe and surface..... 51

Figure 1.12 An AFM image of dibasic calcium phosphate dihydrate, scan size 5  $\mu\text{m}$  (Left). And a SEM image of dibasic calcium phosphate dihydrate (Right)..... 52

Figure 1.13 A schematic image of attenuated total reflection of infrared radiation through the transmitting crystal. .... 58

Figure 1.14 NIR chemical mapping of one API (left) and cellulose (right) on one model tablet showed the position of high density domains of substrates [139]..... 60

Figure 1.15 A schematic diagram of the ToF-SIMS instrument (D.W. Mogk Montana State University)..... 62

Figure 1.16 Distribution maps of rapamycin (yellow) and PLGA (blue) in eluting coatings at the depth of 22 nm (left) and 33 nm (right) [144]..... 63

Figure 1.17 A schematic diagram of SThM thermal probe..... 67

Figure 1.18 A SEM image of thermal probe used in the Nano-TA system  
(image from Anasys Instruments <http://www.anasysinstruments.com/>).68

Figure 2.1 A simple illustration of the main components of AFM. The  
detector records the changes of laser spot which caused by the  
movement of probes while the piezo scanner scans over the sample  
surface. In this manner, a representation of surface topography in X, Y  
and Z directios will be generated by computer..... 94

Figure 2.2 SEM image and Schematic of contact mode V-shape (left)  
and tapping mode cantilever (right) (images from Veeco  
<http://www.veecoprobes.com/>)..... 97

Figure 2.3 Schematic of a deflection signal versus piezo scanner  
position curve. The AFM probe approaches to the surface from position  
1 and contacts to the surface at position 2. The probe shall keep pushing  
to pre-set loading force and retreat from position 3. The adhesion forces  
between probe and surface pull the cantilever even after initial contact  
position 2 until the adhesion can not hold the cantilever at position 5.. 97

Figure 2.4 A schematic force-distance curve converted from deflection  
signal versus piezo scanner position curve in Figure 2.3. The AFM probe  
approaches to the surface from position 1 and contacts to the surface at  
position 2. The probe shall keep pushing to pre-set loading force and  
retreat from position 3. The adhesion forces between probe and surface

pull the cantilever even after initial contact position 2 until the adhesion can not hold the cantilever at position 5..... 99

Figure 2.5 SEM images of Nano-TA2 system AN-2 thermal probe cantilever and tip (images from Anasys Instruments <http://www.anasysinstruments.com/nano-TA2.pdf>). ..... 102

Figure 3.1 A schematic diagram of probe penetration depth determination. Regardless of probe deformation, the depth is also considered to be probe indentation ( $\delta$ ) [3]. ..... 113

Figure 3.2 A schematic diagram of contact region radius R determination based on spherical probe in contact with deformable plane surface. r is the radius of a circular plane at the cross section of the tip when sample deforms to its maximum extent. A is the area of the circular plane and  $\delta$  is the probe indentation. R is the contact region radius [3]. ..... 114

Figure 3.3 AZD 3409 Hcl salt form AFM tapping images. Both images have the scan size: 1  $\mu\text{m}$  x 1  $\mu\text{m}$ . ..... 116

Figure 3.4 AZD 3409 malate salt form AFM tapping images. Both images have the scan size: 1  $\mu\text{m}$  x 1  $\mu\text{m}$ . ..... 117

Figure 3.5 Lactose monohydrate tapping image. The scan size is 1  $\mu\text{m}$  x 1  $\mu\text{m}$ . ..... 117

Figure 3.6 Dibasic calcium phosphate dehydrate tapping image. The scan size is 1  $\mu\text{m}$  x 1  $\mu\text{m}$ . ..... 117

Figure 3.7 Magnesium stearate tapping image. The scan size is 1  $\mu\text{m}$  x

1 $\mu$ m. ....	118
Figure 3.8 Lactose monohydrate original data: a T-B deflection signal versus relative Z displacement curve collected from a multimode AFM with a FESP probe.....	120
Figure 3.9 Processed data: the force versus relative Z displacement curve from original data Figure 3.8. ....	120
Figure 3.10 Processed data: the force versus tip-sample distance curve from original data Figure 3.9. ....	121
Figure 3.11 A schematic diagram of TGT1 grating. The period is 3 $\mu$ m and diagonal period is 2.12 $\mu$ m. The tip angle is about 30 degrees....	122
Figure 3.12 The FESP probe reverse image which generated by scanning over the TGT1 grating. The 3D view of left image is generated by the SPIP.....	123
Figure 3.13 The plot of water contact angle versus time to acquire contact angle of water on HPMC surface at 0 second.....	125
Figure 4.1 A schematic illustration of the plasma coating machine used to functionalize the AFM colloidal probes.....	142
Figure 4.2 SEM images of colloid probes without Au coating: (a) a contact mode AFM probe with a glass bead glue on the end of cantilever (R=9.5 $\mu$ m). (b) a tapping mode AFM probe with a glass bead glue on the end of cantilever (R=9.7 $\mu$ m).....	144
Figure 4.3 SEM images of colloid probes: (a) a tapping mode AFM probe	

with a glass bead glue on the end of cantilever ( $R=10.1 \mu\text{m}$ ). (b) a tapping mode AFM probe with a glass bead glue on the end of cantilever ( $R=9.6 \mu\text{m}$ )..... 145

Figure 4.4 AFM reverse image method on colloid probes. AFM height images of an uncoated colloid probe after several forces measurements (Left) and a plasma polymer hexane coated colloid probe after several forces measurements (Right)..... 146

Figure 4.5 Tapping images of thickness measurement with AFM scratching method on plasma polymer hexane (Left) and average lines profiles function in SPIP (Right)..... 151

Figure 4.6 Tapping images of thickness measurement with AFM scratching method on plasma polymer allylamine (Left) and average lines profiles function in SPIP (Right). ..... 151

Figure 4.7 Tapping topography images of plasma polymer hexane on glass slide (left)  $5 \times 5 \mu\text{m}^2$ , plasma polymer allylamine on glass slide (right)  $5 \times 5 \mu\text{m}^2$ ..... 152

Figure 4.8 Graphic illustration of the relative magnitude of adhesion forces for each sample obtained from plasma polymer hexane colloid probes force measurements. .... 155

Figure 4.9 Graphic illustration of the relative magnitude of adhesion forces for each sample obtained from plasma polymer allylamine colloid probes force measurements. .... 155

Figure 4.10 Comparison plots of dispersion forces which are derived from dispersion surface free energy and radius of each colloid probe and adhesion forces (dash dot line) which are obtained from colloid probe adhesion force measurements. .... 160

Figure 4.11 FESP probes comparison plots of dispersion forces which are derived from dispersion surface free energy and radius of each colloid probe and adhesion forces (dash dot line) which are obtained from colloid probe adhesion force measurements. .... 161

Figure 5.1 SEM images of top view of the SThM probe cantilever and thermal element and magnified view of the thermal element [4]..... 172

Figure 5.2 SEM images of the AN-2 thermal probe used in nano-TA system and magnified view of the sharp probe (images from Anasys Instruments)..... 172

Figure 5.3 The plot of E versus temperature results on HPMC.  $T_g$  temperature for HPMC is 120 °C..... 176

Figure 5.4 Force-distance curves of HPMC at room temperature (left) and high temperature 140 °C (right). At high temperature, the retract force-distance curve is not applicable for linear gradient determination. .... 178

Figure 5.5 SEM images of DCPD (left) and ACP (Right) samples used in Young's modulus measurements. .... 179

Figure 5.6 A SThM local thermal analysis plot on AZD 3409 HCl salt. The

melting point in the plot is 205.8 °C. ....	181
Figure 5.7 A SThM local thermal analysis plot on AZD 3409 malate salt. The melting point in the plot is 199.3 °C. ....	181
Figure 5.8 A tapping mode image of a hole which nano-TA local thermal analysis made on lactose monohydrate surface. The radius of the hole is 219 nm as measured by Nanoscope (V7.0) Section function. ....	184
Figure 5.9 A nano-TA local thermal analysis plot of lactose monohydrate. There are two peaks in the plot. The first peak is the dehydrate temperature at 160.7 °C. And the second peak is the melting temperature at 207.5 °C. ....	184
Figure 5.10 A DSC plot of lactose monohydrate. The first peak is the crystal dehydration onset temperature at 145.15 °C and the second peak is the melting onset temperature at 207.92 °C. ....	186
Figure 5.11 A DSC plot of DCPD. The first peak is the crystal dehydration temperature at 103.08 °C and the second peak is the melting temperature at 177.21 °C. ....	186
Figure 5.12 Three local thermal analysis plots on re-crystallized lactose monohydrate crystal surface with nano-TA system. The first peak is at a temperature of around 150 °C and is related to dehydration and the second peak is at a temperature of around 185 °C for the melting point. .....	187
Figure 5.13 Nano-TA local thermal analysis to confirm the dehydration of	

lactose monohydrate: the upper curve is the first measurement stopped at the dehydrate point (138 °C) and the lower curve is the followed measurement at the same position.....	188
Figure 5.14 Nano-TA local thermal analysis to confirm the rehydration of lactose monohydrate: the upper curve is the first measurement stopped at the dehydrate point (154 °C) and the lower curve is the followed measurement after 50 minutes at the same position. Dehydration point (150 °C) and melting point (209 °C) can be observed.....	189
Figure 6.1 ATR-IR spectra of AZD 3409 malate salt powder and compressed disc. The comparison between the two spectra shows that there are no changes of chemical components during the compression processes.....	200
Figure 6.2 ATR-IR spectra of lactose monohydrate powder and compressed disc. The comparison between two spectra shows that there are no changes of chemical components during the compression processes.....	201
Figure 6.3 Spectra math spectrum (red) and actual ATR-IR average spectrum from 5 measurements on 80: 20 w/w binary mixtures disc..	202
Figure 6.4 Spectra math spectrum (red) and actual ATR-IR average spectrum from 5 measurements on 50: 50 w/w binary mixtures disc..	202
Figure 6.5 Spectra math spectrum (red) and actual ATR-IR average spectrum from 5 measurements on 20: 80 w/w binary mixtures disc..	203

Figure 6.6 the NIR chemical images (1x1 mm<sup>2</sup>) of a simple mixed compressed 50:50 w/w disc. Left map is the spectra correlated by AZD 3409 malate salt standard NIR spectrum. Right is the spectra correlated by lactose monohydrate standard NIR spectrum. .... 205

Figure 6.7 The NIR chemical images (1x1 mm<sup>2</sup>) of a slurry mixed compressed 80:20 W/w of AZD 3409 malate salt: lactose disc. Left image is the spectra correlated by AZD 3409 malate salt standard NIR spectrum. Right is the spectra correlated by the lactose monohydrate standard NIR spectrum. .... 205

Figure 6.8 The NIR chemical images (1x1 mm<sup>2</sup>) of a slurry mixed compressed 50:50 W/w of AZD 3409 malate salt: lactose disc. Left image is the spectra correlated by AZD 3409 malate salt standard NIR spectrum. Right is the spectra correlated by the lactose monohydrate standard NIR spectrum. .... 206

Figure 6.9 The NIR chemical images (1x1 mm<sup>2</sup>) of a slurry mixed compressed 20:80 W/w of AZD 3409 malate salt: lactose disc. Left image is the spectra correlated by AZD 3409 malate salt standard NIR spectrum. Right is the spectra correlated by the lactose monohydrate standard NIR spectrum. .... 206

Figure 6.10 ToF-SIMS 80:20 w/w simple mixed compressed disc distribution maps. Top four positive ions distribution maps: AZD 3409 malate salt, lactose monohydrate, total ion and cross distribution.

Bottom four images are negative ions distribution maps.....	210
Figure 6.11 ToF-SIMS 80:20 w/w slurry mixed compressed disc distribution maps. Top four positive ions distribution maps: AZD 3409 malate salt, lactose monohydrate, total ion and cross distribution. Bottom four negative ions distribution maps. ....	210
Figure 6.12 ToF-SIMS 50:50 w/w simple mixed compressed disc distribution maps. Top four positive ions distribution maps: AZD 3409 malate salt, lactose monohydrate, total ion and cross distribution. Bottom four images are negative ions distribution maps.....	211
Figure 6.13 ToF-SIMS 50:50 w/w slurry mixed compressed disc distribution maps. Top four positive ions distribution maps: AZD 3409 malate salt, lactose monohydrate, total ion and cross distribution. Bottom four images are negative ions distribution maps.....	211
Figure 6.14 ToF-SIMS 20:80 w/w simple mixed compressed disc distribution maps. Top four positive ions distribution maps: AZD 3409 malate salt, lactose monohydrate, total ion and cross distribution. Bottom four images are negative ions distribution maps.....	212
Figure 6.15 ToF-SIMS 20:80 W/w slurry mixed compressed disc distribution maps. Top four positive ions distribution maps: AZD 3409 malate salt, lactose monohydrate, total ion and cross distribution. Bottom four images are negative ions distribution maps.....	212
Figure 6.16 Tapping topography and phase images of 50:50 w/w slurry	

compressed disc with FESP probe before force measurements. Scan size is $10 \times 10 \mu\text{m}^2$ .....	213
Figure 6.17 Surface free energy measurements on pure AZD 3409 malate salt and lactose monohydrate discs. 100 surface free energy values were derived from the force-distance curves of each sample. The values were plotted as histogram. The average surface free energy values for AZD 3409 malate salt is $10.7 (2.2) \text{ mJ/m}^2$ ; for lactose monohydrate is $38.6 (11.2) \text{ mJ/m}^2$ .....	214
Figure 6.18 Force map on 50:50 w/w slurry compressed disc. The scan size of tapping topography image is $10 \times 10 \mu\text{m}^2$ and the scan size of force measurements is $5 \times 5 \mu\text{m}^2$ . Each position was classified into the two materials present based on its surface free energy value. ....	215
Figure 6.19 Force map of 80:20 w/w slurry compressed disc. Scan size is $10 \times 10 \mu\text{m}^2$ and scan size of force measurements is $5 \times 5 \mu\text{m}^2$ . 100 force measurements were collected.....	216
Figure 6.20 Force map of 50:50 w/w slurry compressed disc. Scan size is $10 \times 10 \mu\text{m}^2$ and scan size of force measurements is $5 \times 5 \mu\text{m}^2$ . 100 force measurements were collected.....	216
Figure 6.21 Force map of 20:80 w/w slurry compressed disc. Scan size is $10 \times 10 \mu\text{m}^2$ and scan size of force measurements is $5 \times 5 \mu\text{m}^2$ . 100 force measurements were collected.....	217
Figure 6.22 Tapping topography image of 20:80 w/w slurry disc with	

AN-2 thermal probe before thermal measurements. The single particle which is going to be measured is marked..... 220

Figure 6.23 Tapping topography image of a 20:80 w/w slurry disc with an AN-2 thermal probe after thermal measurement. The hole made by thermal measurement can be seen. The corresponding LTA trace is presented as Figure 6.24..... 220

Figure 6.24 Nano-TA local thermal analysis on the single particle circled in figure 6.22. The melting point temperature is 123.2 °C which indicates the single particle is the AZD 3409 malate salt (See table 5.4)..... 221

Figure 6.25 Tapping topography images before (Left) and after (Right) thermal measurements. Nano-TA local thermal analysis show that single particle with red circle is AZD 3409 malate salt (Figure 6.26), while position with light turquoise circle is lactose monohydrate (Figure 6.27).  
..... 222

Figure 6.26 Nano-TA local thermal analysis on the particle with red circle. The melting point temperature is 113.2 °C for AZD 3409 malate salt. 222

Figure 6.27 Nano-TA local thermal analysis on the position with light turquoise circle. The melting point temperature is 161.2 °C. While the dehydrate point temperature is found at 106.4 °C..... 223

Figure 6.28 AFM tapping topography image of 20:80 w/w slurry disc with a FESP probe. The marker hole was made with nano-TA thermal measurement early for easy position relocation with tapping imaging. 5

positions were measured with AFM force measurements.....	224
Figure 6.29 AFM tapping topography image of 20:80 slurry disc with AN-2 Thermal probe. 5 positions were measured with Nano-TA local thermal analysis. ....	225
Figure 6.30 Nano-TA local thermal analysis measurements on 5 positions. At position No.1 dehydration temperature is 141.8 °C, melting temperature is 190.8 °C. At position No.2 dehydration temperature is 111.3 °C, melting temperature is 167.6 °C. At position No.3 dehydration temperature is 152.8 °C, melting temperature is 195.3 °C. At position No.5 dehydration temperature is 149.9 °C, melting temperature is 189.4 °C. At position No. 4 only melting temperature was observed at 113.4 °C. ....	226

## List of Tables

Table 3.1 Root Mean Square (RMS) roughness values for APIs and excipients .....	116
Table 3.2 Adhesion Forces for APIs and Excipients (n=50) ..	121
Table 3.3 Surface free energy of APIs and Excipients .....	124
Table 3.4 Surface free energy and its components values of each liquid probe used in contact angle measurements	Unit: mJ/m <sup>2</sup> ..... 126
Table 3.5 Contact angle results of three liquids on samples (N=5)	Unit: ° 126
Table 3.6 Sample surface free energy (dispersive and polar component) results derived from the Wu's equation	Unit: mJ/m <sup>2</sup> 错误! 未 定义书签。
Table 3.7 Comparison of literature values of sample surface free energy and contact angle experiment results	Unit: mJ/m <sup>2</sup> ..... 127
Table 3.8 Comparison of surface free energy results derived contact angle experiment and AFM adhesion force measurements	Unit: mJ/m <sup>2</sup> ..... 132
Table 4.1 Adhesion Forces and Surface Energy Results from Uncoated Glass Beads Probes	(N=50) ..... 147
Table 4.2 Contact Angle and Surface Free Energy Results of Plasma Polymer Hexane and Allylamine .....	149

Table 4.3 RMS roughness results of plasma polymer hexane and allylamine	152
Table 4.4 Adhesion forces measurements (AD) on samples with plasma polymer hexane coated probes	Unit: nN (N=9) ..... 153
Table 4.5 Adhesion forces measurements (AD) on samples with plasma polymer allylamine coated probes	Unit: nN (N=9) 153
Table 4.6 Surface free energy values of samples derived from hexane coated colloid probes and FESP probes	Unit: mJ/m <sup>2</sup> ..... 156
Table 4.7 Roughness (RMS) values of samples for colloid probe forces measurements	Unit: nm ..... 157
Table 4.8 Theoretic adhesion forces calculated with dispersion surface free energy derived form hexane coated colloid probes and radii of allylamine coated colloid probes and FESP probes from reverse images.	Unit: nN ..... 159
Table 5.1 Young's modulus values derived from retreat curves with AFM FESP probes.....	174
Table 5.2 Young's modulus of HPMC before and after heating and Young's modulus at T <sub>g</sub> Temperature.....	176
Table 5.3 Young's modulus values of DCPD before and after dehydration...	179
Table 5.4 Melting points of materials from nano-TA system local thermal	

analysis .....	182
Table 5.5 Melting points of materials measured by DSC method (onset temperature).....	185
Table 6.1 Ion list for AZD 3409 malate salt used in ToF-SIMS material identification.....	208
Table 6.2 Ion list for lactose monohydrate used in ToF-SIMS material identification.....	209
Table 6.3 Surface free energy values in Figure 6.25 5 measure positions.....	224

## **Chapter 1: Introduction**

In pharmaceutical applications, the characterizations of drugs and excipients are the priority in formulation and subsequent stability testing [1-2]. The properties of raw materials such as particle size, porosity, density and the mechanical properties as well as chemical purity concerning safety and efficacy are not only used as quality control parameters to restrict the batch to batch differences but are also involved in the final products performances both *in vivo* and *in vitro* [3-4]. The characterization of individual compounds usually starts based on either bond or molecular vibration in the electromagnetic spectrum (IR, NIR, Raman) or the weight-charge ratio in the Mass Spectrometry (MS). In stability tests, the physical and chemical changes within a range of temperatures and humidities are explored with time. The appearances of heterogeneities on a surface due to such stress conditions may be detectable with surface characterization methods [5-6]. With the increasing use of nanotechnology in formulation, the demands for sub-micron characterization are increasing. Hence, microscopy and spectroscopy techniques have been introduced to carry out the material characterization with sub-micron or even higher spatial resolutions. For example, the high resolution topography images, materials distribution and mechanical measurements on single particles have been widely used in the pharmaceutical, biological and

medical applications [7-10]. In another example, the formulation of dry powder inhalers, the interactions between the sub-micron size drug and the carrier particles can only be directly monitored by Atomic Force Microscopy (AFM) [11]. It should be noted that parameters obtained from single particle measurements including surface free energy, Young's modulus and melting point temperature are not always consistent with the results from traditional bulk methods [12]. So it is wise to use those parameters obtained from single particle measurements but not the bulk results for those applications where the small particles interactions are dominant and to use the insights from both approaches in a complementary fashion. In this chapter, the basic concepts and principals of techniques used in the thesis will be discussed from the aspect of solid-solid interactions.

## **1.1 Surface Forces and Surface Free Energy**

Surface free energy ( $\gamma$ ) which is usually defined as the work required to increase the area of a substance by one unit is also termed surface tension as the force along a line of unit length [13]. This kind of force (energy) creates various phenomena in everyday life, like wetting, adsorption and adhesion. One classic example is the shape of a drop of liquid in air (or another immiscible liquid) that tends to be spherical when gravity is absent. Because the shape of a sphere has the smallest ratio of surface area to volume, the work

required to create a new surface is at a minimum [14]. From this example, the origins of surface free energy can also be noticed. The surface free energy must come from the intermolecular forces which help hold the liquid together [15]. In the view of molecular motion, the forces which attract them together in the bulk also act at the surface. But the molecules on the outside gas phase are relatively fewer than the bulk. So the molecules at the surface are pulled into the bulk by the forces towards at the center of mass, minimizing the ratio of surface area to volume.

### **1.1.1 The Origins of Surface Free Energy**

As mentioned above, surface free energy should come from the intermolecular forces. The intermolecular forces are essentially electrostatic in origin so the forces are classified based on fundamental origin as ionic bands (or metallic bands), van der Waals forces and hydrogen bonds [16].

Ionic bonds between two charged atoms (ions) originate from Coulomb forces which are the strongest of the physical forces - stronger than most covalent (chemical) forces. The free energy for Coulomb interaction between two charges  $Q_1$  and  $Q_2$  is in Equation 1.1,

$$w(r) = \frac{Q_1 Q_2}{4\pi\epsilon_0 \epsilon r} \quad \text{Equation 1.1}$$

Where  $\epsilon$  is the relative permittivity of the medium and  $r$  is the distance between

the two charges. The Coulomb force  $F$  is given by Equation 1.2,

$$F = -\frac{dw(r)}{dr} = \frac{Q_1 Q_2}{4\pi\epsilon_0 \epsilon r^2} \quad \text{Equation 1.2}$$

The Coulomb force thus is very strong and of long range which is manifested in the  $\frac{1}{r^2}$  distance dependence of  $w(r)$ .

Van der Waals forces, unlike Coulomb forces act between all atoms and molecules, even neutral ones like helium and hydrocarbons. In some cases, van der Waals forces are also named as dispersion forces. The term “dispersion” comes from the work of London [17], so London dispersion force is also used in literature [18]. Good [19] further stated that the term of dispersion should be replaced with London since the dispersion is not related with intermolecular forces but a variation of refractive index. After all the dispersion forces, which are not dependant on the properties of molecules, are the most important contribution to the van der Waals force.

The first contribution to the total van der Waals force is the electrostatic interaction between charges, dipoles, quadrupoles and in general permanent “multipoles” [20]. The interactions are also called orientation or Keesom interactions and are used to describe the energy of the dipole-dipole interaction [21] (Equation 1.3),

$$w(r) = -\frac{u_1^2 u_2^2}{3(4\pi\epsilon_0 \epsilon)^2 kTr^6} \quad \text{Equation 1.3}$$

Where  $u$  is the dipole moment and  $k$  is the Boltzman constant.

The second contribution to the total van der Waals force is polarization also known as induction and Debye interactions, which is the interaction between a permanent dipole and a neighbour neutral molecule which is polarized by the dipole. The energy of polarization can be calculated from Equation 1.4 with the dipole moment and polarizability  $\alpha_0$ ,

$$w(r) = -\frac{u^2 \alpha_0}{(4\pi\epsilon_0\epsilon)^2 r^6} \quad \text{Equation 1.4}$$

The dispersion London force is the third and most important contribution to the total van der Waals force. It is the universal attraction between two neutral molecules (or atoms). The interaction energy between two identical molecules (atoms) can be calculated by Equation 1.5,

$$w(r) = -\frac{3\alpha_0^2 h\nu}{4(4\pi\epsilon_0)^2 r^6} \quad \text{Equation 1.5}$$

Where  $h$  is the Planck constant and  $\nu$  is the orbiting frequency of the electron.

The Keesom and Debye interactions are only found among the molecules (atoms) which have permanent “multipoles” moments. While the dispersion interactions act on all the molecules. So in general the energy of van der Waals interactions can be expressed as Equation 1.6,

$$w_{VDW}(r) = -\left[ (u_1^2 \alpha_{02} + u_2^2 \alpha_{01}) + \frac{u_1^2 u_2^2}{3kT} + \frac{3\alpha_{01} \alpha_{02} h\nu_1 \nu_2}{2(\nu_1 + \nu_2)} \right] / (4\pi\epsilon_0)^2 r^6 \quad \text{Equation 1.6}$$

In most cases, the dispersion force is the dominant contribution and that is why van der Waals forces are referred to as dispersion forces. According to the fundamental origins of the three interactions, the interactions of Debye and dispersion are always attractive, while the Keesom interactions could be attractive or repulsive depending on the mutual orientation of the molecules [20]. So the total net van der Waals forces are always attractive because of the dominance of dispersion forces.

Hydrogen bonds are often regarded as those interactions associated with water molecules. The hydrogen bond is predominantly an electrostatic interaction between an H atom and electronegative atom and is much stronger than van der Waals interaction but weaker than a covalent or ionic bond [22]. Hydrogen bonds are very important in macromolecular and biological assemblies. In particular, they do not just occur intermolecularly but also intramolecularly even in non-polar environments [23]. The concept of hydrogen bond has been extended to all electron-acceptor and electron-donor interactions which are sometimes referred to as polar or acid-base interactions. Hydrogen bond interactions contribute the most to the polar components of surface free energy.

### **1.1.2 Surface Free Energy from Contact Angle Measurements**

When a drop of liquid is placed on a solid surface, the shape of the drop is

determined by the equilibrium of the triple interface between the solid, liquid and gas. The shape of liquid usually is described by the angle  $\theta$  between the solid surface and the tangent to the liquid surface at the line of contact [24] (Figure 1.1).

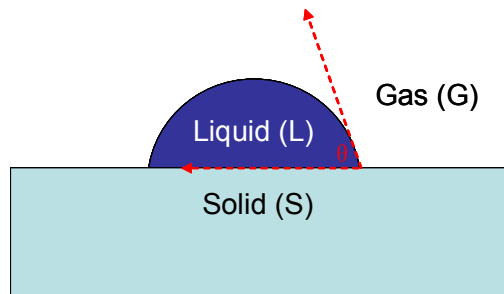


**Figure 1.1** Contact angle ( $\theta$ ) formation of liquid droplet in gas on solid surface.

This angle is also known as the contact angle. At equilibrium, all forces arising from the three interfacial energies ( $\gamma$ ) are in balance as described in the Young equation [25],

$$\gamma_{GS} = \gamma_{LS} + \gamma_{GL} \cos \theta_0 \quad \text{Equation 1.7}$$

$\gamma_{GS}$  is the interfacial energy between gas and solid phase, while  $\gamma_{LS}$  and  $\gamma_{GL}$  is the interface energies of liquid-solid and gas-liquid.

The process of wetting can be expressed by the value of the contact angle. If  $\theta < 90^\circ$ , the liquid is said to wet the solid; if  $\theta = 0$ , it is complete wetting; if  $\theta > 90^\circ$ , the liquid does not wet the solid. The contact angle is actually determined by the competing tendencies between the energy of cohesion of the liquid molecules and the energy of adhesion between the liquid and solid molecules.

If the work of cohesion between the liquid molecules is higher than the work of adhesion between the liquid and solid, the contact angle is formed based on their relative magnitude. If the work of adhesion is higher than the work of cohesion, wetting is preferred.

For a hydrophilic surface, the work of adhesion is stronger than cohesion and the contact angle of water is low; in contrast, for a hydrophobic surface, the contact angle is high. Water contact angle is a simple and quick method to obtain quantitative information on the chemical nature of surface [26] and can be used to determine the solid surface free energy based on work of adhesion with Dupré equation (1.8) and the work of Fowkes (1.9) [27],

$$W_A = \gamma_S + \gamma_L - \gamma_{SL} \quad \text{Equation 1.8}$$

The surface free energy consists of the sum of its components and intermolecular interactions occur between components of the same kind (Equation 1.9).

$$\gamma = \gamma^d + \gamma^p \quad \left( \gamma_i = \sum_j \gamma_i^j \right) \quad \text{Equation 1.9}$$

Where  $\gamma^d$  is the dispersion surface free energy component and  $\gamma^p$  is the polar surface free energy component.

Fowkes equation [28] was proposed to solve the solid surface free energy based on the contact angle measurements.

$$W_A = \gamma_L(1 + \cos \theta) = 2\sqrt{\gamma_S^d \gamma_L^d} + 2\sqrt{\gamma_S^p \gamma_L^p} \quad \text{Equation 1.10}$$

Many efforts had been made to solve the work of adhesion [29]. Among them Wu [30] method is suitable for polymers with relative low surface free energy.

$$W_A = \gamma_L(1 + \cos \theta) = \frac{4\gamma_S^d \gamma_L^d}{\gamma_S^d + \gamma_L^d} + \frac{4\gamma_S^p \gamma_L^p}{\gamma_S^p + \gamma_L^p} \quad \text{Equation 1.11}$$

One of the basic contact angle measurement methods is the static sessile drop method using a contact angle goniometer [29]. The angle which is formed by the liquid drop is recorded by a CCD camera and the contact angle is analyzed by software (Figure 1.2).

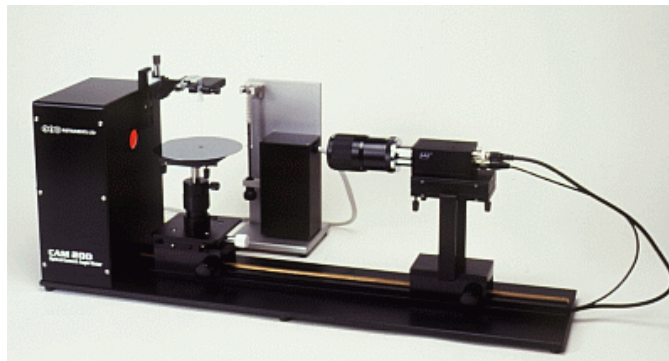


**Figure 1.2** Contact angle goniometer (KSV CAM 200) used in the LBSA (image from KSV website).

Various solid surfaces have been investigated with the contact angle method to derive the surface free energy values [31-33]. Although there are several methods that deal with complex sample surfaces like capillary rise [34] and thin layer wicking [35], most contact angle measurements still employ flat and smooth surfaces. In the Young equation, the microscopic surface heterogeneity

is not taken into account. The effects of surface roughness on contact angle have been noticed and some modifications have been made to surface free energy calculations from contact angle on the basis of roughness [36, 37]. The roughness also contributes to the hysteresis of contact angles in the dynamic sessile drop method [38]. Hysteresis, which is defined as the differences between the advancing and receding angle, is dominated by the chemical interactions or heterogeneities [39].

Neither the Fowkes nor Wu equation can derive the surface free energy with one liquid contact angle value. The contact angle values from several liquids are needed to access the solid surface free energy. In theory, the surface free energy results are not dependent on the liquids used. However in practice the choice of liquids can lead to a variation of several degrees in contact angle and variations of surface free energy values [40-41]. The combination of liquids including the non-polar liquid like diiodomethane and the polar liquids like water and formamide have been proposed with most solid surface contact angle measurements [42].

Before the introduction of inverse gas chromatography (IGC), solid surface free energy values could only be derived from contact angle measurements [43]. IGC can provide the solid dispersion surface free energy and with some mathematical modifications, it can also give the polar surface free energy [44].

Although the agreement has not been established on the correlation of dispersion surface free energy values derived from contact angle and IGC [45, 46], contact angles are still regarded as a simple, fast and relative accurate method to obtain the solid surface free energy.

### 1.1.3 Surface Free Energy from Solid Adhesion Measurements

Solid-solid adhesion without a medium is usually only dependent on the van der Waals forces between the two solid bodies. The van der Waals forces between two macroscopic solid surfaces are not the same as those described in equation 1.6. For interfacial interactions of van der Waals forces, the shape of contacted surfaces needs to be considered because the magnitude of interaction is the summation of all molecules involved. For van der Waals forces between a sphere and a flat surface, the interaction energies at a distance  $D$  are [20];

$$W(D) = -\frac{2\pi^2 \rho_1 \rho_2}{12} \int_{z=0}^{z=2R} \frac{(2R-z)z dz}{(D+z)^3} \quad \text{Equation 1.12}$$

Where  $\rho_1, \rho_2$  is density of molecules in the solid and  $D \ll R$ , only small values of  $z$  contribute to the integral;

$$W(D) = -\frac{\pi^2 C \rho_1 \rho_2 R}{6D} \quad \text{Equation 1.13}$$

The same method can derive the interaction energies with two flat surfaces [20];

$$W(D) = -\frac{\pi C \rho_1 \rho_2}{12D^2} \quad \text{Equation 1.14}$$

The interaction energies, however, are not easily measured between the solid surfaces. But the forces can be obtained with a Surface Forces Apparatus (SFA) or an Atomic Force Microscope (AFM) [47]. So regarding a sphere and a flat surface as two spheres (one sphere is very large), the two interaction energies and forces can be expressed as;

$$F(D)_{sphere} = 2\pi R W(D)_{planes} \quad \text{Equation 1.15}$$

According to equation 1.15, the interaction forces between two large spheres (Figure 1.3) with radius  $R_1$  and  $R_2$  at a distance  $Z=D+R_1+R_2$ ,

$$F(D) = \int_{Z=D}^{Z=\infty} 2\pi x dx f(Z) \approx \int_D^\infty 2\pi \left(\frac{R_1 R_2}{R_1 + R_2}\right) f(Z) dZ = 2\pi \left(\frac{R_1 R_2}{R_1 + R_2}\right) W(D)$$

Equation 1.16

Where  $f(Z)$  is the normal force per unit area between two flat surfaces,  $2\pi x dx$  is the area of a small circular region on one sphere surface.

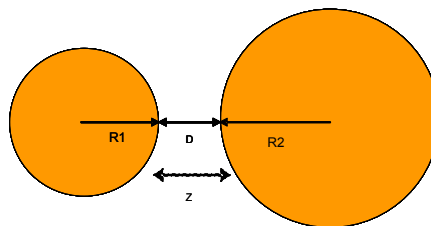


Figure 1.3 A Schematic representation of the two big rigid spheres located at a distance of  $D$ .

The equation 1.16 is called the Derjaguin approximation [48]. It is a useful theoretical tool which to easily derive the interaction energies for two solid

surfaces by their interaction forces.

The adhesion to a solid surface is critical in some industry processes like paints, coatings, adhesives [49] where strong solid-solid interactions benefit the performances of final products. In some cases adhesion should be strictly monitored especially in the case of Dry Powder Inhalers (DPIs). DPIs are propellant-free and multiple-dose alternatives to metered dose inhalers (MDIs) for drug delivery to the respiratory tract [50]. Drugs with particle sizes below 5  $\mu\text{m}$  are delivered by DPIs, formulated as either pure drug or mixed with an inactive excipient as a carrier [51]. The use of carriers can reduce the cohesion and static charges that interfere with pure drug formulations and improve the dose uniformity. However, the use of carriers also introduces competition between the adhesion between drug and carrier particles and drug cohesion and this can effect the penetration of the drug particles to the lung [50]. The interactions between drugs and carriers both in the DPI device with no moisture [52] and the respiratory tract environment with high relative humidity [53] have been modeled as solid particle-particle interactions with the factors such as surface property, size, drug/carrier ratio, relative humidity and electrostatic behaviour being studied [50].

The adhesion between solid surfaces will increase significantly with even trace amounts of vapour. Adhesion forces generally increase with the increasing

relative humidity [54]. The phenomenon is due to the water at the surface contact region causing so-called capillary condensation. Liquids which could wet the surface will spontaneously condense from vapour into the contact region as bulk liquid. The resultant capillary force can be quantitatively determined with the combined vapour and Laplace pressure in Equation 1.17 [55],

$$F = 4\pi R\gamma_L \cos \theta \quad \text{Equation 1.17}$$

The capillary force is one of the main contributors to solid-solid adhesions along with the van der Waals interactions. In some extreme situations (RH>60%), the capillary force is believed to be the dominant force [56]. In Ouyang's work, the capillary force has the same magnitude as the van der Waals interaction and for certain samples, the capillary force is much stronger (25 °C and 50% RH) [57]. So in particular applications such as DPI and manufacture processes, capillary forces should be avoided to improve the flowability and decrease adhesion by reducing the relative humidity [58].

However, in the measurements of solid adhesion forces, the experimental results usually have great biases towards the calculations from these equations due to the roughness and mechanical properties of materials [59].

## 1.2 Mechanical Properties of Pharmaceutical Materials

Generally speaking, the solid mechanical properties are properties such as strength, hardness, toughness, elasticity, plasticity, brittleness, ductility and malleability. Mechanical properties describe the behaviour of materials under an applied load. Solid behavior under a load is usually classified into three models based on the responds to the applied stress [60]:

① Elastic material – when the applied load is removed, the material returns to its undeformed state. The material deforms proportionately to the applied load on the elastic solid. The effect of load is reversible and the material completely returns to its original state. The stiffness of an elastic material can be characterized with Young's modulus which is defined as the ratio of the uniaxial stress over the uniaxial strain in the range of stress in which Hooke's Law holds.

② Viscoelastic material – a material behaves like an elastic material but also has the effects of strain resistance. That means after a load is applied, work has to be done against damping and a hysteresis loop is observed in the stress-strain curve. The dynamic modulus is used to describe the relationship between the oscillating stress and strain.

③ Plastic material –a material that behaves elastically when the applied load

is less than its yield value. Above the yield value, the material behaves plastically which means the material does not return to its previous state. The changes including material's structure are irreversible.

In pharmaceutical applications especially during tablets compression, elastic and plastic deformation will occur on the APIs and excipients. So the mechanical properties of tablets such as compactibility and compressibility are strongly dependent on the mechanical properties of the individual particles [61]. Based on the characterization of APIs, the excipients can be chosen that complement those mechanical properties like yield strength / pressure, brittleness, elasticity / viscoelasticity [61]. The equipments and conditions for processing need be carefully selected based on the mechanical properties of APIs and excipients [62]. Hence, there is a growth demand for the measurements of mechanical properties of powders at the pre-formulation stage in the pharmaceutical industry. In the pre-formulation stage, usually the quantities of API are limited. Hence, methods which can obtain the mechanical properties with small scale materials are extremely welcome. Especially, in the formulation of DPIs, the flow and dispersion properties have been related with mechanical properties of each single sub-micron particles [63]. So methods such as the nanoindentator and AFM indentation which can obtain mechanical properties on individual single particles have been employed at the pre-formulation stage and such applications as DPI where direct

particle-particle interactions are dominant.

### 1.2.1 Contact Theory Modified with Material Mechanical Properties

In the theoretical Derjaguin approximation, the two contact spheres were treated as totally rigid (Figure 1.3). But in the experimental adhesion measurements, the two contact surfaces will deform due to the externally applied loads and the attractive interfacial forces that pull the two surfaces together. The first attempt to calculate the contact region between two surfaces with elastic deformation considered is the Hertz theory [64]. In the Hertz theory, the adhesion forces between two surfaces were treated as zero and only the applied forces (F) were considered. For a system of a sphere and a flat surface (Figure 1.4), the relation with the applied forces and the contact radius ( $a$ ), the radius of sphere (R) and the reduced Young's modulus (K) is [65],

$$a^3 = \frac{RF}{K} \quad \text{Equation 1.18}$$

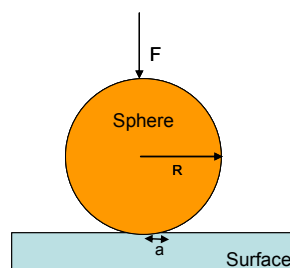


**Figure 1.4** The geometry of the contact between a sphere and a flat surface. F is the applied loading force.

The reduced Young's modulus can be determined by the Young's moduli of two

contacted surfaces [66],

$$\frac{1}{K} = \frac{4}{3} \left( \frac{1-\nu_t^2}{E_t} + \frac{1-\nu_s^2}{E_s} \right) \quad \text{Equation 1.19}$$

Where E is the Young's modulus and  $\nu$  is the Poisson's ratio.

Hertz theory has been applied to predict the contact region of two macroscopic surfaces. But the Hertz theory neglects any adhesions which commonly exist between any surfaces in contact. The good agreement of theoretical calculations and experimental results could only be achieved at the extreme case of large load and very small adhesion [68].

Many attempts have been made to add the adhesion forces into the Hertz theory [20], the most successful two among those approaches are JKR [69] theory and DMT [70] theory, which are widely applied.

The JKR (Johnson-Kendal-Roberts) theory treats all the adhesion forces only existing within the contact region. The adhesion force is considered as a change in work of adhesion (surface energy) between surface 1 and surface 2 ( $W_{12}$ ) only when the surface is in contact [65]. The contact radius  $a$  with JKR theory is:

$$a^3 = \frac{R}{K} \left[ F + 3\pi RW_{12} + \sqrt{6\pi RW_{12}F + (3\pi RW_{12})^2} \right] \quad \text{Equation 1.20}$$

If the load forces are zero, the adhesion forces or 'pull-off' forces are given by:

$$F_a = -\frac{3}{2}\pi RW_{12} \quad \text{Equation 1.21}$$

While the DMT (Derjaguin-Muller-Toporov) theory assumes the adhesion forces are not just within the contact area but also outside. The long-range attractive forces of basically van der Waals type are considered in the DMT theory [65]. The contact radius then is:

$$a^3 = \frac{R}{K}(F + 2\pi RW_{12}) \quad \text{Equation 1.22}$$

The adhesion (pull-off) forces at zero load forces are:

$$F_a = -2\pi RW_{12} \quad \text{Equation 1.23}$$

In practice, the DMT theory applies to the hard materials with low surface energies and a sphere with small radii [71]. In contrast, JKR theory works well for the soft materials with high surface free energy and the spheres with large radii [71]. There are still no perfect solutions to derive the exact contact region information like contact radius and deformation depth. The Hertz theory and its descendants JKR and DMT theories have been used as models to understand the contact, adhesion and friction [72]. The theories have established the methodologies to obtain the solid surface free energy with adhesions measurements and the solid Young's modulus with indentation measurements.

### 1.2.2 Young's Modulus Measurements with the Indentation Method

Young's modulus is defined as the ratio of load (stress) to deformation (strain). The methods to obtain the Young's modulus of a powder are various, such as the beam bending method, which was originally used to measure strength with a 2 point beam in bulk, and was used to calculate the Young's modulus with 4-point bending beam model and a knowledge of Poisson's ratio [73]. The methods to measure the Young's modulus also include indentation and diametrical compression [61]. The common equation to derive the Young's modulus was given by,

$$E = \frac{3F(1-\nu^2)}{4\sqrt{R}\delta^3} \quad \text{Equation 1.24}$$

Where  $\delta$  is the indentation.

However, the results from those methods provide bulk information and had large variations due to the potential phase transition and sample porosity [74]. For example, the Young's modulus value for the same material tested in bulk with indentation, compression and beam deflection has been reported as 18, 0.35 and 1.4 MPa, respectively [64]. So, for accurate Young's modulus determinations, rapid measurements and small amount of materials available at the early stage of development, new efforts are required to develop techniques to measure the material mechanical properties at the submicron scale [75].

Nanoindentation methods usually employ a sphere probe with radius of tens of microns and a system recording the indentation of probe during the load applied [61, 76]. However in this approach, the radius of probe is still relatively large and the applied forces are usually high. The outcome is that the measurement usually leads to a permanent damage of the surface and crystal fracture [76]. With the rapid development of AFM, the use of AFM as a nanoindentation method to assess the material Young's modulus at a nanometer scale has been well accepted [77]. Some pharmaceutical materials such as lactose, sucrose, sodium stearate, acetaminophen and sulfathiazole have been measured with AFM nanoindentation methods to derive the Young's modulus values [78-81]. In AFM nanoindentation, the silicon nitride or silicon oxide AFM probe is used as the indentator hence loads and indentations are truly on the nanoscale. The shape of the AFM probe is usually easy to obtain from either SEM imaging or AFM reverse imaging methods [82]. The indentation ( $\delta$ ) can be determined by the gradients of the contact region between a hard non-deformable surface and the sample surface [83]. The unique advantage of AFM nanoindentation is the ability to combine high-resolution imaging, composition mapping with spatial resolution in nanometers and local mechanical studies with forces at nanoNewtons [84].

## **1.3 The Applications of AFM Imaging and Force Measurements in Pharmaceutical Applications**

Since the invention of AFM, it has been a useful tool for direct measurements of intermolecular forces with atomic-resolution characterization in a broad spectrum of applications such as electronics, semi-conductors, materials and manufacturing, polymers, biology and biomaterials [85-87]. The ability of imaging and in situ force measurement of AFM in pharmaceutical applications can generally be classified into two aspects: the imaging which focuses on the structure determination and the force measurement which focuses on the mechanical properties and interface energies [88]. However, it should be remembered that the principal of AFM imaging still depends on the interaction forces between probe and surfaces regardless of whether the contact or tapping mode is operated.

### **1.3.1 The AFM System**

The basic components and features of AFM mainly include (Figure 1.5): (1) A fine probe which scans near/on the surface and detects some physical quantity. The fine probe is generally monolithic structure formed by a photolithographic process out of Si, SiO<sub>2</sub>, or Si<sub>3</sub>N<sub>4</sub> [89]. The probe is attached to a flexible cantilever. The surface forces experienced by the probe bend the cantilever which is detected by an optical system consisting of a diode laser and a

position sensitive detector [90]. (2) A piezoelectric (PZT) translation system with a suitable feedback system controls the tip/surface separation and translation in the sample plane. The PZT scanner expands and contracts proportionally to an applied voltage and can keep the probe at a constant force, or a constant height above the sample surface. (3) A feed back system holds the tip near the surface at a preset value of force, or height by controlling the vertical separation distance between tip and sample surface.

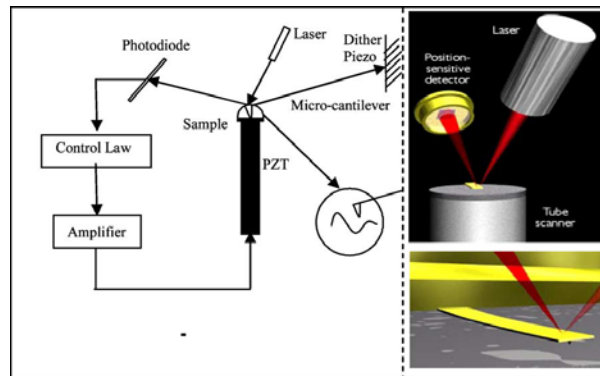


**Figure 1.5** Schematic of basic AFM operation and real micro-cantilever and components [88].

So the principle of AFM operation is to scan the probe over the sample surface with the feed back mechanisms that enables a PZT scanner to maintain the tip at a constant force, or constant height above the sample surface [88,91].

### 1.3.2 The Applications of AFM Imaging to Pharmaceutical and Biopharmaceutical Research

AFM is designed to obtain surface 3D morphology on non-conductive samples

with a resolution of 0.1 nm in height and a lateral resolution better than 1 nm [92]. An advantage of AFM over other high resolution techniques is the ability of operation in both air and liquids [93]. Non-conductive sample imaging and liquids operation have made the AFM an extremely powerful tool in bio and pharmaceutical sciences. For example, the morphology and movement of living cells has been measured with AFM on a time scale of minutes in a liquid medium [94]. The easy alteration of environment parameters with AFM imaging system has provide researchers great opportunities in study how living cells respond to temperature and potential drugs [95, 96].

Another application of AFM imaging is the static and dynamic characterization of nucleic acids - proteins assemblies [97]. To image nucleic acids a specially prepared surface that holds the samples by electrostatic interactions is created by using aminosilanes on a mica surface [98]. The bindings of proteins on DNA involve intracellular regulation of gene metabolism, not only in function but also in spatial conformation. The search for target sites among the vast amount of non-specific sites and the large conformational changes in both proteins and DNAs after the protein binding or exchange between the specific sites and non-specific sites have been studied in vitro by AFM imaging method (Figure 1.6) [99, 100].

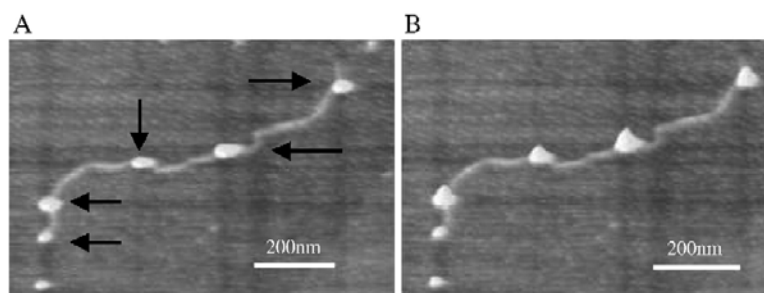


**Figure 1.6** Visualization of the interaction between linear DNA and PprA protein by AFM [100]. The arrows represent the end and internal bound PprA proteins.

The resolution of AFM imaging on the nucleic acids has been further improved by the introductions of AFM carbon nanotube tips (Figure 1.7) [101].

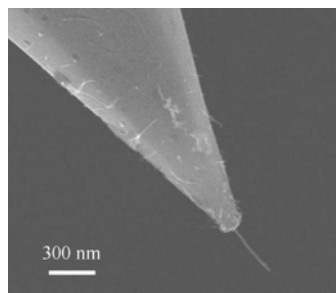
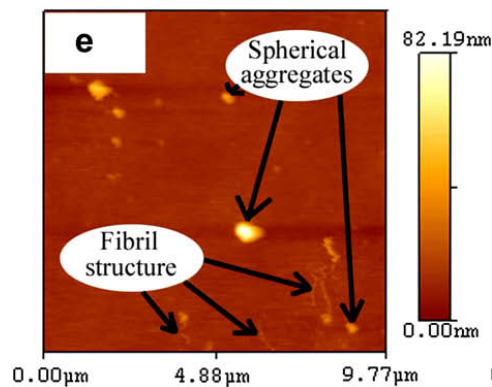


Figure 1.7 A SEM image of a carbon nanotube tip attached to a standard AFM tip.

The nanotube tip method belongs to one of the large applications of AFM where the probe is modified. For example, a so called colloid AFM probe can be prepared by gluing a single particle (or crystal, nanotube) to the end of an AFM cantilever or coating one polymer (or chemical film) to an AFM probe and used to measure the interactions between the colloid probe and sample surface [102]. The attachments of single DNA (or RNA) strands have driven the application of single molecule atomic force spectroscopy to investigate the interactions and elasticity at single-molecule level [103].

The quality of AFM images strongly depends on the probe profile: an incorrect choice of the probe for the required resolution can lead to the image artifacts. So many efforts have been made to correlate the AFM topography images with other microscope methods such as optical and confocal microscopy [104, 105].

The high-resolution 3D imaging and no sample treatments required with AFM have also provided great conveniences for pharmaceutical applications, e.g. for direct observation of the nanostructure of polymers surfaces [106] and the structure related physical properties of gelatin gels at difference concentrations (Figure 1.8) [107]. The AFM phase images obtained during tapping mode imaging have been used in stability testing against phase separation within a formulation: the stability of Amphotericin B with lipidic components has been determined on the nanoscale level with AFM (Figure 1.9) [108].



**Figure 1.8** An AFM image of spherical aggregates and fibril structure in 0.25% concentration gelatin [107].

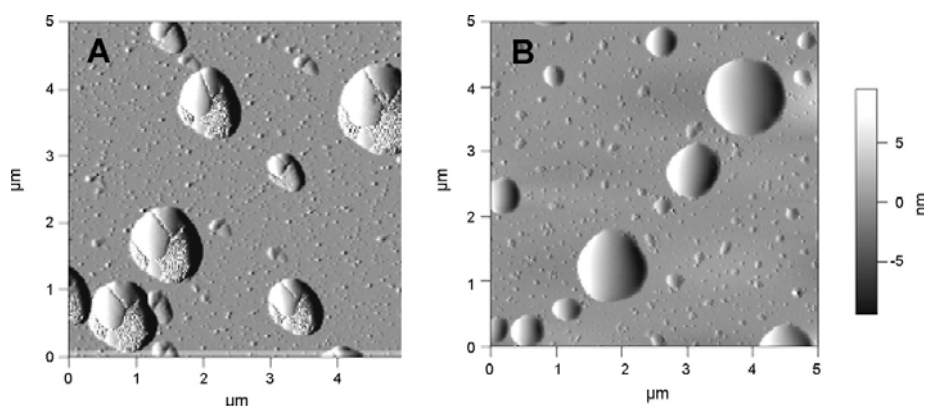


**Figure 1.9** AFM images of AmpB prepared in (A) Peceol alone (B) Peceol/DSPE-PEG2000. Droplets applied to the substrate exhibit phase separation of components in (A) but not in (B) [108].

The structures and growth mechanism of crystal surfaces have also been widely studied with AFM imaging methods. In pharmaceutical applications the crystallization of an API is critical for the success of final products and it is known that the polymorphs of drug crystals that can have different biopharmaceutical, thermal and physical properties are also important. Crystal morphologies and polymorphism are determined by the crystal packing at the molecular level [109]. Successful studies have been done with the API and excipient crystals, e.g. on particular crystal face of paracetamol (0 0 1) [110] and  $\alpha$ -lactose monohydrate (0 1 0) [111].

### **1.3.2 The Applications of AFM Local Force Measurements**

The mechanical properties obtained from AFM local force measurements have been discussed in 1.2.2. Here, the adhesion forces derived from AFM local force measurements will be reviewed. In AFM local force measurements, the results are so-called force-distance curves (Figure1.10). It is easy to identify the adhesion forces on the withdraw part of the force-distance curve. The

adhesion force between tip and sample surface will keep the tip contact with the surface until the cantilever force overcomes it. In the force-distance curve in Figure 1.10, the adhesion (or pull-off) force is at position 5 in the jump-off region.

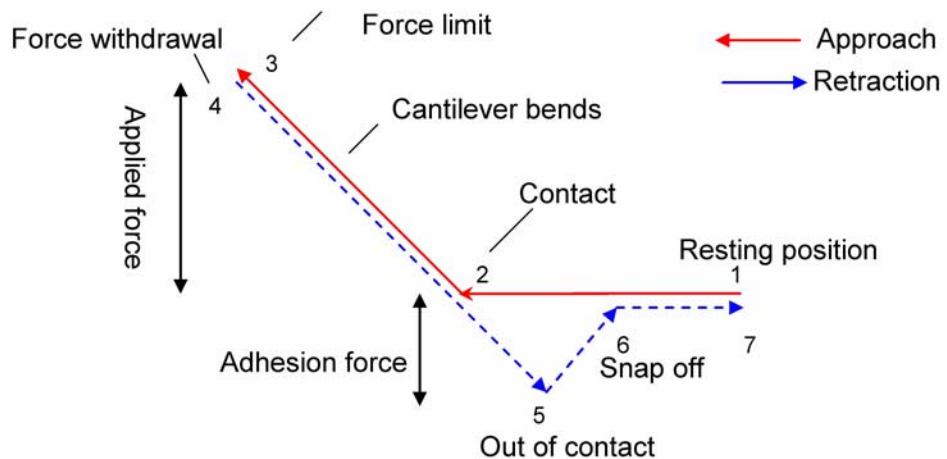


**Figure 1.10** A representative force distance curve. From positions 1 to 2, the tip is approaching the surface, and at position 2 contact is made. From positions 2 to 3, the cantilever bends until it reaches the specified force limit that is to be applied; it is then withdrawn during positions 4 and 5. At position 5, the tip loses contact with the surface but the adhesion force between tip and surface still bends the cantilever until at position 6 where the adhesion force becomes “zero”. From positions 6 to 7, the cantilever returns to its resting position and ready for another measurement.

The adhesion force is a combination of van der Waals forces, polar interactions, electrostatic interactions and capillary forces. The results of direct adhesion force measurements on the same material usually have significant variations due changes in surface roughness leading to changes in contact area or changes

in surface chemistry (e.g. on different crystal faces). It is now generally agreed that the adhesion forces decrease with the increased roughness and increase with the increased relative humidity [112]. It is easy to understand that the adhesion forces will increase due to the increased capillary force with higher relative humidity (Equation 1.17). The roughness of both probe and sample surface is not taken into account neither in the Hertz theory nor JKR-DMT models. But there are many asperities on the real solid surfaces and the larger the roughness, the more chances the asperities forms the contact instead of the whole surface (Figure 1.11). The actual contact radius is then the radius of those small asperities which then would reduce the van der Waals forces [113].

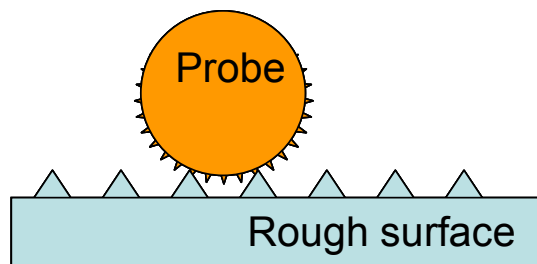


**Figure 1.11** A schematic image of asperities effect of contact geometry on rough probe and surface.

One breakthrough in adhesion force measurements was the introduction of colloid probe technique [114]. In colloid probes, the chemical and physical properties can be well defined and also modified to achieve specific interactions. The particles or single crystals attached to the AFM cantilever usually have regular shapes which make the actual contact area closer to the description in theory. The advantage of the colloid probe technique is the

ability to chemically modify the surface that allows an investigation on particle-particle (surface) specific interactions and how much interactions are influenced by different conditions. For example, the chemical binding forces between living cells and colloid probes which are modified with different silane coupling agents [115] had been studied [116].

It is still hard to determine the contact area in the colloid probe technique. The small crystalline particles used in the pharmaceutical industry often have complex surface morphologies and asperities on their sample surfaces which are much smaller than the radii of say glass bead colloid probes (Figure 1.12).

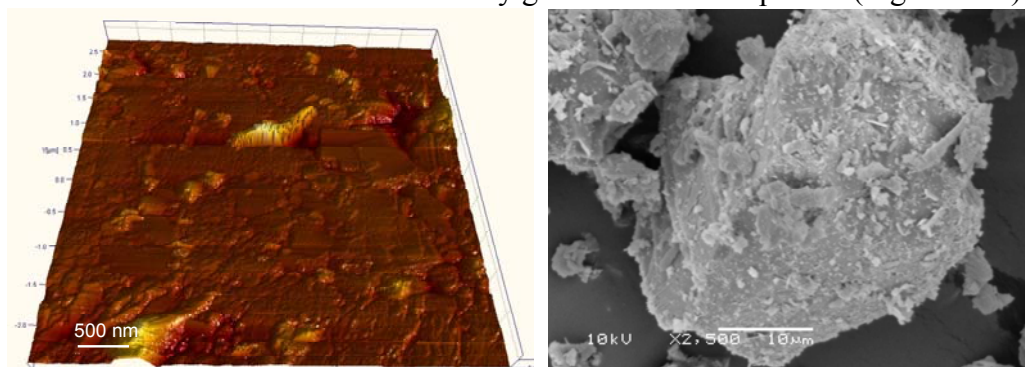


**Figure 1.12** An AFM image of dibasic calcium phosphate dihydrate, scan size 5  $\mu\text{m}$  (Left). And a SEM image of dibasic calcium phosphate dihydrate (Right).

So in this case the contact area is not as the same as the colloid probe but reflects the asperities on the particle surface. The use of a crystalline particle as the colloid probe may be regarded as a solution for pharmaceutical systems since the surfaces of probe and sample surface may be similar in such experiments. But for crystalline particle colloid probes, it is important that high

loading forces are avoided to prevent the changes of probe geometry due to the fragility of crystal structure [117]. So the profiles of these colloid probes need be examined carefully after each measurement. These simple adhesion force measurements are generally semi-quantitative methods, and the results derived from those measurements are not easily comparable as they change from tip to tip. The higher adhesion force derived from the same probe does not indicate that the surface is more adhesive because the contact area depends on the deformation of sample surface also contributes to the adhesion forces. So the mechanical properties of sample surface need be considered also in AFM force measurements.

From the Hertz and JKR theories, the relationship of adhesion force at zero load force and work of adhesion with defined contact radius are clearly revealed in Equation 1.21. The relationship between work of adhesion and surface energies of two contacted surface is given as Equation 1.25 which is a modified Dupré equation used in solid surfaces [118]:

$$W_{12} = \gamma_1 + \gamma_2 - \gamma_{12} \quad \text{Equation 1.25}$$

Clearly, the work of adhesion has lead to the derivation of surface free energy based on equation 1.25. But it is not easy to calculate the interfacial energy ( $\gamma_{12}$ ) in practice. However, there is a good approximation to solve the work of adhesion with dispersion surface free energy in the situation where only

dispersion forces interactions exist:

$$W_{12} \approx \sqrt{W_{11}^d W_{22}^d} \approx 2\sqrt{\gamma_1^d \gamma_2^d} \quad \text{Equation 1.26 [20]}$$

This approximation has also given another equation for interfacial energy derived from equation 1.25 & 1.26:

$$\gamma_{12} \approx \gamma_1 + \gamma_2 - 2\sqrt{\gamma_1^d \gamma_2^d} \quad \text{Equation 1.27}$$

Using this equation, the theoretical calculation of interfacial energy between water and octane has been done. The calculated result was very close to the experimental value [20]. This agreement indicates that when the interactions are mainly contributed by dispersion forces, the approximation in equation 1.26 can derive a relative reliable dispersion surface free energy value from the work of adhesion between the two contact surfaces (if one of the dispersion surface free energy value is already known).

The complex origins of adhesion forces make the work of adhesion hard to relate only to the dispersion interactions. The main contributions to the adhesion forces are van der Waals force, capillary force, electrostatic force and electrical force (electric double layer) [119]. The capillary force strongly depends on the relative humidity of the air in the case of solid-solid interaction [56] and the electrical force (electric double layer) can only occur through a liquid medium [120]. In theory if the moisture is not present in the gap of two

surfaces, the capillary and electrical forces are not significant to the total adhesion force [121]. The electrostatic force between two contacting solid surfaces with a load is believed to be around 50 times smaller than the van der Waals force [122]. In conclusion, in the case of very low relative humidity between two contacting solid surfaces, the adhesion force is mainly contributed to by the van der Waals force only [123].

In AFM adhesion force measurements, the adhesion forces were collected at low humidity to derive the dispersion solid surface free energies. The approach started from the measurement of adhesion forces between the same material surfaces by AFM colloid probe technique [124]. A polymer sphere was used as the colloid probe to measure the adhesion forces on a flat surface of mica, the surface energy of that polymer was determined from the adhesion forces [125, 126]. In contrast, a glass bead has been used as the colloidal probe to measure the adhesion forces and calculate the surface energies of different sample surfaces [127]. As mentioned in 1.3.1, the colloid probe method to derive surface energies can encounter problems such as low lateral resolution and the changes of probe morphology during measurements. So alternatively, the normal AFM probe has been used to obtain the adhesion forces and surface energies on the sample surface [128].

The use of normal AFM probe has provided more conveniences to researchers

for solid surface energy determination: the shape of AFM probe can be determined by the reverse imaging method [82] and the morphology of AFM probe does not easily alter during measurements. The materials of AFM probes are usually silicon and oxidized silicon, so the chances of polar interactions between the probes and most sample surfaces in dry air is minimized. The resolution of adhesion force measurement with a normal AFM probe is highly improved to the nanometer scale which makes the surface energy (dispersion surface free energy) measurements possible on single crystal faces [129]. The crystalline lactose monohydrate and amorphous form of lactose are well distinguished by the surface energies derived from adhesion forces. With such resolution, the differences of the polymorph sites on a single crystal surface in mechanical properties and surface energies can be determined by AFM probe adhesion force measurements.

The solid surface free energy associated with the adhesion between two solids surfaces is fundamental to the understanding of the pharmaceutical applications such as mixing, blending, components selection and API release from carrier and matrix [130]. However, there are not many options to measure solid surface free energy: the contact angle method which is described in 1.1.2 actually derives the surface free energy from the interactions between liquids and solids. For some materials with higher surface free energies which are easily completely wetted by the liquid probes, the contact angle can not be used

to obtain their surface free energies. The surface free energy derived from IGC is based on the interactions between vapours and solids. The results derived from IGC method may be overly influenced by the high-energy site due to the infinite dilution of vapor probes [129]. In contrast, AFM force measurements directly investigate the solid-solid interactions and derive the solid surface free energies from the solid-solid interactions. So the AFM adhesion forces measurements can be regarded as a powerful tool complementary to current contact angle and IGC methods.

## **1.4 Solid State Surface Characterizations in Pharmaceutical Applications**

The surface for pharmaceutical applications is extremely important as it presents the interface for any physical and chemical interactions. So the characterization of solid surface is valuable in product design, optimizing performance and function [15]. In pharmaceutical applications, various solid materials including crystalline drugs, polymers, and metals are used as APIs, excipients and packing/device materials. The surfaces of these materials all need be characterized in both physical and chemical ways. In the previous sections, the methods such as contact angle, Young's modulus measurements, AFM imaging and adhesion force measurements were discussed. In this section, the characterization of the chemical properties of such materials surface will be

explored.

#### 1.4.1 Attenuated Total Reflection Infrared (ATR-IR) and Near Infrared (NIR) Spectroscopy

ATR-IR and NIR belong to the vibrational spectroscopy techniques which use the particular spectral range from the electromagnetic spectrum at which the chemical bonds in molecules vibrating [131]. In IR the wavenumbers are from 4000 - 400  $\text{cm}^{-1}$ , while in NIR the wavenumbers are from 13000 - 4000  $\text{cm}^{-1}$  [132]. In IR and NIR spectroscopy the sample absorbance is recorded at each wavelength. In the IR spectrum, the absorbances of energy at the vibrational and rotational frequencies of atoms are recorded, while for the NIR spectrum the molecular overtone and combination vibrations are recorded [133].

ATR-IR has been developed to avoid the sample dilution required in normal IR analysis. So ATR-IR is more practical for solid surface analysis. The ATR refers to the phenomenon that when a beam of light passes from a high refractive index medium to a low refractive index medium, that if the angle is greater than the critical angle, all the reflection are internal only (Figure 1.13).

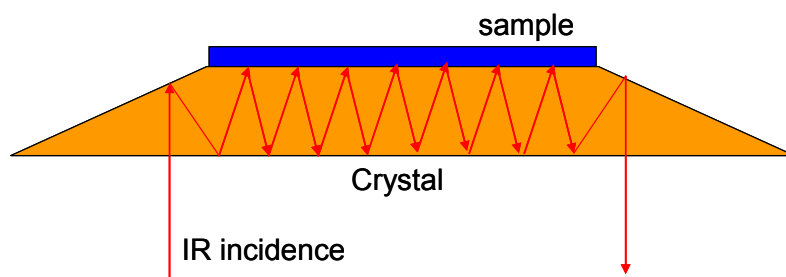


**Figure 1.13** A schematic image of attenuated total reflection of infrared radiation through the transmitting crystal.

In ATR-IR, the high refractive index medium is created by a crystal made of ZnSe, Si, Diamond or Ge. ATR-IR is a (near) surface characterization method because the light is totally reflected at the crystal-sample surface interface although the energy could penetrate into the sample surface a short distance (several microns) [133]. For those materials in solid forms with high Young's moduli, usually diamond crystals are preferred because such materials need high pressure to keep in contact with the ATR-IR crystal. The organic matter fouling of nano and ultra-filtration membranes had been characterized by ATR-IR spectral comparisons before and after use [134]. With little sample preparations and reliable spectra, ATR-IR is now widely used to identify materials and to find counterfeit and polymorphic forms especially on the tablet surfaces during stability testing [135].

NIR can also obtain the sample spectra as fast and as nondestructively as ATR-IR but is based on the combination and overtone vibrations in the near-infrared range. The NIR spectra are narrow and the peaks in NIR spectra are broad and overlapping [136]. The identification with NIR spectra is difficult. So the statistical analysis of the spectra is often required for molecular identification and quantification [137]. The raw materials used in pharmaceutical applications such as Avicel have been identified by NIR spectra

to find the differences in Avicel PH-101, 102 and 200 [138]. NIR has been applied widely for material identification and qualification including distinguishing polymorphism of crystalline drugs [132].

One prime advantage of the NIR spectroscopy is the ability to obtain the chemical mapping of a two-dimensional area of a sample (Figure 1.14). The chemical mapping technique relies on the interface of an optical microscope, equipped with a motorized stage to the NIR spectrometer [139]. The interested area of interest is first selected by the optical microscope. Subsequently, the same visual area is defined for the NIR spectroscopic analysis.

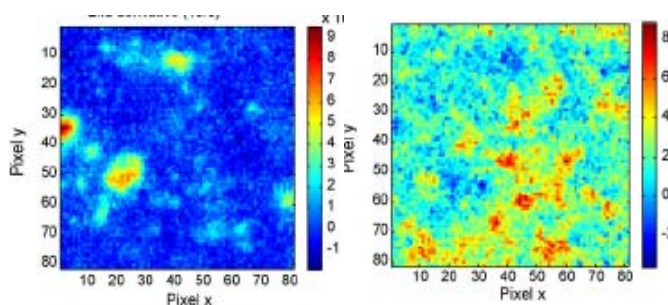


**Figure 1.14** NIR chemical mapping of one API (left) and cellulose (right) on one model tablet showed the position of high density domains of substrates [139].

The individual spectra are acquired for each spatial location with a lateral spatial resolution of 5-10  $\mu\text{m}$  within the two dimensional area. Once the individual spectra are collected, the intensity of a specific spectral feature within each spectrum can be plotted versus the spatial position [140]. The spectra are then processed by the baseline correction and the normalization to

remove the spectral and spatial artifacts like the detector noise and surfaces roughness [141]. The chemical distribution map is extracted by comparing the spectra at every pixel with the spectra of pure materials with the image process methods which use mainly univariate and multivariate analysis [135]. In this manner, the position of a certain material in the mixtures can be located. With this method, the distributions of an API or each excipients have been revealed in powder blending, granulation and solid dosage formulations [132]. In contrast to ATR-IR measurements where the reflections are within the top 3  $\mu\text{m}$  of the interface, near-infrared can penetrate much further into the sample. The actual penetration depth in NIR is difficult to determine because it also depends on the properties of sample matrix. A study has shown that the penetration depth of NIR can be as deep as 750  $\mu\text{m}$  [142]. So NIR can not be regarded as a surface method but as a bulk technique instead.

#### **1.4.2 Time-of-Flight Secondary Ion Mass Spectrometry (ToF-SIMS)**

In ToF-SIMS, the secondary ions are generated by the direct collisions of high energy primary ions like  $\text{Cs}^+$  and  $\text{Bi}^+$  with the sample surface. The energy with primary ions is considerable higher than the bond energy of most molecular species within a lattice so the collisions result in bond breaking. The atomic particles are first emitted and as the energy cascade becomes less, fewer bonds can be broken and so the large molecular fragments are emitted. The collisions

provide enough energy for elements, molecules and particles in the top of 2-3 monolayers to overcome the surface binding energy and leave the sample [92]. ToF-SIMS is regarded as a highly sensitive qualitative surface characterization technique. The sputtered secondary particles are ejected as neutral atoms, molecules, electrons and ions and they travel through the time-of-flight (ToF) analyzer. The mass to charge ratio of the fragment determines the time that it takes to travel through the analyzer. A fixed voltage accelerates the secondary ions into the ToF analyzer, with its polarity determining whether positive or negative secondary ions are analyzed (Figure 1.15). So the positive and negative secondary ion mass spectra consist of the ion mass charge ratio versus the number of ions detected. The mass spectra generated from ToF-SIMS can be used to identify the chemical structure and composition. The structures of polymers have been characterized with the ToF-SIMS fragment ion characterization: the backbone, side-chain and high-repeat units of polymer were determined with the peaks pattern in the spectra [143].

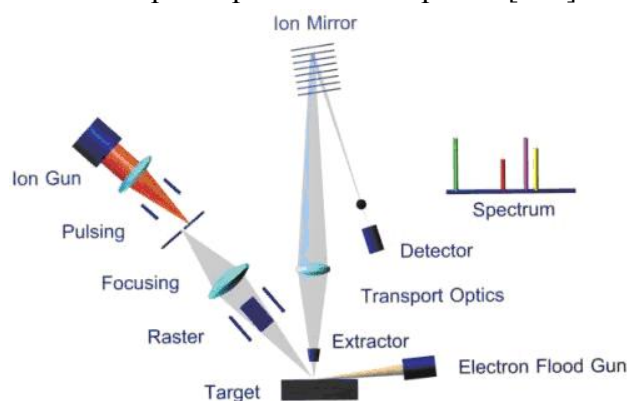


**Figure 1.15** A schematic diagram of the ToF-SIMS instrument (D.W. Mogk Montana State University).

Chemical mapping of a surface can also be obtained by the ToF-SIMS. The mapping area is first identified by an optical microscope. Then, the primary beam is focused to the area and the beam raster across the area surface. A complete mass spectrum is obtained at each point in the raster of the ion beam. After data acquisition, a specific ion or a combination of ions of interested material can be selected and compared with spectra at each pixel to generate the surface distribution map (Figure 1.16).

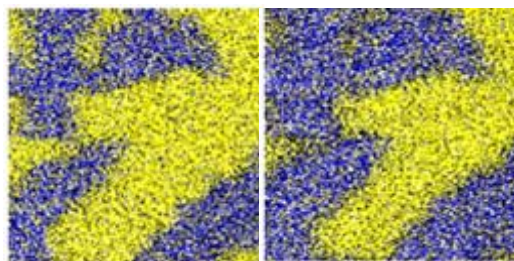


**Figure 1.16** Distribution maps of rapamycin (yellow) and PLGA (blue) in eluting coatings at the depth of 22 nm (left) and 33 nm (right) [144].

The resolution of chemical mapping depends on the focus size of the primary ions. For a ToF-SIMS equipped with a  $\text{Bi}^+$  ion gun, the lateral resolution can be better than 100 nm [145]. With the ToF-SIMS imaging analysis, the distribution of a drug has been assessed in a complex biological sample to understand the surface composition and structure and learn the events happened on the surface [146]. The effect and pharmacokinetics of drugs on proteome and lipidome can be assessed by ToF-SIMS analysis [147]. The ToF-SIMS imaging analysis has also been employed from traditional inorganic samples to more biopharmaceutical systems such as cells, tissues,

macromolecules and nucleic acids [148]. The change of distribution of vitamins A and E in tissues under different conditions has been reported by employing the ToF-SIMS imaging analysis [149]. There is no requirement for fluorescent labels with ToF-SIMS imaging analysis, providing more convenience for bio/pharmaceutical research [150]. However, the samples for ToF-SIMS need more preparation than ATR-IR and NIR. Any contamination on the sample surface will be detected in the ToF-SIMS analysis and hence can disturb or mask the underlying spectrum [151]. For biological samples, special treatments such as cryofixing and chemical fixation may be also necessary [152]. Other factors like the thickness of a sample, surface roughness and surface charging during measurements can also influence the yield of secondary ions.

## **1.5 Thermal Properties and Thermal Measurements on Solid Pharmaceutical Materials**

Thermal phenomena accompany all the physical and chemical reactions and changes because all those processes result in a change in heat content (enthalpy) [153]. Besides the thermal conductivity and coefficient of thermal expansion, the temperatures at which the thermal phenomena occur such as the endothermic processes (melting, boiling, sublimation, vaporization, desolvation, solid-solid phase transition and chemical degradation) and the exothermic

processes (crystallization and oxidative decomposition) are monitored because the temperature is sometimes the only effective indicator for such reactions [154]. For pharmaceutical solid materials, perhaps the most important temperatures are the melting point temperature and phase transition temperature. The melting point temperature at which the solid changes state to liquid is usually unique for the solid crystalline material. The melting of solid crystalline material is associated with the disruption of a crystal structure, which is determined by the chemical bonds and molecule arrangements in lattices [155]. So for one certain crystalline material, the melting point temperature should be consistent. If there are impurities, amorphousness and/or polymorphic crystalline materials coexisting with the structure, the temperature of melting point will alter and the range of temperature will broaden [156]. In practice, the characterization of melting point temperature is used as a method for material identification, purity testing, and distinguishing polymorphs [157]. In contrast, there are some solid materials like glass (amorphous materials) which do not have the abrupt phase change at one specific temperature but a gradual change over a range of temperatures where the viscoelastic properties will change from a glassy to a rubbery status [158]. The temperature which represents this transition is called the glass transition temperature ( $T_g$ ) and the transition is classified as the second order transition while melting is the first order transition [159]. The glass transition temperature is not as consistent as the melting point for crystalline material. For polymers, it is found that the

more immobile the chain, the higher the glass transition temperature will be [160]. The phase transition temperature is generally a name for the other phase phenomena during heating such as crystallization, crystal dehydration (rehydration), solid-solid transition and desolvation. The characterization of those temperatures can help investigate the pharmaceutical applications like stability, polymorphism, drug-excipient compatibility and the determination of kinetic parameters [156].

The most popular technique used for solid material thermal properties determination in pharmaceutical applications is the Differential Scanning Calorimetry (DSC). In the DSC analysis, the differences in power required to maintain the sample and the reference to the same temperature are recorded as a function of temperature [159]. In DSC analysis, the transitions (first and second order) can be observed in the curve of heat flow versus temperature. The samples for DSC analysis usually do not need special preparations but need be weighed. Before the heating starts, the sample and reference need be pre-heated to achieve the same temperature in the pans. DSC is a rapid and accurate method to determine the thermal properties from bulk solid materials.

The surface thermal properties of a material can be assessed by using the Scanning Thermal Microscope (SThM) which is a development from the AFM technique. The temperature of melting or glass transition can be determined by

SThM local thermal analysis (LTA) mode. In LTA, the thermal probe (Figure 1.17) of SThM is heated at a specific rate and approaches to a surface. SThM has been used to study the NiTi Shape memory alloy thin films deposited on the silicon wafer to investigate the martensitic to austenitic transformations [161].

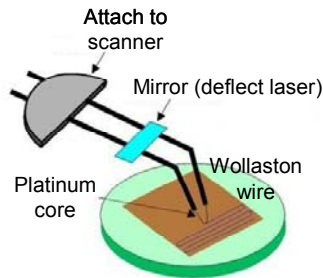


**Figure 1.17** A schematic diagram of SThM thermal probe.

Another operation mode in SThM is the imaging according to topography and thermal conductivity [162]. In this mode, the thermal probe is rastered over the area at a constant temperature, the power required to maintain the pre-set temperature is recorded. As the heat flow between probe and sample surface varies due to thermal properties differences across the surface, the conductivity map as well as the topography image can be obtained. However, in this mode, the thermal probe scans over the area in the contact imaging mode, and therefore, a very complex surface will decrease the resolution of the topographic image and also make the heat flow between the probe and surface difficult to model. So the thermal conductivity mapping method can identify the different materials only for very flat surfaces [163, 164]. However, in the LTA measurements of SThM, the applications are various because of the ability

to measure the surface thermal properties with micron spatial measurement resolution. The surfaces of polylactic acid microspheres which used as delivery vehicles have been characterized by the SThM LTA measurements and the presence or absence of a drug on the exterior of the spheres can also be studied by the LTA analysis [165]. And the two polymorphic forms of cimetidine have been distinguished by the SThM LTA measurements in the 50:50 mixtures [166]. Especially for the micro-electro-mechanical-systems, SThM has provided the chances to thermal characterize the micro devices [167].

A recent development of SThM is the nano-TA system. The nano-TA has the same function as the original SThM but with much higher spatial resolution. Instead of the Wollaston wire used in the original SThM, nano-TA uses the specific thermal probe which is as sharp as an AFM tapping probe (Figure 1.18). So the spatial resolution of local thermal analysis can be improved to sub 100 nm [168]. The sharp probe used in the nano-TA system also benefits the thermal conductivity imaging function of SThM. The resolutions of topography and phase images are comparable with those obtained by normal AFM tapping probes. With the enhanced controller, a higher heating rate and broader temperature range can be achieved with the nano-TA system [169].

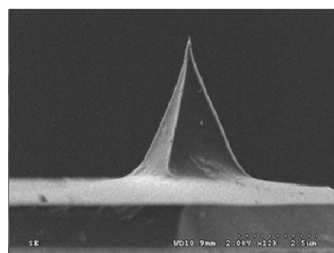


**Figure 1.18** A SEM image of thermal probe used in the Nano-TA system.

## **1.6 Aims of the Thesis**

In this thesis, a new methodology which can visualize and identify materials on the surface with sub-micron resolution was established. The high resolution topography images of surfaces were obtained by AFM imaging method and the materials were identified based on their surface free energies and melting point temperatures. The surface free energy was derived from the adhesion force between a AFM probe and the sample surface at low relative humidity. And melting temperature was obtained by the local thermal analysis of Nano-TA system with a sharp thermal probe. By combining these two parameters with surface topography images, the position of single particle of material had been located on the model binary mixtures surface.

With such a method, the changes (phase transition, degradation and polymorphism) happened at small scale (single particles) due to processing and stability testing on solid surface can be detected.

### **Publication:**

J. Zhang, S. Ebbens, X. Chen, Z. Jin, S. Luk, C. Madden, N. Patel and C. J. Roberts. Determination of the surface free energy of crystalline and amorphous

lactose by atomic force microscopy adhesion measurement. *Pharm. Res.* **23** (2006) 401.

## References

1. J. O. H. Sham, Y. Zhang, W. H. Finlay, W. H. Roa and R. Löbenberg. Formulation and characterization of spray-dried powders containing nanoparticles for aerosol delivery to the lung. *Int. J. Pharm.* **269** (2004) 457.
2. R. Vanbever, J. D. Mintzes, J. Wang, J. Nice, D. Chen, R. Batycky, R. Langer and D. A. Edwards. Formulation and physical characterization of large porous particles for inhalation. *Pharm. Res.* **16** (1999) 1735.
3. P. W. S. Heng and O. M. Y. Koo. A study of the effects of the physical characteristics of microcrystalline cellulose on performance in extrusion spheronization. *Pharm. Res.* **18** (2001) 480.
4. H. G. Brittain. Physical characterization of pharmaceutical solids. Marcel Dekker, New York, 1995.
5. Q. Zhou and M. Xanthos. Nanosize and microsize clay effects on the kinetics of the thermal degradation of polylactides. *Polym. Degrad. Stab.* **94** (2009) 327.
6. J. G. Ibanez, A. A. Ordaz, S. G. Granados and N. Batina. Nanoscale degradation of polypyrrole films under oxidative stress: an atomic force microscopy study and review. *Polym. Degrad. Stab.* **93** (2008) 827.
7. P. A. Clark, A. M. Clark, A. Rodriguez, M. A. Hussain, J. J. Mao. Nanoscale

characterization of bone-implant interface and biomechanical modulation of bone ingrowth. *Mater. Sci. Eng., C* **27** (2007) 382.

8. Y. Yoshioka, K. Asao, K. Yamamoto and H. Tachi. Preparation and characterization of nanoscale aromatic polyamide particles. *Polym.* **48** (2007) 2214.

9. A. Anderson, F. Bäckhed, A. Euler, A. Dahlfors, D. Sutherland and B. Kasemo. Nanoscale features influence epithelial cell morphology and cytokine production. *Biomater.* **24** (2003) 3427.

10. O. Karoussi and A. A. Hamouda. Macroscopic and nanoscale study of wettability alteration of oil-wet calcite surface in presence of magnesium and sulfate ions. *J. Colloid Interface Sci.* **317** (2008) 26.

11. V. Bérard, E. Lesniewska, C. Andrès, D. Pertuy, C. Laroche and Y. Pourcelot. Affinity scale between a carrier and a drug in DPI studied by atomic force microscopy. *Int. J. Pharm.* **247** (2002) 127.

12. V. M. Masterson and X. Cao. Evaluating particle hardness of pharmaceutical solids using AFM nanoindentation. *Int. J. Pharm.* **362** (2008) 163.

13. D. E. Packham. Surface energy, surface topography and adhesion. *Int. J. Adhes. Adhes.* **23** (2003) 437.

14. G. T. Barnes and I. R. Gentle. Interfacial science: an introduction. Oxford university press, Oxford, 2005.

15. H. J. Butt, K. Graf and M. Kappl. Physics and chemistry of interfaces.

Wiley-vch 2005.

16. J. N. Israelachvili and B. W. Ninham. Intermolecular forces-the long and short of it. *J. Colloid Interface Sci.* **58** (1977) 14.

17. F. London. The general theory of molecular forces. *Trans. Faraday Soc.* **33** (1937) 8.

18. O. J. Hirschfelder, C. F. Curtiss and R. B. Bird. Molecular theory of gases and liquids. Wiley, New York, 1954.

19. R. J. Good, Surface free energy of solids and liquids: thermodynamics. Molecular forces, and structure. *J. Colloid Interface Sci.* **59** (1977) 398.

20. J. Israelachvili. Intermolecular & Surface Forces 2<sup>nd</sup> Edition, Academic Press, London 1991.

21. M. Battezzati and V. Magnasco. Classical and quantum evaluation in the low temperature limit of the Keesom integral for the interaction between permanent dipoles. *C. R. Chim.* (2008) doi:10.1016/j.crci.2008.09.026.

22. G. A. Jeffrey. An introduction to hydrogen bonding (Topics in physical chemistry) Oxford university press, Oxford, 1997.

23. S. Goswami, S. Jana, S. Dey, D. Sen, H. Fun and S. Chantrapromma. Recognition of a dicarboxylic acid with dipicolyl urea in solution and in solid phase: intramolecular hydrogen bond inhibiting both pyridine nitrogens from binding carboxyl groups. *Tetrahedron* **64** (2008) 6426.

24. J. C. Berg. Wettability (Surfactant science). Marcel Dekker, New York, 1993.

25. T. Young. An essay on the cohesion of fluids. *Phil. Trans. R. Soc.* **95** (1805) 65.
26. R. H. Yoon and S. A. Ravishankar. Long-range hydrophobic forces between mica surfaces in dodecylammonium chloride solutions in the presence of dodecanol. *J. Colloid Interface Sci.* **179** (1996) 391.
27. F. M. Fowkes. Additivity of intermolecular forces at interfaces. I determination of the contribution to surface and interfacial tensions of dispersion forces in various liquids. *J. Phys. Chem.* **67** (1963) 2538.
28. F. M. Fowkes. Donor-acceptor interactions at interfaces. *J. Adhes.* **4** (1972) 155.
29. R. J. Good and C. J. Van Oss. In modern approaches to wettability: theory and applications. Plenum Press. New York. 1992.
30. S. Wu. Polar and nonpolar interactions in adhesion. *J. Adhes.* **5** (1973) 39.
31. E. L. Keijbets, J. Chen, E. Dickinson and J. Vieira. Surface energy investigation of chocolate adhesion to solid mould materials. *J. Food Eng.* **92** (2009) 217.
32. A. M. Raichur, X. H. Wang and B. K. Parekh. Estimation of surface free energy of pyrites by contact angle measurements. *Miner. Eng.* **14** (2001) 65.
33. M. Morra, E. Occhiello and F. Garbassi. Knowledge about polymer surfaces from contact angle measurements. *Adv. Colloid Interface Sci.* **39** (1992) 383.
34. R. Crawford, K. L. Koopal and J. Ralston. Contact angle on particles and

- plates. *Colloids Surf.* **27** (1987) 57.
35. W. Wu, R. F. Giese and C. J. Vanoss. Change in surface-properties of solids caused by grinding. *Powder Technol.* **89** (1996) 129.
36. A. I. Rusanov. Effect of contact line roughness on contact angle. *Mendeleev Commun.* **6** (1996) 30.
37. E. L. Decker, B. Frank, Y. Suo and S. Garoff. Physics of contact angle measurement. *Colloids Surf. A* **156** (1999) 177.
38. A. Gajewski. Contact angle and sessile drop diameter hysteresis on metal surface. *Int. J. Heat Mass Transfer* **51** (2008) 4628.
39. C. W. Extrand and Y. Kumagai. An experimental study of contact angle hysteresis. *J. Colloid Interface Sci.* **191** (1997) 378.
40. C. Della Volpe and S. Sibioni. Some reflection on acid-base solid surface free energy theories. *J. Colloid Interface Sci.* **195** (1997) 121.
41. E. Chibowski and R. Perea-Carpio. Problems of contact angle and solid surface free energy determination. *Adv. Colloid Interface Sci.* **98** (2002) 245.
42. O. Planinšek, A. Trojak and S. Srčič. The dispersive component of the surface free energy of powders assessed using inverse gas chromatography and contact angle measurements. *Int. J. Pharm.* **221** (2001) 211.
43. G. Buckton and H. Gill. The importance of surface energetics of powders for drug delivery and the establishment of inverse gas chromatography. *Adv. Drug Delivery Rev.* **59** (2007) 1474.
44. B. Shi, Q. Zhang, L. Jia and Y. Liu. Surface lewis acid-base properties of

polymers measured by inverse gas chromatography. *J. Chromatogr. A* **1149** (2007) 390.

45. Y. Matsushita, S. Wada, K. Fukushima and S. Tasuda. Surface characteristics of phenol-formaldehyde-lignin resin determined by contact angle measurement and inverse gas chromatography. *Ind. Crops Prod.* **23** (2006) 115.

46. X. Huang, B. Shi, B. Li, L. Li X. Zhang and S. Zhao. Surface characterization of nylon 66 by inverse gas chromatography and contact angle. *Polym. Test.* **25** (2006) 970.

47. P. M. Claesson, T. Ederth, V. berberon and M.W. Rutland. Techniques for measuring surface forces. *Adv. Colloid Interface Sci.* **67** (1996) 119.

48. B. V. Derjaguin, Y. I. Rabinovich and N. V. Churaev. Measurement of forces of molecular attraction of crossed fibres as a function of width of air gap. *Nature* **265** (1977) 520.

49. J. H. Clint. Adhesion and components of solid surface energies. *Current Opinion Colloid Interface Sci.* **6** (2001) 28.

50. M. P. Timsina, G. P. Martin, C. Marriott, D. Ganderton and M. Yianneskis. Drug delivery to the respiratory tract using dry powder inhalers. *Int. J. Pharm.* **101** (1994) 1.

51. S. P. Newman and W. W. Busse. Evolution of dry powder inhaler design, formulation, and performance. *Respir. Med.* **96** (2002) 293.

52. S. Adi, H. Adi, P. Tang, D. Traini, H. Chan and P. M. Young. Micro-particle

corrugation, adhesion and inhalation aerosol efficiency. *Eur. J. Pharm. Sci.* **35** (2008) 12.

53. V. Bérard, E. Lesniewska, C. Andrès, D. Pertuy, C. Laroche and Y. Pourcelot. Dry powder inhaler: influence of humidity on topology and adhesion studied by AFM. *Int. J. Pharm.* **232** (2002) 213.

54. J. A. S. Cleaver and L. Looi. AFM study of adhesion between polystyrene particles;-The influence of relative humidity and applied load. *Powder Technol.* **174** (2007) 34.

55. U. Grüning and A. Yelon. Capillary and Van der Waals Forces and mechanical stability of porous silicon. *Thin Solid Films* **255** (1995) 135.

56. A. Fukunishi and Y. Mori. Adhesion force between particles and substrate in a humid atmosphere studied by atomic force microscopy. *Adv. Powder Technol.* **17** (2006) 567.

57. Q. Ouyang, K. Ishida and K. Okada. Investigation of micro-adhesion by atomic force microscopy. *Appl. Surf. Sci.* **169-170** (2001) 644.

58. J. J. Fitzpatrick, K. Barry, P. S. M. Cerqueira, T. Iqbal, J. O'Neill and Y. H. Roos. Effect of composition and storage conditions on the flowability of dairy powders. *Int. Dairy J.* **17** (2007) 383.

59. C. J. Taylor, L. E. Dieker, K. T. Miller, C. A. Koh and E. D. Sloan Jr., Micromechanical adhesion force measurements between tetrahydrofuran hydrate particles. *J. Colloid Interface Sci.* **306** (2007) 255.

60. M. Meyers and K. Chawla. Mechanical behavior of materials. 2<sup>nd</sup> Edition.

Cambridge University Press. 2009, P71.

61. S. F. Yap, M. J. Adams, J. P. K. Seville and Z. Zhang. Single and bulk compression of pharmaceutical excipients: evaluation of mechanical properties.

*Powder Technol.* **185** (2008) 1.

62. S. Jain. Mechanical properties of powders for compaction and tableting: an overview. *PSTT* **2** (1999) 20.

63. A. R. Najafabadi, K. Gilani, M. Barghi and M. R. Tehrani. The effect of vehicle on physical properties and aerosolisation behaviour of disodium cromoglycate microparticles spray dried alone or with L-leucine. *Int. J. Pharm.* **285** (2004) 97.

64. M. Abdel-Ghani, J. G. Petrie, J. P. K. Seville and R. Clift. Mechanical properties of cohesive particulate solids. *Powder Technol.* **65** (1991) 113.

65. U. D. Schwarz. A generalized analytical model for elastic deformation of an adhesive contact between a sphere and a flat surface. *J. Colloid Interface Sci.* **261** (2003) 99.

66. K. L. Johnson. Contact mechanics. Cambridge University Press. 1985.

67. M. Molotskii, I. Torchinsky and G. Rosenman. Hertz model for contact of water droplet with superhydrophobic surface. *Phys. Lett. A* **373** (2009) 804.

68. H. Butt, B. Cappella and M. Kappl. Force measurements with the atomic force microscope: technique, interpretation and applications. *Surf. Sci. Rep.* **59** (2005) 1.

69. K. L. Johnson, K. Kendall and A. D. Roberts. Surface energy and the

- contact of elastic solids. *Proc. R. Soc. London, Ser. A* **324** (1971) 301.
70. A. Fogden and L. R. White. Contact elasticity in the presence of capillary condensation I the nanoadhesive Hertz problem. *J. Colloid Interface Sci.* **138** (1990) 414.
71. D. Tabor. Surface forces and surface interactions. *J. Colloid Interface Sci.* **58** (1977) 2.
72. R. H. Plaut, S. A. White and D. A. Dillard. Effect of work of adhesion on contact of a pressurized blister with a flat surface. *Int. J. Adhes. Adhes.* **23** (2003) 207.
73. P. Stanley. Mechanical strength testing of compacted powders. *Int. J. Pharm.* **227** (2001) 27.
74. S. BinBaie, J. M. Newton and F. Podczeck. The characterization of the mechanical properties of pharmaceutical materials. *Eur. J. Pharm. Biopharm.* **42** (1996) 138.
75. J. Fraxedas, S. Garcia-Manyes, P. Gorostiza, F. Sanz. Nanoindentation: toward the sensing of atomic interactions. *Proc. Natl. Acad. Sci. USA* **99** (2002) 5228.
76. L. J. Taylor, D. G. Papadopoulos, P. J. Dunn, A. C. Bentham, N. J. Dawson, J. C. Mitchell and M. J. Snowden. Predictive milling of pharmaceutical materials using nanoindentation of single crystals. *Org. Proc. Res. Dev.* **8** (2004) 674.
77. V. M. Masterson and X. Cao. Evaluating particle hardness of

- pharmaceutical solids using AFM nanoindentation. *Int. J. Pharm.* **362** (2008) 163.
78. M. Perkins, S. J. Ebbens, S. Hayes, C. J. Roberts, C. E. Madden, S. Y. Luk and N. Patel. Elastic modulus measurements from individual lactose particles using atomic force microscopy. *Int. J. Pharm.* **332** (2007) 168.
79. X. Liao and T. S. Wiedmann. Characterization of pharmaceutical solids by scanning probe microscopy. *J. Pharm. Sci.* **60** (2004) 2250.
80. K. J. Ramos and D. F. Bahr. Mechanical behavior assessment of sucrose using nanoindentation. *J. Mater. Res.* **22** (2007) 2037.
81. K. M. Picker-Freyer, X. Liao, G. Zhang and T. S. Wiedmann. Evaluation of the compaction of sulfathiazole polymer. *J. Pharm. Sci.* **96** (2007) 2111.
82. G. W. Bao and S. F. Y. Li. Characterization of atomic force microscopy (AFM) tip shapes by scanning hydrothermally deposited ZnO thin films. *Talanta* **45** (1998) 751.
83. M. Radmacher, M. Fritz, J. P. Cleveland, D. A. Walters and P. K. Hansma. Imaging adhesion forces and elasticity of lysozyme adsorbed on mica with the atomic-force microscope. *Langmuir*. **10** (1994) 3809.
84. S. Belikov, S. Magonov, N. Erina, L. Huang, C. Su, A. Rice, C. Meyer, C. Prater, V. Ginzburg, G. Meyers, R. McIntyre and H. Lakrout. Theoretical modeling and implementation of elastic modulus measurement at the nanoscale using atomic force microscope. *J. Phys. Conf. Ser.* **61** (2007) 1303.
85. K. L. Westra and D. J. Thomson. Microstructure of thin films observed

- using atomic force microscopy. *Thin Solid Films* **257** (1995) 15.
86. Y. Yong, W. Hong and D. A. Erie. Quantitative characterization of biomolecular assemblies and interactions using atomic force microscopy. *Methods* **29** (2003) 175.
87. N. Nagashima, S. Matsuoka and K. Miyahara. Nanoscopic hardness measurement by atomic force microscope. *JSME Int. J. A* **39** (1996) 456.
88. N. Jalili, K. Laxminarayana. A review of atomic force microscopy imaging systems: application to molecular metrology and biological sciences. *Mechatronics* **14** (2004) 907.
89. S. R. Cohen and A. Bitler. Use of AFM in bio-related systems. *Current Opinion Colloid Interface Sci.* **13** (2008) 316.
90. A. D. L. Humphris, M. J. Miles and J. K. Hobbs. A mechanical microscope: high-speed atomic force microscopy. *Appl. Phys. Lett.* **86** (2005) 034106.
91. A. Alessandrini and P. Facci. AFM: a versatile tool in biophysics. *Meas. Sci. Technol.* **16** (2005) 65.
92. R. Lal and S. A. John. Biological application of atomic force microscopy. *Am. J. Physiol.* **266** (1994) 1.
93. B. Bhushan, M. Palacio and B. Kinzig. AFM-based nanotribological and electrical characterization of ultrathin wear-resistant ionic liquid films. *J. Colloid Interface Sci.* **317** (2008) 275.
94. J. A. Dvorak. The application of atomic force microscopy to the study of living vertebrate cells in culture. *Methods.* **29** (2003) 86.

95. C. Espenel, M. Giocondi, B. Seantier, P. Dosset, P. Milhiet and C. L. Grimmler. Temperature-dependent imaging of living cells by AFM. *Ultramicroscopy* **108** (2008) 1174.
96. J. A. Chouinard, G. Grenier, A. Khalil and P. Vermette. Oxidized-LDL induce morphological changes and increase stiffness of endothelial cells. *Exp. Cell Res.* **314** (2008) 3007.
97. Y. L. Lyubchenko. DNA structure and dynamics: an atomic force microscopy study. *Cell Biochem. Biophys.* **41** (2004) 75.
98. Y. L. Lyubchenko and L. S. Shlyakhtenko. AFM for analysis of structure and dynamics of DNA and protein-DNA complexes. *Methods* (2008) doi:10.1016/j.ymeth.2008.09.002.
99. X. Xiong, H. Li and E. Cao. PIG11 protein binds to DNA in sequence-independent manner in vitro. *Biochem. Biophys. Res. Commun.* **358** (2007) 29.
100. M. Murakami, I. Narumi, K. Satoh, A. Furukawa and I. Hayata. Analysis of interaction between DNA and *Deinococcus radiodurans* PprA protein by atomic force microscopy. *Biochim. Biophys. Acta* **1764** (2006) 20.
101. J. Thirlway, I. J. Turner, C. T. Gibson, L. Gardiner, L. Brady, S/ Allen, C. J. Roberts and P. Sultanas. *Nucleic Acids Res.* **31** (2003) 4001.
102. M. Tanaka, M. Komagata, M. Tsukada and H. Kamiya. Evaluation of the particle-particle interactions in a toner by colloid probe AFM. *Powder Technol.* **183** (2008) 273.

103. W. Zhang, C. Machón, A. Orta, N. Phillips, C. J. Roberts, S. Allen and P. Soutanas. Single-molecule atomic force spectroscopy reveals that DnaD forms scaffolds and enhances duplex melting. *J. Mol. Biol.* **377** (2008) 706.
104. D. Hu, M. Micic, N. Klymyshyn, Y. D. Suh and H. P. Lu. Correlated topographic and spectroscopic imaging by combined atomic force microscopy and optical microscopy. *J. Lumin.* **107** (2004) 4.
105. S. Kondra, J. Laishram, J. Ban, E. Migliorini, V. D. Foggia, M. Lazzarino, V. Torre and M. E. Ruaro. Integration of confocal and atomic force microscopy images. *J. Neurosci. Methods* **177** (2009) 94.
106. S. C. Strathmann, M. A. Murphy, B. A. Goeckner, P. W. Carter and J. D. Green. Forces between insulin microspheres and polymers surfaces for a dry powder inhaler. *Int. J. Pharm.* **372** (2009) 147.
107. H. Yang and Y. Wang. Effects of concentration on nanostructural images and physical properties of gelatin from channel catfish skins. *Food Hydrocolloids* **23** (2009) 577.
108. E. K. Wasan, K. Bartlett, P. Gershkovich, O. Sivak, B. Banno, Z. Wong, J. Gagnon, B. Gates, C. G. Leon and K. M. Wasan. Development and characterization of oral lipid-based Amphotericin B formulations with enhanced drug solubility, stability and antifungal activity in rats infected with *Aspergillus fumigatus* or *Candida albicans*. *Int. J. Pharm.* **372** (2009) 76.
109. M. A. Deji, J. van Eupen, H. Meeke, P. Verwer, P. Bennema and E. Vlieg. Experimental and computational morphology of three polymorphs of the free

base of Venlafaxine: A comparison of morphology prediction methods. *Int. J. Pharm.* **353** (2008) 113.

110. C. Thompson, M. C. Davies, C. J. Roberts, S. J. B. Tendler and M. J. Wilkinson. The effects of additives on the growth and morphology of paracetamol (acetaminophen) crystals. *Int. J. Pharm.* **280** (2004) 137.

111. T. D. Dincer, M. I. Ogden and G. M. Parkinson. Crystal growth mechanisms of the (0 1 0) face of  $\alpha$ -lactose monohydrate crystals. *J. Cryst. Growth* (2009), doi:10.1016.

112. V. Berard, E. Lesniewska, C. Andres, D. Pertuy, C. Laroche and Y. Pourcelot. Dry powder inhaler: influence of humidity on topology and adhesion studied by AFM. *Int. J. Pharm.* **232** (2002) 213.

113. Q. Li and V. Rudolph. London-van der Waals adhesiveness of rough particles. *Powder Technol.* **161** (2006) 248.

114. W.A. Ducker, T.J. Senden and R.M. Pashley. Direct measurement of colloidal forces using an atomic force microscope, *Nature* **353** (1991) 239.

115. C. M. Niemeyer. Nanoparticles, protein, and nucleic acid: biotechnology meets materials science. *Angew. Chem. Int. Ed. Engl.* **40** (2001) 4128.

116. C. E. McNamee, N. Pyo and K. Higashitani. Atomic force microscopy study of the specific adhesion between a colloid particle and a living melanoma cell: effect of the charge and the hydrophobicity of the particle surface. *Biophys. J.* **91** (2006) 1960.

117. J. Ralston, I. Larson, M. W. Rutland, A. A. Feiler and M. Kleijn. Atomic

force microscopy and direct surface force measurements. *Pure Appl. Chem.* **77** (2005) 2149.

118. M. E. Schroder. Work of adhesion of a sessile drop to a clean surface. *J. Colloid Interface Sci.* **213** (1999) 602.

119. B. J. R. Thio and J. C. Meredith Measurement of polyamide and polystyrene adhesion with coated-tip atomic force microscopy. *J. Colloid interface Sci.* **314** (2007) 52.

120. G. Gillies and C. A. Prestidge. Interaction forces, deformation and nano-rheology of emulsion droplets as determined by colloid probe AFM. *Adv. Colloid Interface Sci.* **108-109** (2004) 197.

121. F. Podczec, J. M. Newton and M. B. James. Influence of relative humidity of storage air on the adhesion and autoadhesion of micronized particles to particulate and compacted powder surfaces. *J. Colloid Interface Sci.* **187** (1997) 484.

122. F. Podczec, J. M. Newton and M. B. James. Variations in the adhesion force between a drug and carrier particles as a result of changes in the relative humidity of the air. *Int. J. Pharm.* **149** (1997) 151.

123. M. Farshchi-Tabrizi, M. Kappl, Y. J. Cheng, J. Gutmann and H. Butt. On the adhesion between fine particles and nanocontacts: an atomic force microscope study. *Langmuir* **22** (2006) 2171.

124. N. A. Burnham, D. D. Dominguez, R. L. Mowery and R. J. Colton. Probing the surface forces of monolayer films with an atomic-force microscope.

*Phys. Rev. Lett.* **64** (1990) 1931.

125. S. Biggs and G. Spinks. Atomic force microscopy investigation of the adhesion between a single polymer sphere and a flat surface. *J. Adhes. Sci. Technol.* **12** (1998) 461.

126. J. C. Hooton, C. S. German, M. C. Davies and C. J. Roberts. A comparison of morphology and surface energy characteristics of sulfathiazole polymerphs based upon single particle studies. *Eur. J. Pharm. Sci.* **28** (2006) 315.

127. J. Drelich, G. W. Tormoen and E. R. Beach. Determination of solid surface tension from particle-substrate pull-off forces measured with the atomic force microscope. *J. Colloid Interface Sci.* **280** (2004) 484.

128. A. E. Ghzaoui. Determination of surface energy of polymers by force microscopy. *J. Appl. Phys.* **85** (1999) 1231.

129. J. Zhang, S. Ebbens, X. Chen, Z. Jin, S. Luk, C. Madden, N. Patel and C. J. Roberts. *Pharm. Res.* **23** (2006) 401.

130. Z. Tüske, G. Regdon Jr., I. Erős, S. Srčić and K. Pintye-Hódi. The role of the surface free energy in the selection of a suitable excipient in the course of a wet-granulation method. *Powder Technol.* **155** (2005) 139.

131. A. Barth. Infrared spectroscopy of proteins. *Biochim. Biophys. Acta* **1767** (2007) 1073.

132. Y. Roggo, P. Chalus, L. Maurer and C. L. Martinez, A. Edmond and N. Jent. A review of near infrared spectroscopy and chemometrics in

- pharmaceutical technologies. *J. Pharm. Biomed. Anal.* **44** (2007) 683.
133. D. Steele, in: J. M. Chalmers, P. R. Griffiths (Eds), Handbook of vibrational spectroscopy. John Wiley & Sons, London, (2002) 44.
134. C. Jarusutthirak, G. Amy and J. P. Croué Fouling characteristics of wastewater effluent organic matter (EfOM) isolates on NF and UF membranes. *Desalination* **145** (2002) 247.
135. C. Gendrin, Y. Roggo and C. Collet. Pharmaceutical applications of vibrational chemical imaging and chemometrics: A review. *J. Pharm. Biomed. Anal.* **48** (2008) 533.
136. P. J. Treado, I. W. Levin and E. N. Lewis. Near-infrared acousto-optic filtered spectroscopic microscopy: A solid-state approach to chemical imaging. *Appl. Spectrosc.* **46** (1992) 553.
137. J. Chen and X. Z. Wang. A new approach to near-infrared spectral data analysis using independent component analysis. *J. Chem. Inf. Comput. Sci.* **41** (2001) 992.
138. N. K. Ebube, S. S. Thosar, R. A. Roberts, M. S. Kemper, R. Rubinovitz, D. L. Martin, G. E. Reier, T. A. Wheatley and A. J. Shukla. Application of near-infrared spectroscopy for nondestructive analysis of Avicel powders and tablets. *Pharm. Dev. Technol.* **4** (1999) 19.
139. C. Ravn, E. Skibsted and R. Bro. Near-infrared chemical imaging (NIR-CI) on pharmaceutical solid dosage forms-comparing common calibration approaches. *J. Pharm. Biomed. Anal.* **48** (2008) 554.

140. D. E. Bugay. Characterization of solid-state: spectroscopic techniques. *Adv. Drug Delivery Rev.* **48** (2001) 43.
141. S. Šašić, H. Sato, M. Shimoyama and Y. Ozaki. Two-dimensional (2D) correlation coefficient analyses of heavily overlapped near-infrared spectra. *Analyst* **130** (2005) 652.
142. J. Wang, Y. Geng, B. Guo, T. Klima, B. N. Lal, J. T. Willerson and W. Casscells. Near-infrared spectroscopic characterization of human advanced atherosclerotic plaques. *J. Am. Coll. Cardiol.* **39** (2002) 1305.
143. A. M. Belu, D. J. Graham and D. G. Castner. Time-of-flight secondary ion mass spectrometry: techniques and applications for the characterization of biomaterial surfaces. *Biomater.* **24** (2003) 3635.
144. A. Belu, C. Mahoney and K. Wormuth. Chemical imaging of drug eluting coatings: combining surface analysis and confocal Raman microscopy. *J. Controlled Release* **126** (2008) 111.
145. <http://www.ion-tof.com/technique-IONTOF-TOF-SIMS-TIME-OF-FLIGHT-SURFACE-ANALYSIS.htm>
146. J. Clerc, C. Fourré And P. Fragu. SIMS microscopy: methodology, problems and perspectives in mapping drugs and nuclear medicine compounds. *Cell Biol. Int.* **21** (1997) 619.
147. R. M. A. Heeren, D. F. Smith, J. Stauber, B. Kükrer-Kaletas and L. MacAleese. Imaging Mass Spectrometry: Hype or Hope. *J. Am. Soc. Mass. Spectrom.* **20** (2009) 1006.

148. J. C. Feldner, M. Ostrop, O. Friedrichs, S. Sohn, D. Lipinsky, U. Gunst and H. F. Arlinghaus. TOF-SIMS investigation of the immobilization process of peptide nucleic acid. *Applied Surface Sci.* **203-204** (2003) 722.
149. T. Amemiya, H. Gong, K. Takaya, M. Tozu and Y. Ohashi. Changes of vitamins A and E in the rat retina under light and dark conditions detected with ToF-SIMS. *Applied Surface Sci.* **203-204** (2003) 738.
150. R. M. A. Heeren, L. A. McDonnell, E. Amstalden, S. L. Luxembourg, A. F. M. Altelaar and S. R. Piersma. Why do not biologists use SIMS A critical evaluation of imaging MS. *Applied Surface Sci.* **252** (2006) 6827.
151. E. A. Jones, J. S. Fletcher, C. E. Thompson, D. A. Jackson, N. P. Lockyer and J. C. Vickerman. ToF-SIMS analysis of bio-systems: Are polyatomic primary ions the solution. *Applied Surface Sci.* **252** (2006) 6844.
152. A. P. Nair, B. J. Tyler and R. E. Peterson. Application of a cryo-stage in the TOF-SIMS analysis of atmospheric aerosol surfaces. *Applied Surface Sci.* **231-232** (2004) 538.
153. G. Buckton and A. E. Beezer. The applications of microcalorimetry in the field of physical pharmacy. *Int. J. Pharm.* **72** (1991) 181.
154. H. Brittain, S. Bogdanowich, D. Bugay, J. DeVincentis, G. Lewen and A. Newman. Physical characterization of pharmaceutical solids. *Pharm. Res.* **8** (1991) 963.
155. F. Delogu. On the relationship between the mechanical and the thermal instabilities of crystalline lattices. *Mater. Sci. Eng., A* **403** (2005) 48.

156. A. A. van Dooren and B. W. Müller. Purity determinations of drugs with differential scanning calorimetry (DSC)-a critical review. *Int. J. Pharm.* **20** (1984) 217.
157. L. Yu, S. M. Reutzel and G. A. Stephenson. Physical characterization of polymorphic drugs: an integrated characterization strategy. *PSTT* **1** (1998) 118.
158. J. Jackle. Models of the glass transition. *Rep. Prog. Phys.* **49** (1986) 171.
159. G. W. H. Höhne, W. F. Hemminger and H. J. Flammersheim. Differential scanning calorimetry, second edition. Springer London, 2003.
160. B. Srinivasulu, P. Raghunath, E. V. Sundaram. Synthesis and characterization of ethyl methacrylate-acrylamide copolymers, *J. Appl. Polym. Sci.* **43** (2003) 1521.
161. J. Zhang, N. Botterill, C. Roberts and D. Grant. Micro-thermal analysis of NiTi shape memory alloy thin films. *Thermochim. Acta* **401** (2003) 111.
162. R. B. Dinwiddie, R. J. Pylkki and P. E. West. Thermal conductivity contrast imaging with a scanning thermal microscope. *Therm. Conductivity* **22** (1994) 668.
163. F. A. Guo, K. Y. Zhu, N. Trannoy and J. Lu. Examination of thermal properties by scanning thermal microscopy in ultrafine-grained pure titanium surface layer produced by surface mechanical attrition treatment. *Thermochim. Acta* **419** (2004) 239.
164. H. Fischer. Quantitative determination of heat conductivities by scanning thermal microscopy. *Thermochim. Acta* **425** (2005) 69.

165. P. G. Royall, V. L. Hill, D. Q. M. Craig, D. M. Price and M. Reading. An investigation into the surface deposition of progesterone on poly(D, L-)lactic acide microspheres using micro-thermal analysis. *Pharma. Res.* **18** (2001) 294.
166. G. H. W. Sanders, C. J. R. Roberts, A. Danesh, A. J. Murray, D. M. Price, M. C. Davies, S. J. B. Tendler and M. J. Wilkins. Discrimination of polymorphic forms of a drug product by localized thermal analysis. *J. Microscopy* **198** (2000) 2.
167. A. Altes, K. Mutamba, R. Heiderhoff, H. L. Hartnagel and L. J. Balk. Scanning near field thermal microscopy on a micromachined thin membrane. *Superlattices Microstruct.* **35** (2004) 465.
168. L. T. Germinario. Nano thermal analysis of chemicals, polymers, thin films and coating. *Microsc. Microanal.* **13** (2007) 1590.
169. Technical Note from Anasys Instruments website:  
<http://www.anasysinstruments.com/nano-TA2.pdf>

## Chapter 2: Materials and Methods

### 2.1 Materials

An API (AZD3409) in HCl salt form and malate salt form were provided by AstraZeneca (Macclesfield, UK). In addition, a number of tablet formulations of these APIs pre and post stability testing were also given. The excipients employed in these tablets were lactose monohydrate, Avicel™ (Microcrystalline Cellulose, MC), Hydroxypropyl Methylcellulose (HPMC), Dibasic Calcium Phosphate Dihydrate (DCPD), Polyvinyl Pyrrolidone (PVP), and Magnesium Stearate (MS). Silicon wafers were purchased from Rockwood (Riddings, UK). Tap300 and FESP AFM tips were from Budget Sensors (Sofia, Bulgaria). A TGT1 tip radius calibration grating was from NT-MDT (Moscow, Russia). Deionized water was prepared using an ELGA LabWater system (ELGA, UK). Formamide and diiodomethane used in the contact angle measurements were purchased from Sigma-Aldrich (Gillingham, UK). Potassium bromide (KBr) used in infrared discs preparation was purchased from Sigma-Aldrich. Materials used for nano-thermal calibration: Polycaprolactone (PCL), Polyethylene (PE) and Polyethylene terephthalate (PET) polymer films were supplied by Anasys Instruments (Norwich, UK). Further calibration materials used in micron-thermal analysis: biphenyl, benzyl and benzoic acid were purchased from Sigma-Aldrich. Ethanol (70%) used in the lactose monohydrate recrystallization and heptane (99%) used in the slurry mixing

method were purchased from Fisher Scientific (Loughborough, UK). AFM images were analyzed by the image analysis software Scanning Probe Image Processor (SPIP) (Image Metrology, Denmark) and NanoScope V510 and V710 offline version (Veeco, US). The AFM probes which need UV cleaning are treated by an UV tip cleaner (Bioforce Nanosciences, IA, US).

### **2.1.1 Samples for AFM Surface Free Energy and Mechanical (Young's modulus) Measurements**

APIs and excipients (~0.2 g) powders were slightly compressed by hand between two cleaned glass slides. The thin layers of samples were transferred onto one side of double-sided carbon sticky tape mounted on the AFM samples holder discs.

### **2.1.2 Samples for Contact Angle Measurements**

The HCl and Malate salt forms together with lactose monohydrate, MC, HPMC, DCPD, PVP and MS (~0.5 g) were compressed into 13mm discs using a die at 10 tons pressure. Three discs for each material were prepared.

### **2.1.3 Lactose Recrystallization for Nano-Thermal Analysis**

The lactose supersaturated solutions were made by adding lactose monohydrate

powder (10 g) to DI water (3 ml). The clear solutions (~20  $\mu$ l) were placed on to a cleaned glass slide overnight in an anti-solvent (ethanol) vapour environment [1]. The resultant recrystallized lactose monohydrate crystals were harvested. Large and clean single tomahawk [2] shaped lactose crystals were selected for nano-TA thermal analysis.

#### **2.1.4 Model Formulation for AFM Adhesion Force Mapping and Nano-Thermal Analysis**

AZD 3409 malate salt form and lactose monohydrate were selected as the components in a model formulation. The two materials were mixed in the weight ratio of 20:80, 50:50 and 80:20 w/w. Slurry mixtures were prepared by adding heptane into powder mixtures and stirred on the magnetic plate. The slurry mixtures were dried using a vacuum filter. Dry slurry mixtures (~1 g) were compressed into 13 mm discs at 10 tons pressure by a die.

## **2.2 Atomic Force Microscopy**

AFM is a direct descendent of the Scanning Tunneling Microscope (STM), and allows the measurement of three dimensional surface structure. AFM can achieve high resolution (lateral ~ 1 nm, vertical ~ 0.1 nm), obtain the sample topography without surface treatment or coating, and acquire the images within a liquid medium [3]. In addition to imaging, AFM can measure the surface

frictional and adhesion properties from single point interactions [4].

The basic configuration of an AFM is shown as Figure 2.1. AFM creates three-dimensional representations of a sample surface by monitoring the forces of interactions experienced between the sample and a sharp probe as it scans the surface. This relative motion is performed with sub-Ångström accuracy by a piezoelectric ceramic scanner, usually in the form of a hollow cylinder. Interactions with the sample deflect the cantilever allowing the tip-sample interactions to be monitored with high resolution by exploiting a laser beam reflecting from the back of the cantilever to a split photodetector. While scanning, the computer and feedback control circuits will adjust the interaction between tip and sample to a fixed pre-set value by sensing the cantilever deflection.

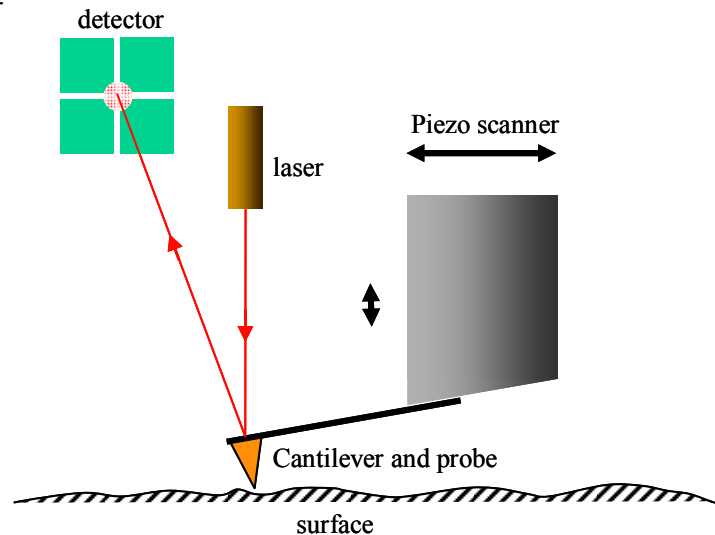


**Figure 2.1** A simple illustration of the main components of AFM. The detector records the changes of laser spot which caused by the movement of probes while the piezo scanner scans over the sample surface. In this manner, a representation of surface topography in X, Y

and Z directions will be generated by computer.

In this work, most topography data were obtained using either a Multimode AFM with Nanoscope IIIa, IV or V controllers or a Dimension 3000 with a Nanoscope IIIa controller (Veeco). The mechanical properties (Young's modulus) were measured using a Multimode AFM with a Nanoscope IIIa controller. The AFM hot-stage sample holder could be heated up to 250 °C in air and was used in investigating mechanical properties with temperature. The adhesion forces between probes and sample surfaces were measured using an EnviroScope AFM with a Nanoscope IIIa controller (Veeco, CA, USA) and a humidity controller (Triton Technology, UK).

### **2.2.1 AFM Imaging**

AFM obtains the topography mainly through two modes: contact and tapping. In contact mode, the probe is constantly in contact with a surface. It is the highest resolution mode of operation but can damage the surface of soft specimens due to the applied lateral force loads. The cantilevers used in contact mode AFM are typically in the shape of triangle with spring constants in the range of 0.1-1 N/m. Figure 2.2 shows a typical contact mode AFM probe. In contact mode the cantilever deflection is sensed and compared in a DC feedback amplifier to desired setpoint value. When the deflection becomes different from the setpoint (say due to topography changes) the feedback

amplifier will apply a voltage to the scanner to adjust the relative position between the sample surface and probe to restore the setpoint value of deflection. In tapping mode, the cantilevers are normally in the shape of single beam with a high spring constant typically above 20 N/m. The cantilevers are oscillated at or close to their resonant frequency with the probes touching the sample surface at the low points in their oscillation cycle. The amplitude of oscillation is maintained by a feedback loop. When the probe scans over a raised feature in the surface, the cantilever has less space to oscillate and the amplitude decreases (assuming homogeneous surface properties). In contrast, amplitude increases when the probe scans over a depression. The change of amplitude is recorded to identify and measure the surface features. This type of working mode overcomes the influence of lateral forces such as friction forces between probes and sample surfaces and can obtain high quality images on softer samples [5]. In addition to sample topography, tapping mode can obtain the phase images which are generated by comparing the driving signal with the phase of cantilever oscillation. The phase lag of the cantilever oscillation is simultaneously monitored by the Extender Electronics Module (Veeco). The phase images which reflecting the nature and level of interactions between AFM probes and sample surfaces have, for example, provided information in polymer nanoscale composition [6].

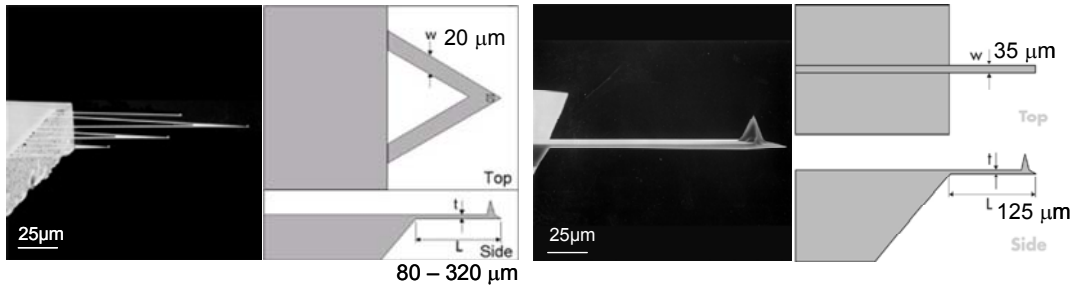


**Figure 2.2** SEM image and Schematic of contact mode V-shape (left) and tapping mode cantilever (right) (images from Veeco <http://www.veecoprobes.com/>).

### 2.2.2 AFM Force Measurements

One great advantage of AFM is the ability to carry out high sensitivity local force measurements. Though both modes of operation can measure the forces between the probes and surfaces, contact mode is preferred. The direct result of such a force measurement is the detector signal in volts,  $\Delta V$  versus the position of the piezo scanner,  $\Delta Z$ , normal to the surface (Figure 2.3).

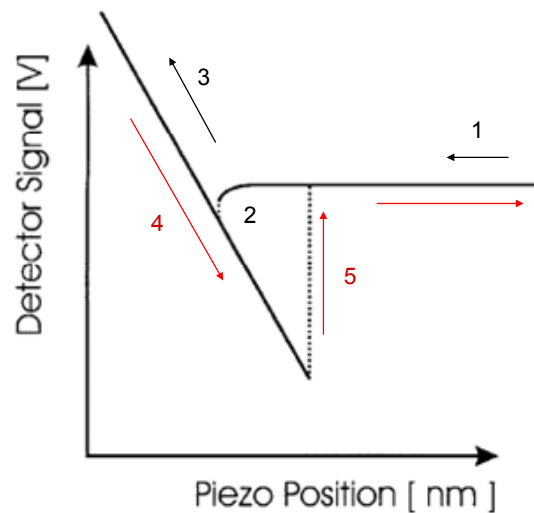


**Figure 2.3** Schematic of a deflection signal versus piezo scanner position curve. The AFM probe approaches to the surface from position 1 and contacts to the surface at position 2. The probe shall keep pushing

to pre-set loading force and retreat from position 3. The adhesion forces between probe and surface pull the cantilever even after initial contact position 2 until the adhesion can not hold the cantilever at position 5.

The deflection of cantilever can be converted to the force based on Hooke's Law:  $F=k \cdot x$ , where  $k$  is the cantilever's spring constant. The accuracy of force measurement mainly depends on the determination of this spring constant. The methods to acquire the spring constant are: the direct calculation from cantilever material and shape [7], applied exterior force measurement [8] and resonance techniques (Sader method) [9]. Among these methods, the Sader method is well accepted for its convenience and relative precision (15%-20% uncertainty) [10].

By applying the spring constant value to Hooke's Law, a force-distance curve is obtained from the deflection-position curve (Figure 2.4) and the piezo position has been converted to real displacement also. There are two major parts in the force-distance curve: the approach curve and withdrawal curve. However, in real experiments, these two kinds of the curves are often not overlapping.

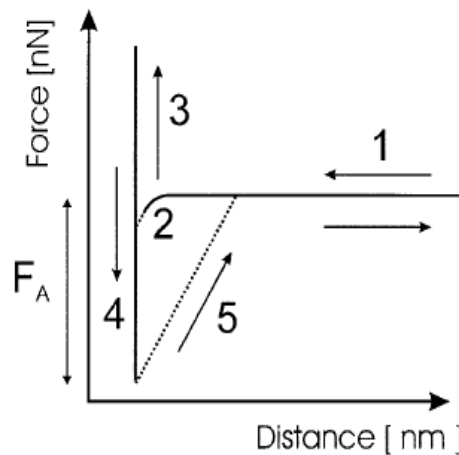


**Figure 2.4** A schematic force-distance curve converted from deflection signal versus piezo scanner position curve in Figure 2.3. The AFM probe approaches to the surface from position 1 and contacts to the surface at position 2. The probe shall keep pushing to pre-set loading force and retreat from position 3. The adhesion forces between probe and surface pull the cantilever even after initial contact position 2 until the adhesion can not hold the cantilever at position 5.

The whole sequence of a force-distance curve is shown in detail in Figure 2.4 as processes 1 to 5:

1. The tip is approaching to the surface but still far from the surface, no deflection occurs.
2. When the tip gets close to the substrate, the surface forces (in this case attractive) will cause a bending of the cantilever towards the surface. Jump to contact.
3. After the tip jumps in to contact with the surface, the tip and surface will move in parallel (no deformation assumed). The resulting linear relationship is corresponding to the so-called constant compliance region [11].

4. Upon retracting from the sample, the tip may adhere to the surface (adhesion force), causing the cantilever to bend downwards.

5. Eventually the bending force will become larger than the adhesive or pull-off force, and the cantilever will snap off the surface into its equilibrium position.

Information about the elastic-plastic behavior of materials can be read from the contact lines of force-distance curves. With the knowledge of probe geometry, by applying the Hertz theory, the Young's moduli ( $E$ ) of crystals, polymers and living cells have been calculated from the force-distance curves with the nanoscale resolution [12-13]. The adhesion force can be directly read from the jump off contact region of force-distance curve.

### **2.3 Nano-Thermal Analysis**

The nano-thermal system used in this work was a Nano-TA2 system (Anasys Instruments, CA, USA) which is an accessory that enables the Multimode AFM to carry out Nano Local Thermal Analysis (NTA) and Scanning Thermal Microscopy (S<sub>Th</sub>M) functions.

In the NTA measurements, a thermal probe (AN-2) is first moved to contact at a selected position. The temperature of probe rises with the increasing voltage while the deflection of cantilever is monitored. At the point of material melting

or phase transition, the material under the probe will soften and the probe will penetrate into the sample surface. The temperature of melting or transition then can be determined from the change of deflection versus temperature curve. In the SThM mode, the probe scans the sample surface in contact mode at a constant temperature. The different power requirements to maintain the probe at that constant temperature are recorded to generate a thermal conductivity map.

The Nano-TA2 provides a higher thermal scan rate (up to 10,000 °C/s) and a higher temperature resolution (0.1°C), and the much higher topography resolution than the original SThM system with an Explorer AFM (Topometrix) due to the microfabricated probe employed (Figure 2.5). In contrast to the previous Wollaston wires of micro-thermal microscopy whose analysis regions are up to 1  $\mu\text{m}^3$  [14], the Nano-TA2 uses silicon probes with tip radii around 30 nm. These sharp tips enable the Nano-TA2 system to achieve a high topographic resolution which is comparable to normal AFM probes, with similar resolution in thermal measurements. NTA has been applied to the characterization of materials in thin films and coatings with high spatial resolution [15]. The application of NTA has for example complemented the Raman imaging to obtain higher spatial resolution in the characterization of polymer blends [14].

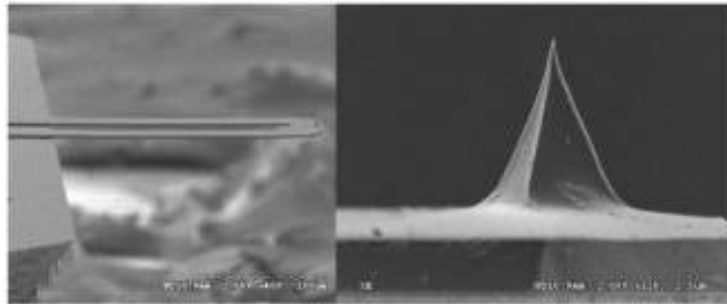


**Figure 2.5** SEM images of Nano-TA2 system AN-2 thermal probe cantilever and tip (images from Anasys Instruments <http://www.anasysinstruments.com/nano-TA2.pdf>).

## 2.4 Contact Angle Measurements

The contact angle instrument used in this work was a CAM200 contact angle goniometer (KSV Instruments, Finland). The experiments were carried out at room temperature, 20-25°C.

When a liquid drop is deposited on a solid substrate, if the liquid does not completely spread on the substrate, a contact angle is formed. Contact angle is geometrically defined as the angle between the liquid side of tangential line and solid intersect. Contact angle is a direct method to measure the interactions between liquids and solids at an interfacial boundary. The magnitude of the contact angle is determined by the interaction forces of interfacial tension of each phase. In Young's equation, this relation can be quantitatively described in Equation 2.1,

$$\gamma_{LV} \cos \theta = \gamma_{SV} - \gamma_{SL} \quad \text{Equation 2.1}$$

Where  $\theta$  is the angle between the solid surface and the tangent to the liquid surface at the line of contact,  $\gamma$  is the interfacial surface free energies.

In practice, contact angle is mostly used to obtain the solid surface free energy by using liquids of known surface tension (energy) as the probes. The surface free energies can be divided into dispersive components and polar components based on the nature of the interactions. The interactions which originate from van der Waals forces belong to the dispersive components of surface free energy while other interactions such as acid/base forces, hydrogen bonding forces and polar forces belong to the polar components. To derive the two components, a harmonic mean is determined via the Wu's equation [16].

$$W_{12} = \gamma_1 (1 + \cos \theta) = \frac{4\gamma_1^d \gamma_2^d}{\gamma_1^d + \gamma_2^d} + \frac{4\gamma_1^p \gamma_2^p}{\gamma_1^p + \gamma_2^p} \quad \text{Equation 2.2}$$

Where  $\gamma^d$  is the dispersion part of surface free energy,  $\gamma^p$  is the polar part of surface free energy.

In this work, water, formamide and diiodomethane were selected as suitable probes. Besides surface free energy measurements, water contact angle itself is also a parameter that can be used to indicate whether the solid surface is hydrophobic or hydrophilic.

There are several methods to measure the contact angle including, the static

sessile drop method, the dynamic sessile drop method, the dynamic Wilhelmy method and the single-fiber Wilhelmy method [17]. In this work, the static sessile drop method was used. A digital camera is used to record the profile of droplet within several seconds. The images were analyzed by the software provided by KSV to obtain the liquid contact angle.

The powdered samples are pressed into discs to minimize the affect of roughness. It should be noted that on rough solid surface, different angles can coexist along the porous contact line which may lead variation in results [18].

## **2.5 Infrared Spectroscopy**

Infrared (IR) spectroscopy is broadly used in pharmaceutical applications to characterize the chemical compositions of materials. With IR spectra, the pharmaceutical materials can be identified by the pattern of absorption bands [19]. The IR region normally refers to the electromagnetic spectrum having wavenumbers from 13,000 to  $10\text{ cm}^{-1}$ . The whole region is divided into three parts: the far ( $400\text{-}10\text{ cm}^{-1}$ ), the mid ( $4000\text{-}400\text{ cm}^{-1}$ ) and the near ( $14000\text{-}400\text{ cm}^{-1}$ ).

IR spectroscopy depends on the fact that molecules will rotate or vibrate at certain frequencies to discrete energy levels when they absorb IR radiation.

Different functional groups absorb the characteristic frequencies of IR. Hence, IR spectroscopic analysis can determine the chemical functional groups in a sample. For the identification purpose, the mid-IR spectra Thermal Nicolet 5700 (Fisher scientific, UK) are employed.

In the near infrared region, the IR beams have higher energy so near infrared (NIR) spectroscopy can excite molecular overtone and combination vibrations. The advantage of NIR is that NIR can penetrate much further into a sample than normal mid-IR radiation which makes NIR a sensitive bulk method to characterize thick materials and bulk materials with little preparation. By using NIR spectra of pure materials, NIR can generate a 2-dimensional material distribution map which will indicate the material distribution in the sub-millimeter range. In this work, a FT-NIR spectrometer PL10 (Perkins, USA) was used to investigate material distribution of mixtures of API and lactose.

Attenuated total reflection infrared (ATR-IR) spectroscopy is another application of IR. In ATR-IR spectroscopy, the IR radiation is passed through an infrared transmitting crystal which is usually made of ZnSe, Ge, silicon or diamond with a high refractive index. The IR beam will internally reflect within the ATR crystal several times. A sample in contact with the ATR crystal will be couple in to evanescent radiation from the crystal. The absorption

spectra from this radiation are hence sensitive to the material properties at this interface region. The ATR-IR instrument used in this work is Thermal Nicolet 6700 (Fisher scientific, UK) with diamond as infrared transmitting crystal.

## **2.6 Other Complementary Characterization Methods**

### **2.6.1 SEM Imaging and Image Analysis**

The SEM images were taken using a JSM-6060LV Scanning Electron Microscope (JEOL, Tokyo, Japan). The samples which were not conductive were gold coated in an argon environment for 3 minutes using a SCD-010 FL9496 Balzers sputter coater (Balzers Union, Liechtenstein).

The SEM images of powder sample were analyzed using ImageJ (NIH Image,US) to obtain the particle size.

### **2.6.2 DSC Thermal Measurements**

Crystalline samples melting points were measured by a differential scanning calorimeter DSC (TA Instruments, CA, USA). The weight of the measured samples was between 1 and 10 mg. The temperature of the DSC chamber was programmed to stay at 25°C for 10 mins and the target temperature was 250 °C. The scan rate for this experiment is 10 °C/min.

### 2.6.3 ToF-SIMS Chemical Mapping

Time-of-Flight Secondary Ion Mass Spectrometer IV (ION-TOF GmbH, Münster, Germany) with a liquid metal ( $\text{Ga}^+$ ) ion gun for imaging were used to investigate the surface molecular distribution in a UHV environment [20]. The measured area for each sample was  $400 \times 400 \mu\text{m}^2$ . After data collection, several typical characteristic peaks for materials were selected to build the surface chemical images which indicated material distribution using the ToF-SIMS software (ION-TOF, Munster, Germany).

## References

1. P. Begat, D. A. V. Morton, J. N. Staniforth and R. Price, The cohesive-adhesive balances in dry powder inhaler formulations I Direct quantification by atomic force microscopy. *Pharm. Res.* **21** (2004) 1591.
2. M. P. Arellano, J. M. Aguilera and P. Bouchon, Development of a digital video-microscopy technique to study lactose crystallization kinetics in situ. *Carbohydr. Res.* **339** (2004) 2721
3. G. Binnig, C. F. Quate and C. Gerber, Atomic force microscope. *Phys. Rev. Lett.*, **56** (1986) 930.
4. Z. Burton and B. Bhushan. Surface characterization and adhesion and friction properties of hydrophobic leaf surfaces. *Ultramicroscopy* **106** (2006) 709.
5. J. Tamayo, R. Garcia, Deformation, contact time, and phase-contrast in tapping mode scanning force microscopy, *Langmuir* **12** (1996) 4430.
6. R. Godehardt, W. Lebek, R. Adhikari, M. Rosenthal, C. Martin, S. Frangov and G.H. Michler, Optimum topographical and morphological information in AFM tapping mode investigation of multicomponent polyethylene, *Eur. Polym. J.* **40** (2004) 917
7. J. E. Sader, Parallel beam approximation for V- shaped atomic force microscope cantilevers, *Rev. Sci. Instrum.* **66** (1995) 4583.
8. J. P. Cleveland, S. Manne, D. Bocek and P. K. Hansma, Nondestructive method for determining the spring constant of cantilevers for scanning force

- microscopy, *Rev. Sci. Instrum.* **64** (1993) 403.
9. J. E. Sader, J. W. M. Chon, and P. Mulvaney, Calibration of rectangular atomic force microscope cantilevers, *Rev. Sci. Instrum.* **70** (1999) 3967.
10. M. Kim, Y. Park, J. Choi and D. Kang, Accurate determination of spring constant of atomic force microscope cantilever and comparison with other methods. *IMEKO XVIII World Congress.* **2006** Brazil.
11. B. Cappella, G. Dietler, Force-distance curves by atomic force microscopy, *Surf. Sci. Rep.* **34** (1999) 1.
12. C. A. Clifford, M. P. Seah, Quantification issues in the identification of nanoscale regions of homopolymers using modulus measurement via AFM nanoindentation, *Appl. Surf. Sci.* **252** (2005) 1915.
13. J. R. Withers, D.E. Aston, Nanomechanical measurements with AFM in the elastic limit, *Adv. Colloid Interface Sci.* **120** (2006) 57.
- 14 G. Meyers, A. Pastzor Jr., and K. Kjoller, Localized thermal analysis: from the micro- to the nanoscale, *Am. Lab.* **39** (2007) 9.
- 15 B. A. Nelson, W. P. King, Thermal analysis with nanoscale spatial resolution using heated probe tips, *Rev. Sci. Instrum.* **78** (2007) 702.
- 16 S. Wu, Calculation of interfacial tension in polymer systems, *J. Polym. Sci.* **C34** (1971) 19.
17. A. J. Milling. Surface characterization methods principles, techniques, and applications. P47 **1999** CRC Press
- 18 D. Quere, Rough ideas on wetting, *Physica A* **313** (2002) 32.

- 19 H. G. Brittain, S. J. Bogdanowich, D. E. Bugay, J. DeVincentis, G. Lewen and A. W. Newman, Physical characterization of pharmaceutical solids, *Pharm. Res.* **8** (1991) 963.
20. A. R. Wood, N. Benedetto, N. Hooker, E. Scullion, P. A. Smith and J. F. Watts. Development of an automated in situ fracture stage for a ToF-SIMS system. *Surf. Interface Anal.* **40** (2008) 1409.

## **Chapter 3: Solid Surface Free Energy Measurements with AFM Adhesion Force and Contact Angle Methods**

### **3.1 Introduction**

In this chapter, two APIs and several excipients used in tablet formulations are measured by AFM adhesion force measurements. The adhesion force results are then derived into surface free energy values by using contact region theory and probe geometry information. The surface free energy values derived from AFM adhesion force measurements are compared with the contact angle method results on the compressed sample discs.

### **3.2 Materials and Methods**

Two APIs namely AZD 3409 malate salt and hydrochloride (HCl) salt (AstraZeneca, Macclesfield) were slightly compressed by hand between two cleaned glass slides for AFM adhesion force measurements. The excipients: lactose monohydrate, dibasic calcium phosphate dihydrate (DCPD), Avicel (Microcrystalline Cellulose, MCC), hydroxypropyl methylcellulose (HPMC), polyvinyl pyrrolidone (PVP) and magnesium stearate (Astrazeneca, Macclesfield) were also compressed as described in section 2.1.1. The same materials were compressed by a 13 mm die for contact angle measurements. Details for the compression process can be found in section 2.1.2.

Before the adhesion force measurements were undertaken, the AFM tapping mode images of each sample were taken with a Multimode AFM (Veeco). The scan size of the tapping mode image selected was  $1\ \mu\text{m} \times 1\ \mu\text{m}$  to correlate with the range used for individual adhesion force measurements. The tapping images were analyzed by the Scanning Probe Image Processor software (Image Metrology A/S, Lyngby, Denmark) to obtain the roughness values. Among several parameters available for roughness assessment, the root mean square (RMS) value, which is most frequently used in AFM force measurements [1], was selected as the parameter to describe the sample surface roughness.

An Environ-Scope AFM (Veeco) with a humidity controller (Triton) was set up to obtain the adhesion forces of samples. The humidity was controlled at below 2% to minimize the capillary forces. Before the force measurements were undertaken on the samples, the deflection sensitivity of the whole AFM system was measured by applying the force measurements on a cleaned silicon wafer surface. The relative deflection of the cantilever over the silicon wafer would also be used to calculate probe penetration depth (Figure 3.1). For each sample, the force measurements were completed by collecting 50 force-distance curves within a  $1\ \mu\text{m} \times 1\ \mu\text{m}$  area. The raw force-distance data were then analyzed by customized macro software developed by Professor X. Chen of the LBSA to acquire the adhesion forces, indentation and modulus information. In the macro, the parameters such as the spring constant and deflection sensitivity need be

inputted in advance and several background fitting methods are available to reduce background noise and achieve better data resolution.

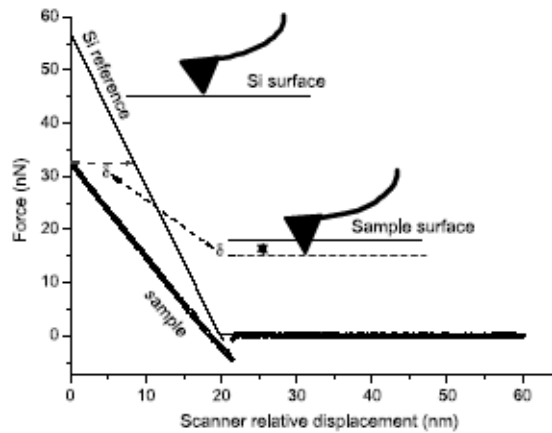


**Figure 3.1** A schematic diagram of probe penetration depth determination. Regardless of probe deformation, the depth is also considered to be probe indentation ( $\delta$ ) [3].

Before and after each batch of force measurements, the AFM probes were examined by the inverse image method which scans the probes over an array of small spikes (TGT1 grating) [2]. The probes that had no changes in geometry during force measurements were valid for the further analysis. In the experiments, the probes should not have significant changes after hundreds of force measurements on those pharmaceutical materials. The geometry of probes including the radius of circular plane ( $r$ ) and area of circular plane ( $A$ ) together with indentation ( $\delta$ ) were used in calculating the contact region radius ( $R$ ). The contact region between the probe and sample surface was simplified to the sphere and plane surface model [3] (Figure 2.2). The contact region radius ( $R$ ) can be derived based on geometry of Figure 3.2 in Equation 3.1,

$$R = \frac{A + \pi\delta^2}{2\pi\delta}$$

Equation 3.1

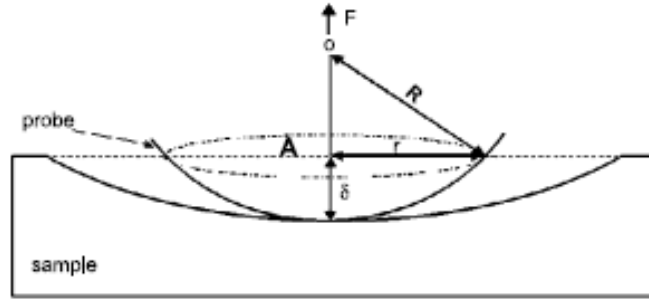


**Figure 3.2** A schematic diagram of contact region radius  $R$  determination based on spherical probe in contact with deformable plane surface.  $r$  is the radius of a circular plane at the cross section of the tip when sample deforms to its maximum extent.  $A$  is the area of the circular plane and  $\delta$  is the probe indentation.  $R$  is the contact region radius [3].

The surface free energy of each sample was calculated from the contact region theory based on Hertz theory [4] and JKR model [5]. The deformation of sample surface was regarded as totally elastic and all the forces that contributed to the adhesion were said to originate within the contact area. Equation 3.2 and 3.3 were employed to calculate the surface free energy of the samples. The details of Equation 3.2 and 3.3 have been described in Chapter 1. The dispersive surface free energy of UV cleaned FESP probe was found to be 42 mJ/m<sup>2</sup> [6].

$$F = \frac{3}{2} \pi R w$$

Equation 3.2

$$w = 2\sqrt{\gamma_1 \cdot \gamma_2}$$

Equation 3.3

Contact angle methods have been described in chapter 2.

### **3.3 Results and Discussions**

#### **3.3.1 AFM Sample Tapping Imaging and Roughness Analysis**

The AFM tapping images of the APIs and excipients were taken by a multimode AFM and analyzed by the SPIP software. The images were flattened by the plane correction function integrated in the SPIP. The final images went through the average profile fit. The tapping images (Figure 3.3 AZD 3409 HCl salt, Figure 3.4 AZD 3409 Malate salt, Figure 3.5 Lactose monohydrate, Figure 3.6 DCPD and Figure 3.7 Magnesium Stearate) were used to calculate the roughness values (RMS) (Table 3.1)

The surface of each sample is shown to be relatively smooth with RMS values ranging from 3 to 20 nm and therefore is suitable for AFM force measurements (see Table 3.1). A typical contact area for one force measurement is below 500 nm<sup>2</sup>. The 1 μm x 1 μm scan size tapping images of all the samples indicate that there are enough areas which are flat and smooth for adhesion force measurements. The roughness value or sample topography plays a great role in contact between probe and surface in the force measurements as was well described by Hooton et al., [7]. Generally speaking, the surface with a high roughness value and the probe with a large radius will decrease the final

adhesion force due to the reduced contact area. For smaller probes, the chances to contact surface asperities become smaller than the large probes, so the contact area will be equal to the theoretical calculation based on the geometry of probes. In AFM force measurements, to obtain accurate adhesion forces and surface free energy values, smaller probes and flat sample surfaces are preferred.

**Table 3.1** Root Mean Square (RMS) roughness values for APIs and excipients

Samples	Roughness (RMS) nm
AZD 3409 HCl salt	12.1
AZD 3409 Malate salt	9.6
Lactose	10.1
DCPD	18.8
Avicel	10.4
PVP	21.9
Magnesium Stearate	3.0
HPMC	18.1

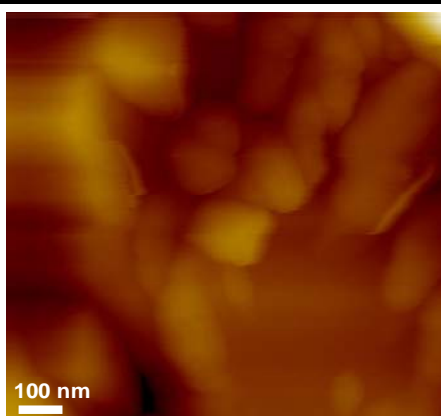


**Figure 3.3** AZD 3409 HCl salt form AFM tapping images. Both images have the scan size: 1  $\mu\text{m}$  x 1  $\mu\text{m}$ .

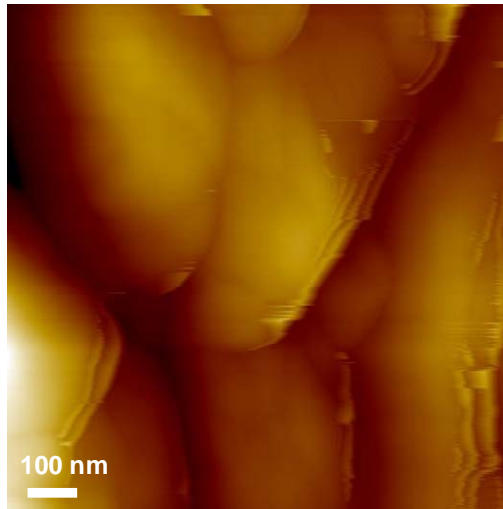


**Figure 3.4** AZD 3409 malate salt form AFM tapping images. Both images have the scan size: 1  $\mu\text{m}$  x 1  $\mu\text{m}$ .

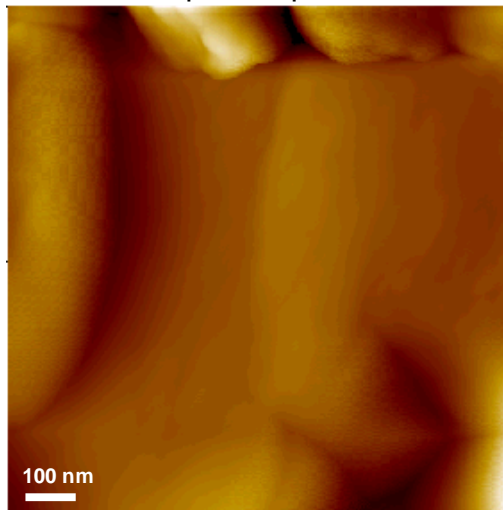


**Figure 3.5** Lactose monohydrate tapping image. The scan size is 1  $\mu\text{m}$  x 1  $\mu\text{m}$ .

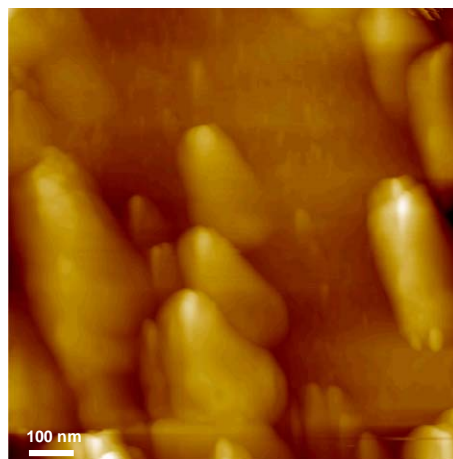


**Figure 3.6** Dibasic calcium phosphate dehydrate tapping image. The scan size is 1  $\mu\text{m}$  x 1  $\mu\text{m}$ .



**Figure 3.7** Magnesium stearate tapping image. The scan size is 1 μm x 1 μm.

### 3.3.2 AFM Adhesion Force Measurements on APIs and Excipients

The deflection sensitivity of the AFM system was assessed by approaching the probes onto the UV cleaned silicon wafer surface. The deflection sensitivity need be collected for each mounted FESP (Force Modulation Etched Silicon Probe) probe correspondingly. For different probes, the mount angle or laser spot position will vary the deflection sensitivity from 50 to 200 nm/V. The sensitivity values were used to calibrate the AFM online measurement system which ensured that the input parameters were transferred from voltage to the spatial position correctly. For off-line analysis, the sensitivity results were used to calculate the probe penetration parameters ( $\delta$ ) as indicated in Figure 3.1.

The spring constant values of FESP probes were calculated by Sader's method [8]. The FESP probes have higher spring constant values than the contact mode probes but in contrast, smaller values than the tapping mode probes. The spring

constant values of FESP used in this experiment range from 1.5 to 3.5 N/m, which are large enough for the nature of the adhesion forces measured between the pharmaceutical materials and still have relatively high sensitivity to achieve better resolution.

The raw data collected from the AFM adhesion force measurements are Top-Bottom deflection signal versus scanner Z displacement curves. Using the macro file (Professor X. Chen, LBSA), input the deflection sensitivity, spring constant and adjust the curves fitting parameters, the original T-B signal versus Z curve (Figure 3.8) is transferred into the force versus Z displacement curve (Figure 3.9). The movement of probe during scanner approach in Z axis should also be considered when the probe indentation parameter is needed for the further calculation. So, in the macro results, the force versus tip-sample distance curve (Figure 3.10) that indicates the real distance between probe and sample surface and therefore, is the most representative so-called force-distance curve in the AFM force measurements.

The adhesion forces for the APIs and excipients are listed in Table 3.2. The absolute results may not be directly compared, because the probes used for adhesion force measurements have different probe apex in geometry, and the probe indentation in each sample is different due to the different loading force and sample mechanical properties. So the adhesion forces results need be

transferred to the surface free energy values to compare the strength of solid-solid interactions. One important fact should be noticed in Table 3.2 is that the deviation of each sample may not just simply indicate the errors in the measurements but also the sample surface heterogeneity caused by measured on different crystal faces or amorphous regions [9]. The samples with large deviation values are usually those materials that have complex surface morphology.

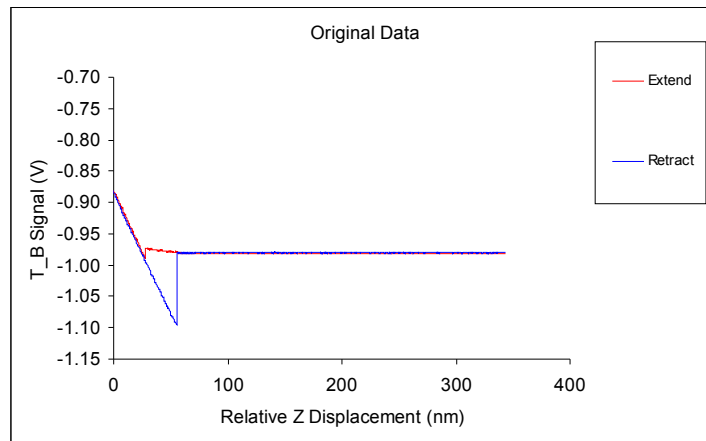


**Figure 3.8** Lactose monohydrate original data: a T-B deflection signal versus relative Z displacement curve collected from a multimode AFM with a FESP probe.

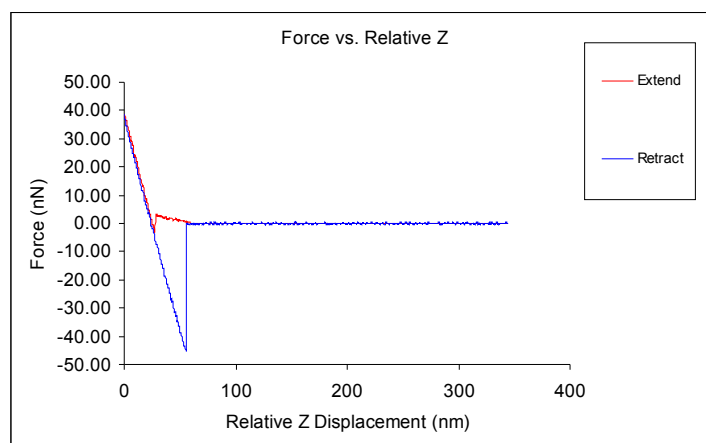


**Figure 3.9** Processed data: the force versus relative Z displacement curve from original data Figure 3.8.

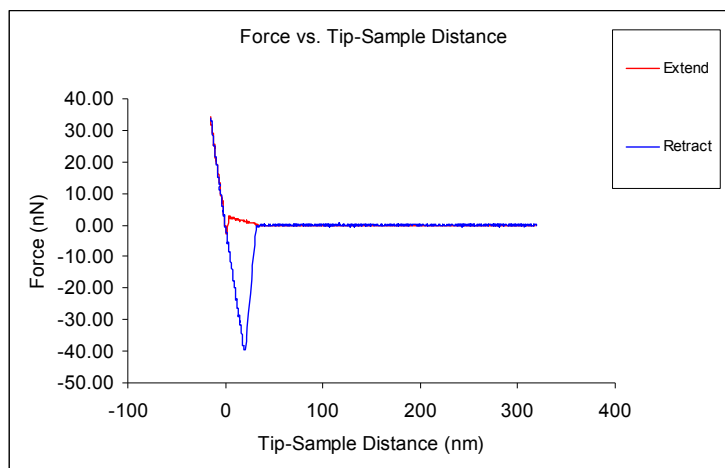


**Figure 3.10** Processed data: the force versus tip-sample distance curve from original data Figure 3.9.

**Table 3.2** Adhesion Forces for APIs and Excipients n=50

Samples	Adhesion Force (nN)
AZD 3409 HCl salt	36.9 (6.8)
AZD 3409 Malate salt	63.6 (7.5)
Lactose	61.5 (7.3)
DCPD	48.3 (9.7)
Avicel	70.3 (7.2)
PVP	88.3 (11.6)
Magnesium Stearate	46.8 (2.1)
HPMC	21.6 (5.2)

### 3.3.3 Surface Free Energy from AFM Force Measurements

The probes profiles were obtained by the reverse imaging method which let the probes scan over an array (TGT1) of small spikes. The TGT1 grating contains spikes with less than 10 nm curvature radius and 3-5  $\mu\text{m}$  in height (Figure 3.11).

The 3-D visualization of scanning probe and tip sharpness parameters can be

determined by the grating.

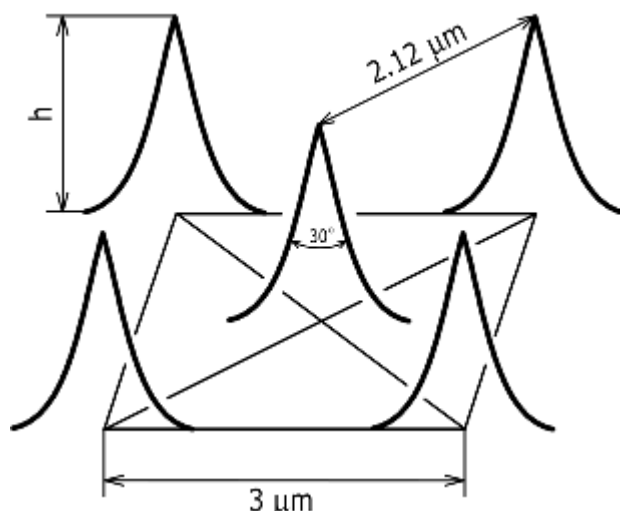


**Figure 3.11** A schematic diagram of TGT1 grating. The period is 3 μm and diagonal period is 2.12 μm. The tip angle is about 30 degrees.

One typical result of reverse imaging can be seen in Figure 3.12. Because the small spikes are not always homogeneous in geometry, the probes reverse images are slightly different in height and radius. In reality the differences are very small and can be minimized by taking the average radius values derived from several probes reverse images. The probe images were analyzed by softwares such as SPIP, nanoscope V510 and V710. The probe circus plane area and probe geometry were determined by software ‘Depth’ and ‘Bear’ functions. The radius of the probe can be calculated based on equation 3.1. The adhesion force and probe radius together can determine the sample surface free energy according to equation 3.2 and 3.3, and the results are presented in Table 3.3. These surface free energy results, which have already normalized the probe geometry and material mechanical properties, can be compared directly.

The materials like PVP and Avicel used in solid formulation as binders have

the highest surface free energy values among all the samples. Magnesium stearate is a hydrophobic lubricant used in tablet formulation so it is not surprise to find the surface free energy value is only  $16.7 \text{ mJ/m}^2$  which is the lowest among all the excipients. The API in malate salt form has a higher surface free energy value than the HCl salt form. Although those two samples both have the same drug base, the binding site between the drug base and the salt is not the same for HCl and malic acid. The differences in the salt form changes the mechanical properties of the drug [10]. So it is found from the data in Table 3.3 that the crystal faces for HCl salt forms can not be the same as malate salt forms. Table 3.3 shows that two salt forms have different surface free energy values and the two drugs are the lowest surface free energy values in the list

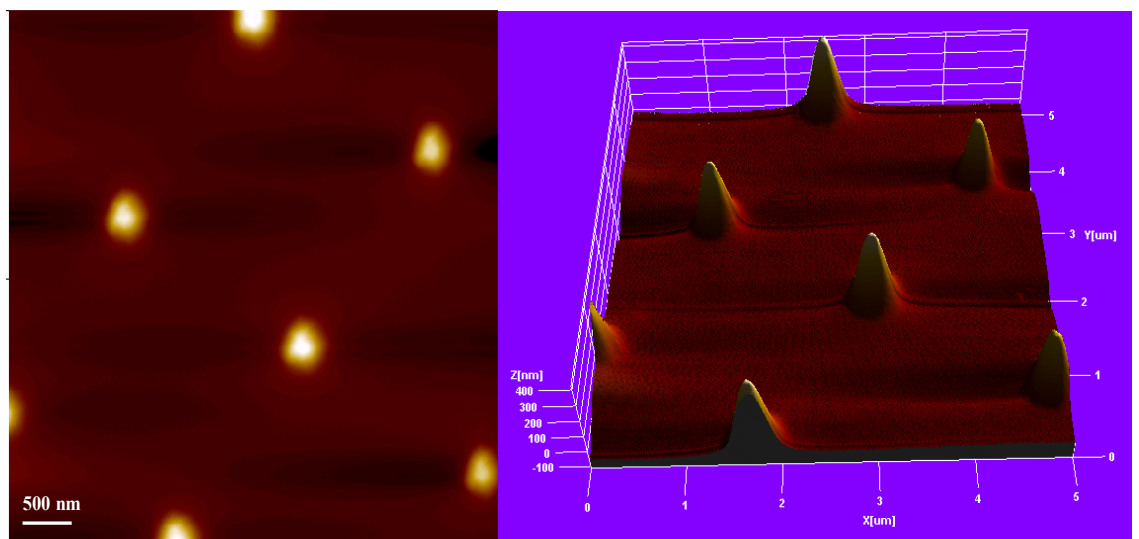


**Figure 3.12** The FESP probe reverse image which generated by scanning over the TGT1 grating. The 3D view of left image is generated by the SPIP.

**Table 3.3** Surface free energy of APIs and Excipients derived from AFM adhesion force measurements in table 3.2 (n=50)

Samples	Surface Free Energy (mJ/m <sup>2</sup> )
AZD 3409 HCL salt	5.3 (0.2)
AZD 3409 Malate salt	12.3 (1.3)
Lactose	33.0 (5.6)
DCPD	27.1 (6.2)
Avicel	39.0 (4.8)
PVP	34.8 (5.7)
Magnesium Stearate	16.7 (2.4)
HPMC	24.6 (2.0)

Because the indentations of each measurements are different so the standard deviations in Table 3.3 are not as much as those in Table 3.2.

### 3.3.4 Surface Free Energy Measured via Contact Angle Measurements

The raw results of contact angle were plotted as 15 angle values taken within 30 seconds of deposition onto the surface (See figure 3.13). Issues arise with this method as the liquid drops tend to evaporate rapidly and for some materials, or samples can dissolve into the contact angle solution. In addition, the shape of the liquid drop always changes with time. To overcome these uncertainties, the contact angle values at initial contact time or 0 seconds were used in the surface free energy calculation. The plots such as Figure 3.13 were used to acquire liquid contact angle measurements at 0 second.

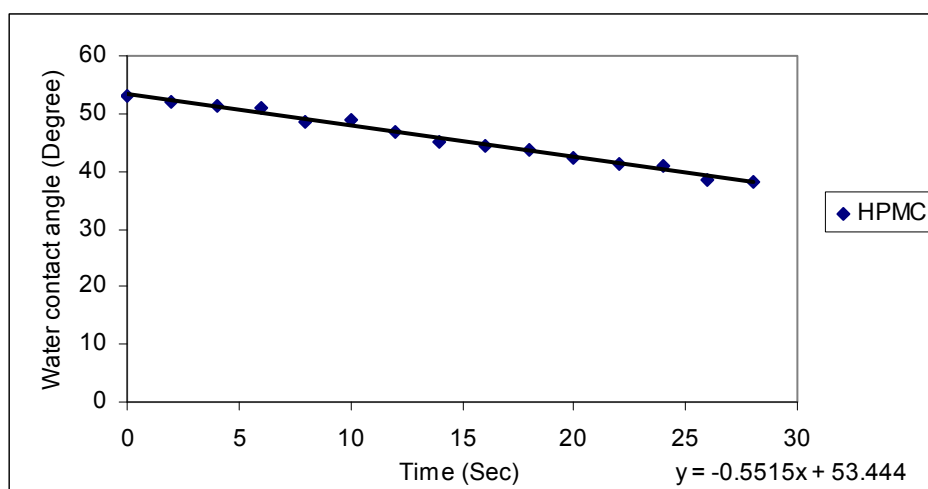


**Figure 3.13** The plot of water contact angle versus time to acquire contact angle of water on HPMC surface at 0 second.

Three liquids were selected as probes to obtain the sample surface free energy values. The properties of the selected liquid probes including their surface free energy are listed in table 3.4. The contact angle results of the 3 liquids on the range of materials are listed in table 3.5. The combination of liquid probes has shown the influence to the final surface free energy calculation so the selection of liquids need be taken care [11]. Normally for samples that have high surface free energy values, diiodomethane should always be chosen as one of the liquids. For those samples that dissolve in more than one liquid probe, other liquid probes such as the homologous series of alkanes can be considered [12]. The surface free energy results from contact angle measurements derived from Wu's equation [13] are presented in table 3.6.

**Table 3.4** Surface free energy and its components values of each liquid probe used in contact angle measurements Unit: mJ/m<sup>2</sup>

Liquids	Surface Energy	Free	Dispersive component ( $\gamma^d$ )	Polar component ( $\gamma^p$ )
Water	72.8		21.8	51.0
Diiodomethane	50.8		50.8	0
Formamide	58.0		39.0	19.0

**Table 3.5** Contact angle results of three liquids on samples (N=5) Unit: °

Samples	Water	Diiodomethane	Formamide
AZD 3409 HCL salt	55.1 (0.5)	25.0 (0.4)	24.6 (0.4)
AZD 3409 Malate salt	40.9 (0.6)	22.8 (0.3)	33.3 (0.2)
Lactose		23.1 (0.1)	13.2 (0.2)
DCPD	9.5 (0.0)	20.0 (0.3)	
Avicel		25.7 (0.3)	14.2 (0.2)
PVP	35.4 (0.6)		40.9 (0.8)
Magnesium Stearate	74.6 (0.4)	55.4 (0.4)	73.9 (0.1)
HPMC	54.8 (0.3)	22.3 (0.7)	22.5 (0.5)

The surface free energy results derived from the contact angle values are compared with the results obtained from the literature in table 3.6. While the values of Avicel agree closely with those from the literature, the values of dispersion surface free energy ( $\gamma^d$ ) for the remainders of the tested samples tend to be higher than the reported values, and the values of polar surface free energy ( $\gamma^p$ ) for Magnesium Stearate and HPMC are higher than the literature values. It must be understood that as the source of the samples, methodologies employed, and environment may be different between the experiment and literature setup, there may be variation between the different data sets.

**Table 3.6** Comparison of literature values of sample surface free energy and contact angle experiment results Unit: mJ/m<sup>2</sup>

Samples	Literature		experiment	
	$\gamma^d$	$\gamma^p$	$\gamma^d$	$\gamma^p$
AZD 3409 HCL salt			45.4	10.3
AZD 3409 Malate salt [14]*	26.9		38.7	21.6
Lactose[15]	43.3	26.1	46.8	12.0
DCPD [12]	21.7	40.8	45.4	32.6
Avicel[16]	43.6	13.2	46.0	12.2
PVP[15]	39.9	10.5	48.9	2.8
Magnesium Stearate[16]	16.8	3.4	25.8	8.4
HPMC[17]	35.8	7.5	47.1	10.1

\* AZD 3409 malate salt surface free energy value is determined by IGC method

### **3.3.5 Surface Free Energy Comparison between AFM Adhesion Force Measurements and Contact Angle measurements**

The surface free energy values derived from AFM force measurements and contact angle measurements may not be comparable for a number of reasons: firstly, the contact angle method is based on the phenomenon that occurs at the three phase (solid-gas-liquid) boundaries. The angle is contributed to the interaction forces between the liquid molecules and the solid molecules at the interface. Since the contact angle values depend on the whole contact area between the liquid and solid interface, the surface free energy values derived from the contact angle measurements are presenting the average interfacial interactions across a surface of dimensions 70  $\mu\text{m}$  diameter. For AFM force measurement, the interaction force is literally the solid-solid interfacial interaction with a definite contact area which is much smaller in comparing. In a specific application such as dry powder inhaler formulation, the surface free energy values derived from the solid-solid interactions based on the AFM measurements may be a better simulation of the interactions within the inhaler device than the values derived from the contact with liquids in the contact angle measurements and so can help selecting the proper combination of drugs and carriers. Another special point about the AFM surface free energy measurement is that the AFM force measurement has a higher spatial resolution. The contact area of 200  $\text{nm}^2$  between AFM probe and sample surface is considerably smaller than the contact angle droplets (70  $\mu\text{m}$  diameter)

which makes the AFM method be the one of choice to identify the small polymorphic differences across a single crystal surface.

In the contact angle method, the surface free energy values are divided into two components namely the dispersive components and polar components. For the interactions between liquid probes and solid surfaces such as hydrogen bonding and metallic interactions, they are attributed to the polar components of surface energy [18]. For the interactions originated from non-covalent and non-electrostatic molecular forces or so called the van der Waals forces, they are attributed to the dispersive components [19]. In the AFM force measurement results, the surface free energy values come from the adhesion forces between AFM probes and solid surfaces within a low relative humidity environment. With such conditions, the adhesion forces are mainly contributed by the van der Waals interactions [20]. So the dispersive components in the contact angle results and surface energy results in the AFM force measurements have the same theoretical origination. If so, then it is possible to compare these two parameters for the same sample.

It is clearly found in table 3.7 that the trend is that the dispersion surface free energy values derived from the AFM adhesion forces are smaller than those from the contact angle experiments. They are generally about 10-15 mJ/m<sup>2</sup> down on the contact angle values and the APIs values are dramatically reduced.

As mentioned above, it is not easy to compare the results derived from the two different methods. Firstly the scales of measurements for these two methods are widely different, in the AFM force measurements the contact area is typically around  $200 \text{ nm}^2$  so the results are representing one phase (layer) rather than the average results around several  $\text{mm}^2$  in the contact angle measurements. The heterogeneity in chemical composition or molecular structure at different length scales can cause a different energy of adhesion and can cause a variation in the effective adhesion force [21]. Secondly, the adhesion forces in AFM measurements are considered as the van der Waals forces only in this work. Although in the experiments the AFM FESP (Silicon) probes are regarded as only having the dispersion interactions with those pharmaceutical samples, they could still be involved in the polar interactions or electrosteric mechanism [22]. Those interactions for most cases are repulsive and will decrease the adhesion forces [23] which could account for the surface free energy values derived from AFM measurements being smaller than contact angle.

It has been found in the literature that the surface free energy values derived from the AFM adhesion force measurements are almost consistent with those from the contact angle method for the cases of polymer samples [24]. The experimental values of work of adhesion for a chemical modified surface system in a liquid medium is very close to the predicted theoretical calculation

value [25]. When measured on metal or crystalline solid samples, no matter in a liquid medium or in air and dry N<sub>2</sub>, the experimental values of surface free energy show relative larger variations with the theoretical calculation values [26, 27]. The variations are much more significant (tens of times) in the case where the probes with big radius were employed [28]. In addition, the surface free energy values of budesonide derived from the AFM adhesion force measurements have broad distribution and they are not consistent with the values derived from IGC measurements [29]. All these measurements and results indicate that first for those polymers films which have homogeneous and repeated surface composition, the AFM adhesion force measurements can provide the similar surface free energy values as the contact angle method. Second for the crystalline solid samples, the AFM adhesion force measurements in most cases provide relative smaller surface free energy values than the contact angle and IGC methods due to the lateral heterogeneous composition and properties along different crystal faces, and the small size (tip contact area of 200 nm<sup>2</sup> in most cases) of measurements in the AFM adhesion force method. The surface free energy values obtained from the AFM adhesion force measurements represent properties of the region on a single face of crystal and a single particle instead of the lateral average properties obtained by the contact angle measurements on the compressed discs. In the application of DPI and pMDI [30] where single particle solid-solid interactions in dry and wet environment are dominant, the AFM adhesion force measurements provide the

surface free energy values which are more suitable to simulate the particle-particle and particle-surface interactions within the devices.

**Table 3.7** Comparison of surface free energy results derived contact angle experiment and AFM adhesion force measurements Unit: mJ/m<sup>2</sup>

Samples	Contact Angle		AFM adhesion
	$\gamma^d$	$\gamma^p$	
AZD 3409 HCL salt	45.4	10.3	5.3
AZD 3409 Malate salt	38.7	21.6	12.3
Lactose monohydrate	46.8	12.0	33.0
DCPD	45.4	32.6	27.1
Avicel	46.0	12.2	39.0
PVP	48.9	2.8	34.8
Magnesium Stearate	25.8	8.4	16.7
HPMC	47.1	10.1	24.6

### 3.4 General Conclusions

To determine a solid material's surface free energy, the AFM adhesion force measurement with very low relative humidity offers an additional choice. The surface free energies are derived from adhesion forces based on Hertz and JKR model. These surface free energy values which represent the solid-solid interactions are obtained on the regions over the scale of just a couple hundreds of nanometers. The same samples have been also measured by contact angle

method to derive the surface free energy values which use liquids as probes and base on the liquid-solid interactions. The size of liquid droplets is usually at the scale of several millimeters. The surface free energy values from two methods above are not easily comparable since the theoretical approaches are different and also they measure the different areas over the surfaces. The results from contact angle measurements are generally larger than that from AFM force measurements. However the dispersive components of contact angle results and surface free energy values of AFM force measurement are both believed to originate from the van der Waals interactions. Based on this point, the comparisons between those two values for the samples are made to verify the AFM force measurements. The AFM results of dispersion surface free energies are still smaller than contact angle derived dispersive component surface free energies. The differences in the scale of measurement and the probe substance between AFM force measurements and contact angle surface free energy measurements are likely to be the main reasons for the surface free energy values variations. However it is not easily to conclude which method has the advantage in the surface free energy determination. For different applications and resolution requirements, the two methods have their own superiority. For those cases where the solid-solid interactions are dominant in the system or the required resolution is at the range of sub-micron, the AFM adhesion force measurements can provide more useful surface free energy values for material selection and heterogeneous detection.

## References

1. A. Vilas, J. M. Bruque and M. L. Martín. Sensitivity of surface roughness parameters to changes in the density of scanning points in multi-scale AFM studies. Application to a biomaterial surface. *Ultramicroscopy* **107** (2007) 617.
2. G. W. Bao and S. F. Y. Li. Characterization of atomic force microscopy (AFM) tip shapes by scanning hydrothermally deposited ZnO thin films. *Talanta* **45** (1998) 751.
3. J. Zhang, S. Ebbens, X. Chen, Z. Jin, S. Luk, C. Madden, N. Patel and C. J. Roberts. Determination of the surface free energy of crystalline and amorphous lactose by atomic force microscopy adhesion measurement. *Pharm. Res.* **23** (2006) 401.
4. M. Abdel-Ghani, J. G. Petrie, J. P. K. Seville and R. Clift. Mechanical properties of cohesive particulate solids. *Powder Technol.* **65** (1991) 113
5. K. L. Johnson, K. Kendall and A. D. Roberts. Surface energy and the contact of elastic solids. *Proc. R. Soc. London, Ser. A* **324** (1971) 301
6. M. L. Gonzalez-martin, B. Janczuk, L. Labajos-broncano, J. M. Bruque and C. M. Gonzalez-Garcia. Analysis of silica surface free energy by the imbibition technique. *J. Colloid Interface Sci.* **240** (2001) 467.
7. J. C. Hooton, C. S. German, S. Allen, M. C. Davies, C. J. Roberts, S. J. B. Tandler and P. M. Williams, Characterization of particle interactions by atomic force microscopy: effect of contact area. *Pharm. Res.* **20(3)** (2003) 508.
8. J. E. Sader, J. W. M. Chon, and P. Mulvaney, Calibration of rectangular

- atomic force microscope cantilevers, *Rev. Sci. Instrum.* **70** (1999) 3967.
9. K. Kimura, K. Kobayashi, H. Yamada and K. Matsushige. High resolution molecular chain imaging of a poly (vinylidene fluoride-trifluoroethylene) crystal using force modulation microscopy. *Nanotechnology* **18** (2007) 305504.
10. R. J. Bastin, M. J. Bowker and B. J. Slater. Salt selection and optimization procedures for pharmaceutical new chemical entities. *Org. Proc. Res. Dev.* **4** (5) (2000) 427.
11. C. Della Volpe and S. Sibioni. Some reflection on acid-base solid surface free energy theories. *J. Colloid Interface Sci.* **195** (1997) 121.
12. I. O. Odidi, J. M. Newton and G. Buckton. The effect of surface treatment on the values of contact angles measured on a compressed powder surface. *Int. J. Pharm.* **72** (1991) 43.
13. S. Wu. Polar and nonpolar interactions in adhesion. *J. Adhes.* **5** (1973) 39.
14. IGC results from Dr. Jennifer Hooton, AstraZeneca.
15. O. Planinšek, R. Pisek, A. Trojak and S. Srčič. The utilization of surface free energy parameters for the selection of a suitable binder in fluidized bed granulation. *Int. J. Pharm.* **207** (2000) 77.
16. N. M. Ahfat, G. Buckton, R. B. Martyn and D. Ticehurst. Predicting mixing performance using surface energy measurements. *Int. J. Pharm.* **156** (1997) 89.
17. P. E. Luner and O. H. Euichaul. Characterization of the surface free energy of cellulose ether films. *Colloids Surf., A* **181** (2001) 31.
18. F. M. Fowkes. Attractive forces at interfaces. *Ind. Eng. Chem.* **56** (12)

(1964) 40.

19. O. Planinšek, A. Trojak and S. Srčič. The dispersive component of the surface free energy of powders assessed using inverse gas chromatography and contact angle measurements. *Int. J. Pharm.* **221** (2001) 211.

20. F. Podczeck, J. M. Newton and M. B. James. Influence of relative humidity of storage air on the adhesion and autoadhesion of micronized particles to particulate and compacted powder surfaces. *J. Colloid Interface Sci.* **187** (1997) 484.

21. M. Farshchi-Tabrizi, M. Kappl, Y. J. Cheng, J. Gutmann and H. Butt. On the adhesion between fine particles and nanocontacts: an atomic force microscope study. *Langmuir* **22** (2006) 2171.

22. R. Ashayer, P. F. Luckham, S. Manimaaran and P. Rogueda. Investigation of the molecular interactions in a pMDI formulation by atomic force microscopy. *Eur. J. Pharm. Sci.* **21** (2004) 533.

23. J. Israelachvili. *Intermolecular & Surface Forces* 2<sup>nd</sup> Edition, Academic Press, London 1991.

24. A. E. Ghzaoui. Determination of surface free energy of polymers by force microscopy. *J. Appl. Phys.* **85** (1999) 1231.

25. S. C. Clear and P. E. Nealey. Chemical force microscopy study of adhesion and friction between surface functionalized with self-assembled monolayers and immersed in solvents. *J. Colloid Interface Sci.* **213** (1999) 238.

26. C. Jacquot and J. Takadoum. A study of adhesion by atomic force

microscopy. *J. Adhes. Sci. Technol.* **14** (2001) 681.

27. F. L. Leite, A. Riul Jr., and P. S. P. Herrmann. Mapping of adhesion forces on soil minerals in air and water by atomic force spectroscopy (AFS). *J. Adhes. Sci. Technol.* **17** (2003) 2141.

28. N. A. Burnham, D. D. Drelich, R. L. Mowery and R. J. Colton. Probing the surface forces of monolayer films with an atomic-force microscope. *Phys. Rev. Lett.* **64** (1990) 1931.

29. M. Davies, A. Brindley, X. Chen, M. Marlow, S. W. Doughty, I. Shrubbs and C. J. Roberts. Characterization of drug particle surface energetics and Young's modulus by atomic force microscopy and inverse gas chromatography. *Pharm. Res.* **22** (2005) 1158.

30. D. Traini, P. Rogueda, P. Yong and R. Price. Surface energy and interparticle force correlation in model pMDI formulations. *Pharm. Res.* **22** (2005) 816.

## **Chapter 4: Colloid Probe AFM Forces Measurements on APIs and Excipients**

### **4.1 Introduction**

In this chapter, the AFM force measurements will be further investigated. In previous chapter, the differences between the surface free energy values derived from the AFM adhesion force and contact angle measurements were discussed. The theoretical approaches of the two methods, the scale of the measurements and the substances of the probes can in part explain the differences in solid surface free energy values derived from those two methods. It should be noticed that in the analysis of the AFM adhesion force measurements, the polar component of surface free energy was ignored. In the very low relative humidity conditions the adhesions are contributed mainly by the van der Waals (dispersion) forces [1, 2]. However, the importance of polar surface free energy in particle-particle interactions within the pMDIs has been emphasized in the research of Traini et al., [3]. In dry air, whether the polar interactions play an important part as in a propellant medium such as HPFP, which has a high polarity and tends to form hydrogen bonds [4], is partly the aim of this chapter. The colloid probe technique in AFM usually refers to the modified probe which is made by gluing a single particle (glass bead) to the end of a normal AFM cantilever. With this technique, the adhesion force measurements will become more easily modeled due to the better defined

geometry. Here colloid probes coated with plasma polymerized hexane, which has only dispersion surface free energy or coated with plasma polymerized allylamine, which has both dispersion and polar surface free energy will be employed to obtain the adhesion forces on the sample surfaces and derive the surface free energies by the method described in Chapter 3. The surface free energies of samples from these two kinds of probes may reveal the strength of polar interactions in the dry environment.

## **4.2 Materials and Methods**

Two APIs: AZD 3409 malate salt form and HCl salt form and excipients: lactose monohydrate, magnesium stearate, Avicel (MCC), hydroxypropyl methylcellulose (HPMC) and dibasic calcium phosphate dihydrate (DCPD) (AstraZeneca, Macclesfield) were compressed into discs by a 13mm die as described in Chapter 2. Silicon wafer samples were cleaned using solvent (water and acetone) and a UV cleaner (Bioforce Nanosciences). Hexane and allylamine were purchased from Fisher Scientific (UK) and Fluka Analytical (UK).

The colloid probes were prepared by gluing a glass bead to the end of Tap 300 tapping AFM probes ( $k=29-46$  N/m) or contact AFM probes ( $k=0.1-0.3$  N/m) (Budget Sensors) depending on the expected magnitude of adhesion force to be

measured. The glue used here is a UV curing adhesive (loctite™ 350) and the glass beads were dry borosilicate glass microspheres ( $d=20\ \mu\text{m}$ ) (Duke Scientific Corporation, CA). The glass beads were first washed by solvents (DI water, Acetone) and then cleaned by UV tips cleaner. Before gluing the glass beads, the spring constant of the cantilevers were measured using the Sader's method [5].

The method to glue the glass beads to AFM probes employed the optical view and manual movement functions in the AFM system: First a small droplet of glue was placed on one side of AFM sample holder and a small group of glass beads on the other side. A sacrificial AFM probe was positioned over the glue droplet with the help of the optical microscope and manual position controller in the AFM. The probe was approached down into the glue slightly to let the tip dip into a small amount of glue to then draw out a thin line of glue. A fresh tip was then dipped into this line of glue and approached to one of the glass beads. The glue on the end of probe then affixed a glass bead.

Before the force measurements, as for normal AFM force measurements, the geometry of colloid AFM probes needed to be determined for subsequent surface free energy calculations and also to check for any contaminations on the contact area of glass beads. Because the average diameter of glass bead is about  $20\ \mu\text{m}$ , and the period of calibrating grating (TGT1) is only  $3\ \mu\text{m}$ , the

completed images of colloid probes can not be obtained with the AFM reverse imaging method [6]. Only the very end of glass beads (the contact area with spikes on the grating) can be imaged. However, for most cases these images provided enough information on the contact area between the colloid probes and the sample surfaces, because the contact areas are limited to within hundreds of nanometers for the colloid probe force measurements. It is very difficult for such large probes to penetrate deep into the sample surface with the relative small applied loading forces used (around several hundreds nNs). So the reverse images from calibrating grating can be used to derive the contact area geometry for the surface energy calculation. Scanning Electron Microscope (SEM) was also employed in to image the colloid probes. SEM provides the image of whole colloid probe but with a resolution relatively lower than the AFM reverse images. Another issue is that the glass beads are not conductive, so the colloid probes need be coated with Au before the SEM measurements. But the colloid probes with Au coating are not useful for the adhesion forces measurements any more. So the SEM images were taken after the adhesion forces measurements and any contaminations before force measurements can not be observed with SEM.

The colloid probes were modified with two kinds of plasma polymers: Hexane and Allylamine. The polymers were coated on colloid probes using a plasma polymerize coating method (Figure 4.1). This coating employs a RF generator

to create the low temperature plasma at low pressure. The colloid probes were placed on the sample tray. Before opening the monomer valves, oxygen gas was pumped into the coating chamber for 3 minutes to clean the chamber by oxidation of any organic contaminations. The pressure was kept at 300 millitorr and the RF was adjusted to an incident value of 20 and a reflected index below 1. The flow rate of monomers was set at 1.6-1.7 Å/Sec. Stopped the coating process, when the indicator of quartz crystal showed the thickness of polymer had reached to 20 nm. Together with colloid probes, two cleaned glass slides and four cleaned normal AFM probes (FESP) were also placed in the sample tray for the control measurements and further thickness measurements.

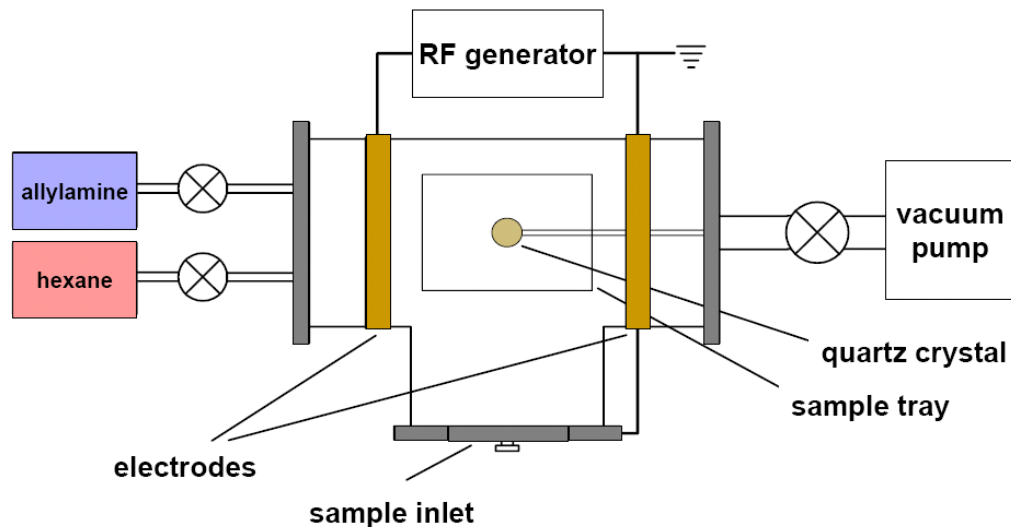


**Figure 4.1** A schematic illustration of the plasma coating machine used to functionalize the AFM colloidal probes.

The AFM force measurements with colloid probes were recorded in the same fashion as with normal AFM probes. The Environ-Scope AFM (Veeco) was used at a relative humidity below 2 %. For the plasma polymer coated probes,

the number of measurements with a single probe was limited to 5 times, as the polymer coatings are relative fragile. The surface free energy values of coated plasma polymers were measured by the contact angle method on the control coated glass slides. Two liquids: water and diiodomethane were used in the contact angle measurements and the Wu's method was used to derive surface free energy from the contact angle results [7].

The thickness of coated polymer was measured by an AFM imaging method. Firstly, a normal AFM tapping probe was used to fast scan over a  $1 \times 1 \mu\text{m}^2$  area in contact mode with a high loading force ( $\sim 500 \text{ nN}$ ). The polymers were scraped off by such a high force. Then the tapping images of larger area ( $10 \times 10 \mu\text{m}^2$ ) were taken using a new tapping AFM probe. The thickness parameters of two coated polymers were analyzed by image analysis using SPIP software (Image Metrology, Denmark).

## **4.3 Results and Discussions**

### **4.3.1 SEM and AFM Reverse Images of Colloid Probes**

The SEM images which were taken before the force measurements without Au coating for the normal colloid probes (Figure 4.2) were used to obtain the general information on the glass beads. Because the glass beads are not conductive, to avoid the damage to the glass beads, low voltages and small spot

sizes were used. This has led to the reduced resolution of the images. The plasma polymer coated colloid probes were imaged after the force measurements and coated with Au. So the resolutions of these images (Figure 4.3) are relatively higher.

The image analysis software ImageJ (v 1.41, NIH, US) was used in the glass beads size determination. After calibrating the scale of images (pixels/unit), the boundary of the glass beads was located by user and the software provides the diameter values of glass beads from figure 4.2 and 4.3.

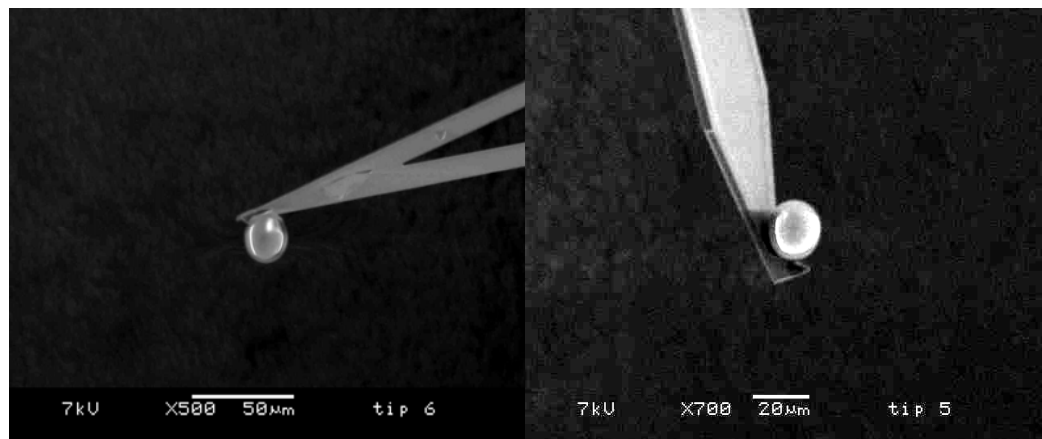


**Figure 4.2** SEM images of colloid probes without Au coating: (a) a contact mode AFM probe with a glass bead glue on the end of cantilever ( $R=9.5 \mu\text{m}$ ). (b) a tapping mode AFM probe with a glass bead glue on the end of cantilever ( $R=9.7 \mu\text{m}$ ).

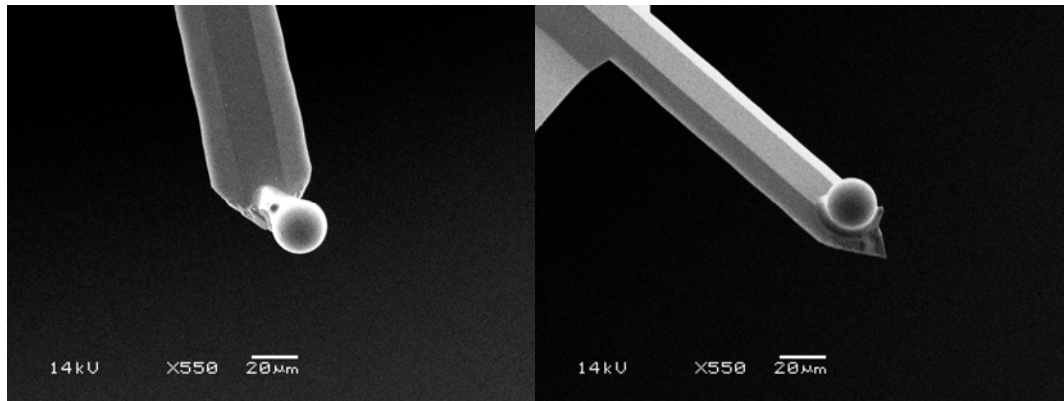


**Figure 4.3** SEM images of colloid probes: (a) a tapping mode AFM probe with a glass bead glue on the end of cantilever ( $R=10.1 \mu\text{m}$ ). (b) a tapping mode AFM probe with a glass bead glue on the end of cantilever ( $R=9.6 \mu\text{m}$ ).

The AFM reverse image method provides detailed information on colloid probes contact region. For the uncoated glass bead probes, before and after the forces measurements, the topography images from AFM reverse imaging method show no significant differences. However, for the polymer coated glass bead probes, because the polymer films are relatively fragile, it is very possible to break the coating in the reverse imaging process with the sharp grating spikes, so the reverse images of polymer coated colloid probes were taken after force measurements only. From the AFM images, it is noticed that, at the submicron scale the surfaces of glass beads are not homogeneous or smooth as expected: some small asperities can be observed. Such asperities will change the contact geometry: the radius of probe will change from the radius of the glass bead to the radius of one small asperity, assuming that these asperities do not collapse or deform under the loads applied. For every colloid probe used in

adhesion forces measurements, the reverse images need to be obtained to check the topography of the glass bead. In some cases, the radii of small asperities on the glass beads were applied in the following surface free energy calculation.

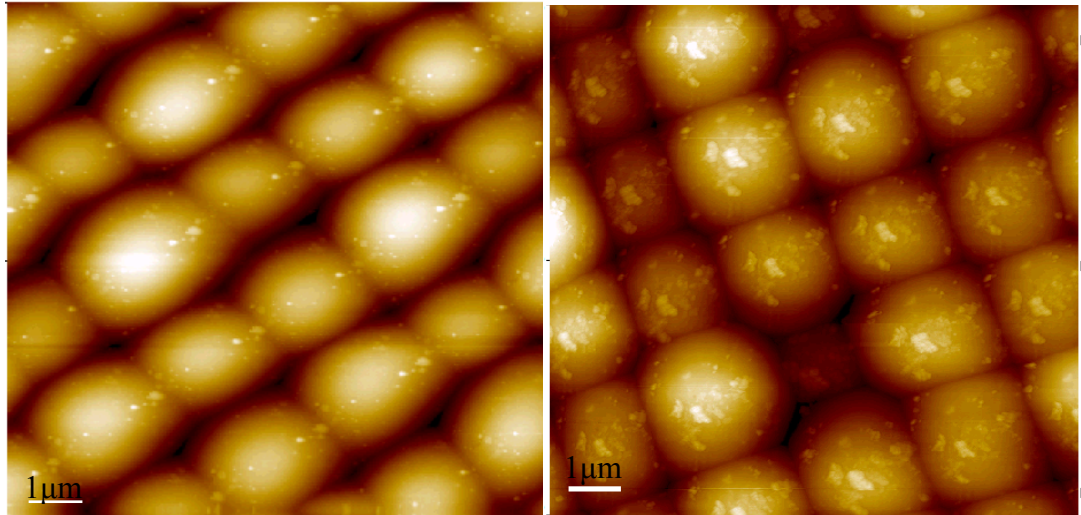


**Figure 4.4** AFM reverse image method on colloid probes. AFM height images of an uncoated colloid probe after several forces measurements (Left) and a plasma polymer hexane coated colloid probe after several forces measurements (Right).

#### **4.3.2 Uncoated Colloid Probes Adhesion Forces Measurements and Surface Energy Calculation**

The adhesion forces obtained with uncoated glass bead colloid probes and the surface energy calculation results are listed in table 4.1. The dispersion surface free energy value for uncoated glass bead is  $24 \text{ mJ/m}^2$  [8]. The radii for glass beads are all in the range of  $10 \text{ }\mu\text{m}$  from the SEM images analysis. But from the AFM reverse image method, all five probes have unique radii due to the heterogeneous structures on glass beads surfaces. So the radius of contact is taken as the value calculated from the small asperity on glass bead from

reverse imaging method and not the global radius of glass bead from SEM images. The roughness of sample surface will affect the contact area of colloid probes more than normal AFM probes, because for colloid probes with larger radii there are more chances to contact with a number of small asperities on the sample surface [9]. The roughness values can be found in table 3.1. Generally, PVP and DCPD have higher RMS values, while lactose monohydrate and the two APIs have lower roughness values.

**Table 4.1** Adhesion Forces and Surface Energy Results from Uncoated Glass

Beads Probes		(N=50)		
Samples	Adhesion Forces (nN)	Radius of Probe (nm)	Surface (mJ/m <sup>2</sup> )	Energy
AZD 3409 HCL salt	531.8 (120.5)	1608	17.8 (0.8)	
AZD 3409 Malate salt	151.3 (40.4)	313	13.8 (0.9)	
Lactose monohydrate	844.6 (235.4)	2548	24.0 (1.9)	
HPMC	334.5 (115.1)	1108	19.9 (2.4)	
DCPD	41.3 (41.4)	499	1.5 (1.5)	
PVP	153.2 (120.0)	980	5.3 (3.3)	

The range of adhesion forces observed for the colloidal probes are larger than would be expected for normal AFM probes, again presumably due to the variations in the number of asperities involved. In addition, these deviations in adhesion are less likely to represent the surface free energy differences between different crystal faces (or layers) as for nanoscale normal AFM probes.

The surface energy values (Table 4.1) derived from colloid probe force measurements are smaller than those from the AFM probe measurements. In the surface energy calculation, the radius used could be overestimated leading to a reduction of apparent surface energy. In general the larger the sample roughness, the smaller the derived surface energy will tend to be. For those rougher samples like DCPD and PVP (Table 3.1 and Table 4.7), the standard deviations are as large as mean average values, and the derived surface energies are much smaller than the values derived from the normal AFM probes.

In table 4.1, the surface free energy for AZD 3409 HCl salt is larger than the malate salt. In Chapter 3, the normal AFM probe adhesion forces measurements and contact angle measurements (Table 3.3 and Table 3.6), both showed that the AZD 3409 malate salt had a larger surface free energy values than the HCl salt. One possible reason for this difference could be that the roughness of malate salt disc is higher than the HCl salt. It is also possible that polar interactions and not just dispersion interactions have occurred between the glass beads and sample surfaces. The glass beads are mainly made of silica but also have composition of boron oxide, sodium oxide, potassium oxide and calcium oxide [10]. So it is possible that the polar interactions occur between the samples surfaces and the glass beads [11]. So in this work, the derived surface energy values are only presenting the relative strength of interfacial

forces between the glass beads and the samples surfaces. They can not be compared with the surface free energy values derived from the contact angle measurements and the dispersion surface free energy values derived from normal AFM probe adhesion forces measurements.

#### 4.3.3 Plasma Polymer Coated Glass Beads Colloid Probes Adhesion Forces Measurements and Surface Free Energy Calculations

To derive the surface free energies of the samples under study, the surface free energy of coated plasma polymer hexane and allylamine should be determined. The contact angle values of two liquid probes were measured on the coated control glass slides. These slides were coated together with the colloid probes in the plasma coater so that the thickness and the degradation status of polymer should be at the same level with the coated colloid probes. The results of contact angle and surface free energy derived from Wu's method are presented in table 4.2.

**Table 4.2** Contact Angle and Surface Free Energy Results of Plasma Polymer Hexane and Allylamine

Polymer	Water Contact Angle (°)	Diiodomethane Contact Angle (°)	Dispersion Free Energy (mJ/m <sup>2</sup> )	Surface Polar Surface Free Energy (mJ/m <sup>2</sup> )
Hexane	104.3 (1.5)	49.3 (1.7)	34.7 (0.9)	0
Allylamine	65.5 (2.0)	39.5 (0.4)	39.9 (0.2)	11.3 (1.1)

It is obvious that plasma polymerized hexane has only a significant dispersion part of its surface free energy. This property means that the hexane coated colloid probes could only interact with the dispersion surface free energy component of sample surface. So the hexane modified colloid probes can help investigate more details in the solid-solid interfacial energy. In comparison the results from the allylamine modified colloid probes, show that the quantities of dispersion and polar contributions can be determined.

The thickness of coated polymer on the glass bead was determined by an AFM imaging method, whereby the polymer film was first removed from a small region using a high imaging force. The average lines sections of images (Figure 4.5, Figure 4.6) were used to calculate the polymer thickness on the coated glass slides. The thickness of plasma polymer hexane is 8.1 nm, and plasma polymer allylamine is 12.7 nm. Although the coating parameters set for the two monomers were the same, the differences in monomer molar mass (hexane:  $86 \text{ g/mol}^{-1}$  and allylamine:  $57 \text{ g/mol}^{-1}$ ) and molecular structure of two materials made the coating thickness slightly different.

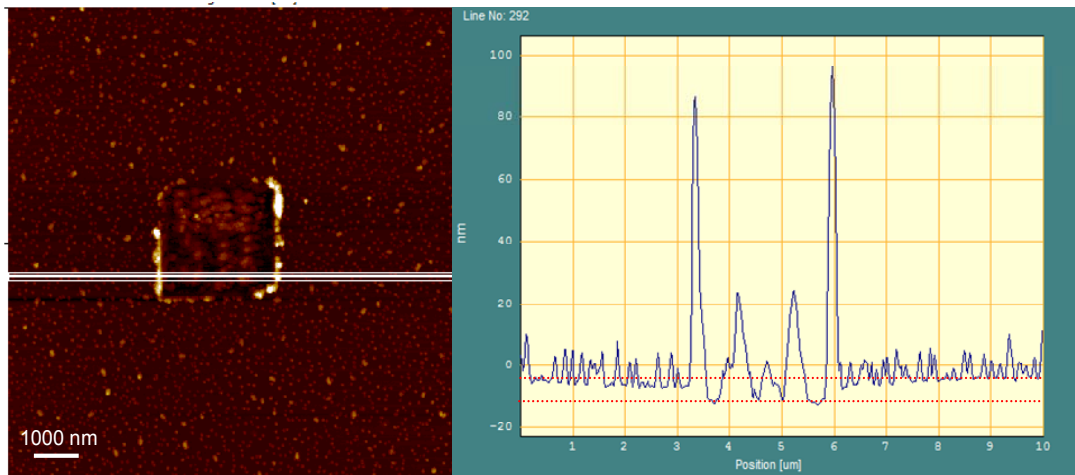


**Figure 4.5** Tapping images of thickness measurement with AFM scratching method on plasma polymer hexane (Left) and average lines profiles function in SPIP (Right).

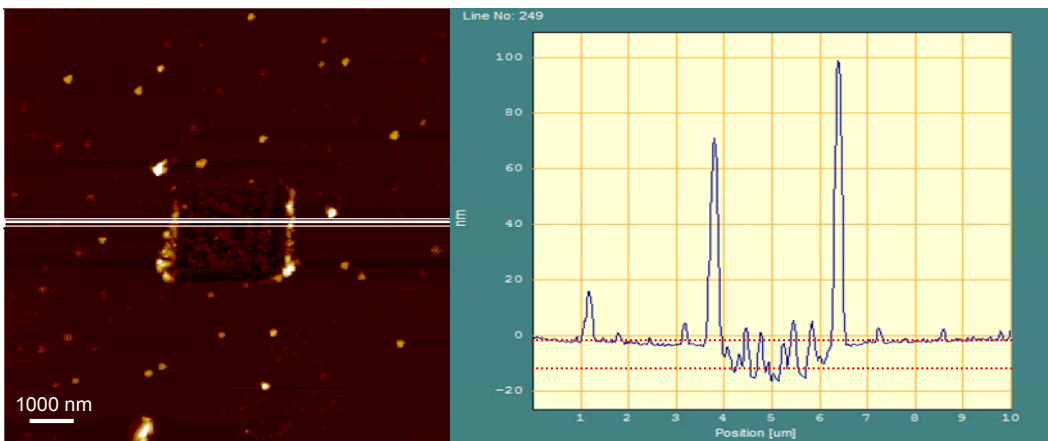


**Figure 4.6** Tapping images of thickness measurement with AFM scratching method on plasma polymer allylamine (Left) and average lines profiles function in SPIP (Right).

The topographies of colloid probes have changed from the glass surfaces to smoother plasma polymer surfaces once the coating processes had been done. So the roughness of plasma polymer hexane and allylamine directly determine the roughness of colloid probes. However, the macroscopic shape of the colloid probes was not significantly changed during polymer coated [12]. So the

contact radii of colloid probes were still derived from the AFM reverse images. The roughness parameter (RMS) were measured at  $5 \times 5 \mu\text{m}^2$  scan size (Figure 4.7) and generated by SPIP. The results are listed in table 4.3.

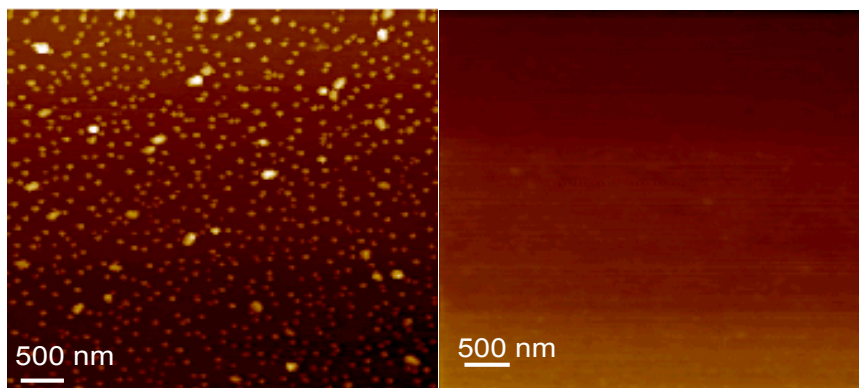


**Figure 4.7** Tapping topography images of plasma polymer hexane on glass slide (left)  $5 \times 5 \mu\text{m}^2$ , plasma polymer allylamine on glass slide (right)  $5 \times 5 \mu\text{m}^2$ .

**Table 4.3** RMS roughness results of plasma polymer hexane and allylamine

Polymer	RMS $5 \times 5 \mu\text{m}^2$ (nm)
Plasma Polymer Hexane	8.8
Plasma Polymer Allylamine	4.3

The adhesion force measurements with the coated colloid probes are presented in table 4.4 and 4.5. The force measurements were carried out with a Nanoscope IV controller (Veeco). The total measured times for each sample were limited to 9 measurements in  $3 \times 3 \mu\text{m}^2$  area. For the coated FESP probes, as control measurements, two APIs, lactose and silicon samples were measured.

**Table 4.4** Adhesion forces (AD) measurements on samples with plasma  
polymer hexane coated probes Unit: nN (N=9)

Sample	Probe 1 AD	Probe 2 AD	Probe 3 AD	FESP probe AD
AZD 3409 HCl salt	1152.5 (353.8)	951.1 (219.8)	516.9 (52.4)	25.9 (2.4)
AZD 3409 Malate salt	446.7 (95.5)	120.5 (21.1)	155.6 (22.0)	21.1 (2.0)
Lactose monohydrate	405.2 (54.1)	198.5 (20.9)	212.8 (80.2)	22.3 (3.2)
Silicon	1514.7 (101.0)	1110.7 (80.6)	1507.1 (41.4)	14.8 (1.1)
DCPD	48.3 (6.3)	172.0 (28.4)	78.2 (16.2)	
MCC	438.6 (182.6)	293.8 (47.2)	313.0 (50.7)	
Magnesium Stearate	564.1 (108.0)	278.5 (47.4)	353.0 (76.9)	
HPMC	568.3 (55.6)	240.3 (44.5)	623.5 (90.7)	

**Table 4.5** Adhesion forces (AD) measurements on samples with plasma  
polymer allylamine coated probes Unit: nN (N=9)

Sample	Probe 1 AD	Probe 2 AD	Probe 3 AD	FESP probe AD
AZD 3409 HCl salt	600.7 (80.3)	296.8 (60.5)	1092.9 (131.5)	52.6 (21.9)
AZD 3409 Malate salt	75.5 (24.4)	115.3 (28.8)	1103.8 (285.7)	38.0 (8.7)
Lactose monohydrate	221.8 (81.3)	148.6 (19.4)	177.7 (36.1)	44.5 (11.3)
Silicon	1246.8 (66.7)	1230.2 (40.1)	1938.1 (77.7)	24.3 (3.0)
DCPD	55.2 (24.6)	121.0 (33.6)	242.2 (90.9)	
MCC	193.6 (112.9)	145.8 (67.2)	43.4 (11.7)	
Magnesium Stearate	645.0 (66.6)	207.8 (28.5)	489.4 (128.5)	
HPMC	204.1 (29.3)	88.9 (11.7)	225.6 (27.5)	

The adhesion forces from different probes should not be compared directly, because the radius of each glass bead is not identical in the size or roughness.

However, the adhesions are comparable for the same probe as the contact radius should be consistent for each sample with the same probe. The adhesion force for each sample with the same probe is compared to index the relative magnitude of interfacial surface energy, if the surface roughness is temporarily ignored.

In Figure 4.8 and 4.9, the same trends can be found with each probe. The silicon has the highest adhesion forces not only with the hexane coated probes but also with the allylamine probes. The relative strength of adhesion forces for those samples ranks in such an order: Silicon > API HCl salt > Magnesium Stearate > MCC > HPMC > lactose monohydrate > API malate salt > DCPD with the hexane coated probes. With the allylamine probes the order is Silicon > API HCl salt > Magnesium Stearate > lactose monohydrate > HPMC > MCC > API malate salt > DCPD. The rank in surface free energy calculation shall stand in such order as well.

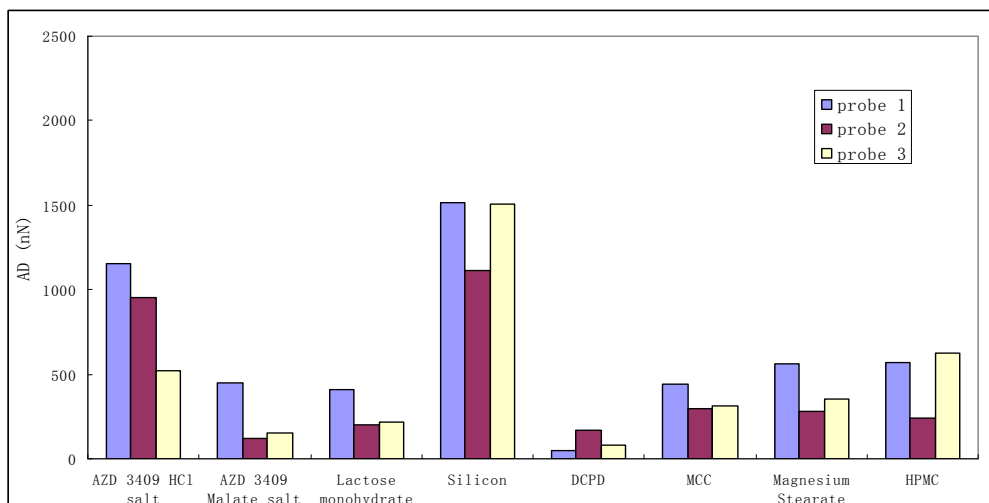


**Figure 4.8** Graphic illustration of the relative magnitude of adhesion forces (AD) for each sample obtained from plasma polymer hexane colloid probes force measurements.

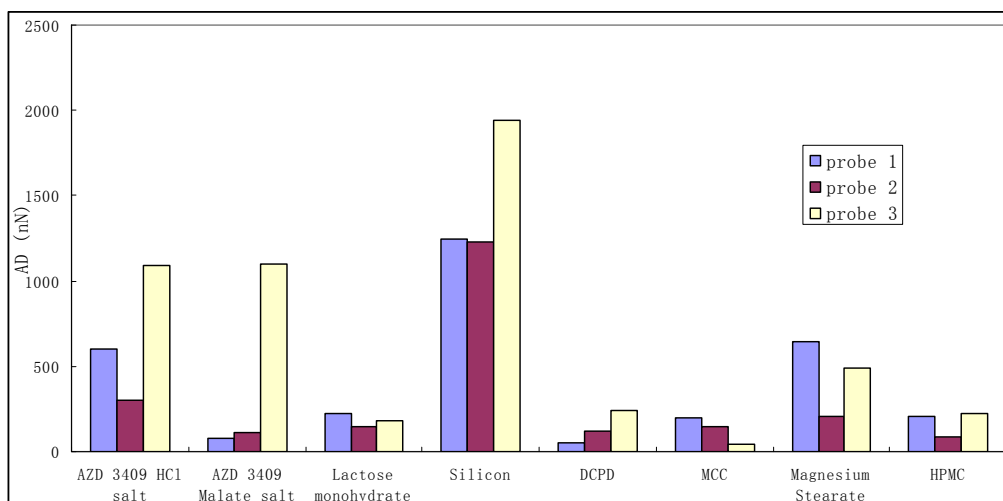


**Figure 4.9** Graphic illustration of the relative magnitude of adhesion forces (AD) for each sample obtained from plasma polymer allylamine colloid probes force measurements.

The radius of each coated probe was obtained from the AFM reverse images and the surface free energy calculations followed the same data analysis method described in Chapter 3. The results of hexane coated colloid probes and FESP probes are listed in Table 4.6.

**Table 4.6** Surface free energy values of samples derived from hexane coated colloid probes and FESP probes Unit: mJ/m<sup>2</sup>

Sample	Surface free energy values from hexane coated colloid probes	Surface free energy values from hexane coated FESP probe (n=1)
AZD 3409 HCl salt	16.7 (10.1)	13.9
AZD 3409 Malate salt	1.3 (1.6)	16.1
Lactose monohydrate	1.5 (1.0)	38.3
Silicon	37.6 (5.9)	31.2
DCPD	0.3 (0.4)	
MCC	2.4 (0.6)	
Magnesium Stearate	3.2 (1.6)	
HPMC	4.7 (3.0)	

It is not a surprise to find that in the hexane coated colloid probes force measurements the surface free energy values are much smaller than the bare AFM probe measurements. Because the contact radii of coated colloid probes are larger, which make the contact areas are much larger than them in the bare AFM probes measurements. The chances of small asperities contact due to the samples or probes roughness in the larger contact areas become higher in this case. The roughness of samples and colloid probes will decrease the actual contact areas leading to the derived surface free energy values smaller than those derived from the bare AFM probes. In the controlled coated FESP probe, the derived surface free energy values are not much different from the AFM probe values in Chapter 3. Still the higher the roughness of the sample (Table

4.7), the smaller the derived surface free energy is when compared with the results in Chapter 3. For example, the RMS roughness of DCPD disc is 101 nm in a  $10 \mu\text{m}^2$  scan size and the derived surface free energy in the coated colloid probes measurements is only  $0.3 \text{ mJ/m}^2$ . While in Chapter 3, the derived surface free energy of DCPD is  $27.1 \text{ mJ/m}^2$ . Because hexane only has the dispersion component of surface free energy, the adhesions obtained from AFM force measurements should be only contributed by the dispersion interactions and the surface free energy values derived from hexane coated colloid probes will be the dispersion surface free energies.

**Table 4.7** Roughness (RMS) values of samples for colloid probe forces measurements Unit: nm

Samples	RMS at $2 \times 2 \mu\text{m}^2$	RMS at $5 \times 5 \mu\text{m}^2$	RMS at $10 \times 10 \mu\text{m}^2$
AZD 3409 HCL salt	9.46	16.8	29.3
AZD 3409 Malate salt	12.9	21.3	36.2
Lactose monohydate	9.8	12.6	18.5
DCPD	30.4	39.4	101
MCC	5.6	19.1	64.3
Magnesium Stearate	13.0	19.0	24.7

The sample surface energy calculation for allylamine coated colloid probe is more complicated. The plasma polymer allylamine has both dispersion and polar surface free energy. The equation 3.2 and 3.3 may hence not be valid for allylamine coated colloid probes. Whereas the dispersion surface free energy

derived from hexane coated colloid probes and radii of allylamine coated colloid probes, the two parameters are available to derive theoretic adhesion forces contributed by dispersion surface free energy (Table 4.8). Comparing the theoretic adhesion forces (dispersion forces) contributed by the dispersion interactions with actual adhesion forces from experiments, the polar surface free energy contributions (attractive or repulsive) can be revealed (Figure 4.10, 4.11). If the calculated dispersion forces are lower than the experimental adhesion forces, the polar interactions should act as the attractive forces and the strength of the polar interactions could be regarded as the difference between the dispersion force and experimental adhesion force. If the calculated dispersion forces are higher than the experimental adhesion forces, the polar interactions may be repulsive. And if these two forces are similar, the polar interactions on those samples surfaces may be negligible.

**Table 4.8** Theoretic adhesion forces calculated with dispersion surface free energy derived from hexane coated colloid probes and radii of allylamine coated colloid probes and FESP probes from reverse images. Unit: nN

Sample	Probe 1 AD	Probe 2 AD	Probe 3 AD	FESP probe AD
AZD 3409 HCl salt	870.0	832.8	1302.4	33.3
AZD 3409 Malate salt	242.7	232.4	363.4	40.6
Lactose monohydrate	260.7	249.6	390.3	51.6
Silicon	1305.5	1249.7	1954.2	26.6
DCPD	116.6	111.6	174.6	
MCC	329.8	315.7	493.7	
Magnesium Stearate	380.8	364.6	570.1	
HPMC	461.6	441.8	690.9	

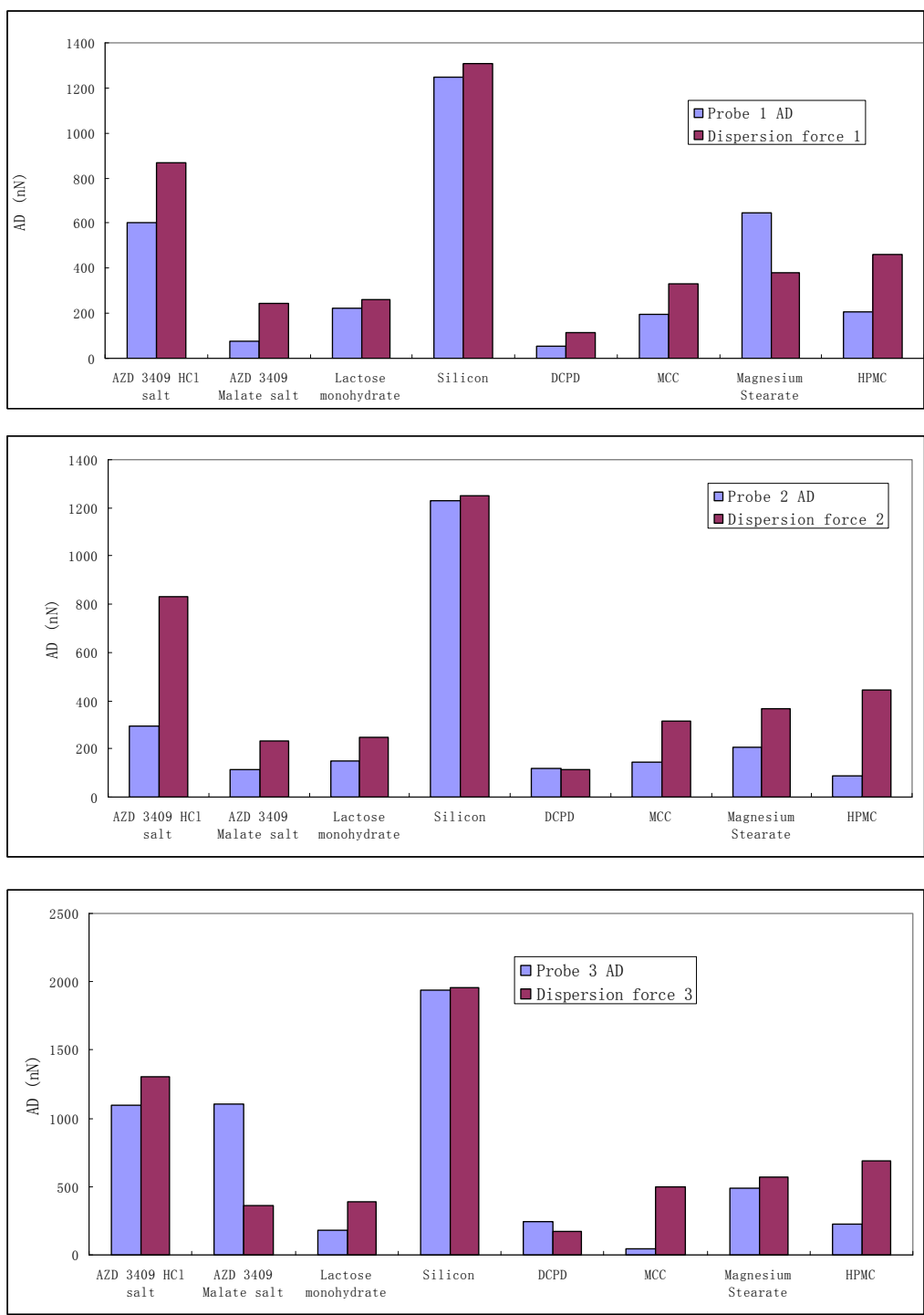


**Figure 4.10** Comparison plots of dispersion forces which are derived from dispersion surface free energy and radius of each colloid probe and adhesion forces (dash dot line) which are obtained from colloid probe adhesion force measurements.

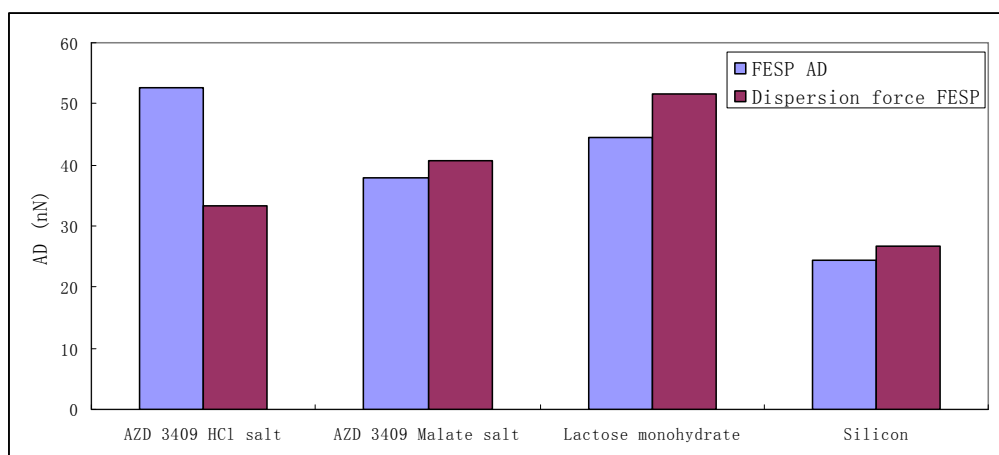


**Figure 4.11** FESP probes comparison plots of dispersion forces which are derived from dispersion surface free energy and radius of each colloid probe and adhesion forces (dash dot line) which are obtained from colloid probe adhesion force measurements.

From the data in table 4.8 and comparison plots of Figure 4.10 and Figure 4.11, it is clear that, with allylamine coated colloid probes, the experimental adhesion forces for most samples are much smaller than the theoretical dispersion adhesion forces. Although it is not easy to assess the polar surface free energy values from AFM force measurements, the possible contributions of polar surface energy in adhesion forces could be estimated. In those cases which the experimental adhesion forces are smaller than the theoretical dispersion adhesion forces, the polar surface free energies of those samples (HCl salt, lactose monohydrate, MCC, HPMC) must have decreased the adhesion forces and acted as repulsive forces [13]. It is also found that for the Silicon wafer that the experimental adhesion forces are almost consistent with the theoretical dispersion forces. This indicates that the polar interactions on

the cleaned Si surface are much smaller than its dispersion interactions. The differences in the magnitude between the experimental adhesion forces and the theoretical dispersion forces seem partly related to the magnitude of the polar surface free energies. For lactose monohydrate, MCC and HPMC which have similar polar surface free energy (12.0, 12.2 and 10.1 mJ/m<sup>2</sup>), the differences between experimental and theoretical dispersion adhesion forces are similar as well. One exception is DCPD which has the highest polar component surface free energy values as derived from contact angle measurements (32.6 mJ/m<sup>2</sup>): The differences are even smaller than lactose monohydrate, MCC and HPMC with smaller polar surface free energies. It is possible that the high polar surface free energy or particular interaction has increased the experimental adhesion force for DCPD and decreased it for other samples. Unlike the dispersion interactions, depending on the nature of polar interactions, the polar interactions can behave either repulsively or attractively [14]. So for DCPD, its polar interactions may act as attractive forces. Alternatively the high RMS roughness value of DCPD leads to this unusual case.

These results could not only be applied in colloid probes force measurements, but also could explain the differences existing in table 3.8 of Chapter 3 when we compared the surface free energies derived from AFM probe force measurements with those from the contact angle method. If the polar components of surface free energies have decreased the overall adhesion forces

between probes and sample surfaces by acting as a source of repulsive forces, the dispersion surface free energies derived from AFM adhesion forces should be smaller than those from contact angle measurements. From table 4.8 it is found that the polar component of surface free energy for Si is much smaller than its dispersion component, so the Si AFM probes should have limited polar interactions with those samples as well. In Figure 4.11, it is also found that with the FESP coated probes in control experiments the differences between the experimental adhesion forces and theoretical dispersion forces are not as large as them with the colloid probes. These magnitude differences may also rise from the differences in the scales of measurements between the FESP and colloid probes. Generally, the polar interactions may exist in the interface of a Si probe and some sample but should not be very strong. Other factors such as contact geometry, surface roughness, relative humidity, electrostatic forces or electrosteric mechanism [15] could also play a part in the differences of AFM adhesion forces surface free energy measurements.

#### **4.4 General Conclusions**

Colloid probes which are made of glass beads have been used to derive the surface free energy values from AFM adhesion forces measurements. The results are much smaller than those derived from AFM probe forces measurements. The large size of the contact area of the colloidal probe and the

complex contact geometry could be the reasons to explain the data differences between colloid probes and AFM probes. The polar interactions between glass bead surface and sample surface may also be involved in the adhesion force measurements where dispersion forces are considered as the only source of the adhesions in the bare AFM probe force measurements.

To further understand the roles of dispersion and polar component surface free energy play in the AFM adhesion force measurements, the colloid probes have been modified with plasma polymerized hexane and allylamine. The RMS roughness values of both coated probes and sample surface are determined, and surface free energy values of coated polymers are measured by contact angle. The hexane coated colloid probes have only a dispersion component of surface free energy. So the interactions between the hexane coated probes and sample surfaces could only be the dispersion interactions. The dispersion surface free energies derived from force measurements with hexane coated probes and radii of colloid probes are applied to calculate the theoretical dispersion forces between allylamine coated probes and sample surfaces. The allylamine coated probes have both dispersion and polar component of surface free energy. It is difficult to directly determine the quantity of polar interactions from overall adhesion forces of allylamine coated probes. However, the comparison could reveal the possible direction of polar interactions which for most cases is opposite to the dispersion interactions which are always attractive.

This could also be used to explain the data differences between surface free energy results from AFM adhesion force measurements with bare AFM probes and contact angle measurements.

## References

1. F. Podczeck, J. M. Newton and M. B. James. Variations in the adhesion force between a drug and carrier particles as a result of changes in the relative humidity of the air. *Int. J. Pharm.* **149** (1997) 151.
2. M. Farshchi-Tabrizi, M. Kappl, Y. J. Cheng, J. Gutmann and H. Butt. On the adhesion between fine particles and nanocontacts: an atomic force microscope study. *Langmuir* **22** (2006) 2171.
3. D. Traini, P. Rogueda, P. Yong and R. Price. Surface energy and interparticle force correlation in model pMDI formulations. *Pharm. Res.* **22** (2005) 816.
4. P. G. A. Rogueda. HPTP, a model propellant for pMDIs. *Drug Dev. Ind. Pharm.* **29** (2003) 39.
5. J. E. Sader, J. W. M. Chon, and P. Mulvaney, Calibration of rectangular atomic force microscope cantilevers, *Rev. Sci. Instrum.* **70** (1999) 3967.
6. G. W. Bao and S. F. Y. Li. Characterization of atomic force microscopy (AFM) tip shapes by scanning hydrothermally deposited ZnO thin films. *Talanta* **45** (1998) 751.
7. S. Wu. Polar and nonpolar interactions in adhesion. *J. Adhes.* **5** (1973) 39.
8. M. C. Gutiérrez, S. Osuna and I. Baráibar. Solid surface mapping by inverse gas chromatography. *J. Chromatogr. A* **1087** (2005) 142.
9. J. C. Hooton, C. S. German, M. C. Davies and C. J. Roberts. A Comparison of morphology and surface energy characteristics of sulfathiazole polymorphs based upon single particle studies. *Eur. J. Pharm. Sci.* **28** (2006) 315.

10. W. Vogel. Glass Chemistry 2<sup>nd</sup> edition. Springer-Verlag, Berlin, (1994).
11. M. Murayama, K. Fujibayashi, M. Matsui and N. Murasaki. Electrostatic launching of vibrating glass beads. *J. Electrostatics*. **42** (1997) 143.
12. W. Magalhães and M. de Souza. Solid softwood coated with plasma-polymer for water repellence. *Surf. Coat. Technol.* **155** (2002) 11.
13. O. Planinsek, R. Pisek, A. Trojak, S. Srcic. The utilization of surface free energy parameters for the selection of a suitable binder in fluidized bed granulation. *Int. J. Pharm.* **207** (2000) 77.
14. D. Wiegel, J. Kaufmann and K. Arnold. Polar interactions of chondroitinsulfate: surface free energy and molecular dynamics simulations. *Colloids Surf. , B* **13** (1999) 143.
15. N. Marilyn Ahfat, Graham Buckton, Robert Burrows, Martyn D. Ticehurst. Predicting mixing performance using surface energy measurements. *Int. J. Pharm.* **156** (1997) 89.

## **Chapter 5: Nanoscale Mechanical (Young's modulus) and Thermal Properties Characterization of Formulation Components**

### **5.1 Introduction**

In this Chapter, the fundamental characterizations of some materials used in tablet formulations are described. The mechanical (Young's modulus) properties will be measured using an AFM with the nanometer spatial resolution. The changes of mechanical properties with temperatures will be studied with an AFM hot-stage set-up. The thermal (melting point and glass transition temperature) properties will be measured using a scanning thermal microscopy and a nano-TA system. In addition the dehydration and rehydration of lactose monohydrate will be studied by the nano-TA system with the nanometer resolution. These studies will exemplify the potential of these approaches before their applications on the mixtures of materials used within the tablet formulations studied in this thesis.

### **5.2 Materials and Methods**

The materials for Young's modulus measurements were AZD 3409 HCl salt and malate salt, lactose monohydrate, Avicel, polyvinyl pyrrolidone (PVP), magnesium stearate and crospovidone (Macclesfield, AstraZeneca). These

samples are slightly compressed with two clean glass slides by hand and transferred to the AFM sample holders. Dibasic Calcium Phosphate Dihydrate (DCPD), Anhydrous Calcium Phosphate (ACP) and Hydroxypropyl Methyl Cellulose (HPMC) (Macclesfield, AstraZeneca) were similarly treated like other samples for temperature dependency studies with the AFM hot-stage accessory. The FESP probes (Veeco) used in the Young's modulus measurements were cleaned with an UV tip cleaner (BioForce, USA).

The materials for thermal properties measurements were AZD 3409 HCl salt and malate salt, lactose monohydrate and HPMC (Macclesfield, AstraZeneca). The samples were generally compressed with two cleaned glass slides by hand to create flat surfaces. The large single lactose crystals were prepared by anti-solvent recrystallization which placed the lactose water solution in ethanol (70%) environment overnight. The calibration processes of SThM (Veeco) was carried out by measuring the melting point temperatures of crystalline biphenyl (69 °C), benzyl (95 °C) and benzoic acid (122 °C). The calibration of the nano-TA system (Anasys Instruments, UK) involved measuring the melting point temperatures of Polycaprolactone (PCL) (56 °C), Polyethylene (PE) (116 °C) and Polyethylene terephthalate (PET) (238°C). The Aluminum pans for differential scanning calorimeters DSC 2920 (TA Instruments, CA, USA) measurements were purchased from Agar. The SEM images were taken with a JSM-6060LV Scanning Electron Microscope (JEOL, Tokyo, Japan).

The mechanical properties measurements employed a Multimode AFM and a hot-stage accessory (Veeco). The Force-Distance curves of samples were recorded using FESP probes to enable the mechanical (Young's modulus) property determination. The force measurement processes were as the same as those in the AFM surface free energy measurements. The indentations ( $\delta$ ) of FESP probes into the sample surfaces were derived by comparison with the gradients of contact regions between hard silicon wafers and samples. The radii ( $R$ ) of probes were determined by analyses of the FESP probes reverse images and sample indentations. In the mechanical measurements, the functions of the loading forces ( $L$ ) with indentations are needed to calculate the combined elastic modulus ( $K$ ) in the model of sphere-plane [1]:

$$K = \frac{L}{(8\delta^3 R)^{\frac{1}{2}}} \quad \text{Equation 5.1}$$

The elastic moduli of probe and sample ( $E_t$  &  $E_s$ ) can be solved with the Poissons' ratio of probes and samples ( $\nu_t$  &  $\nu_s$ ) in Equation 5.2

$$K = \frac{4}{3} \left( \frac{1-\nu_t^2}{E_t} + \frac{1-\nu_s^2}{E_s} \right)^{-1} \quad \text{Equation 5.2}$$

In the AFM mechanical measurements, the FESP probes have much larger Young's modulus than the pharmaceutical materials. So the first bracketed term in Equation 5.2 is smaller than the second and close to zero, leading to equation 5.3 [2].

$$E_s = \frac{3K(1-\nu_s^2)}{4} \quad \text{Equation 5.3}$$

Combining equations 5.1 and 5.3:

$$E_s = \frac{3L(1-\nu_s^2)}{4(8\delta^3 R)^{\frac{1}{2}}} \quad \text{Equation 5.4}$$

The changes of Young's modulus with temperature were measured with a multimode AFM and a hot-stage accessory. For HPMC the temperatures were set at room temperature (27 °C), 40 °C, 60 °C, 80 °C, 100 °C, 120 °C and 140°C. After heating and on return to room temperature, the Young's modulus of HPMC was also measured to compare with the original value. For DCPD, the dehydrate temperature of DCPD crystal is expected at 105 °C [3]. So the DCPD samples were heated to 109 °C with the hot-stage for 30 minutes. The Young's moduli of samples before and after the heating were measured and compared.

The melting points of the materials were measured with the SThM attachment on an Explorer AFM (Veeco) utilizing Wollaston wire thermal probes (Figure 5.1). The microfabricated probes (AN-2, Anasys Instruments) (Figure 5.2) used for the nano-TA system have a smaller tip radii and hence higher spatial resolution than the SThM probes but are more fragile.

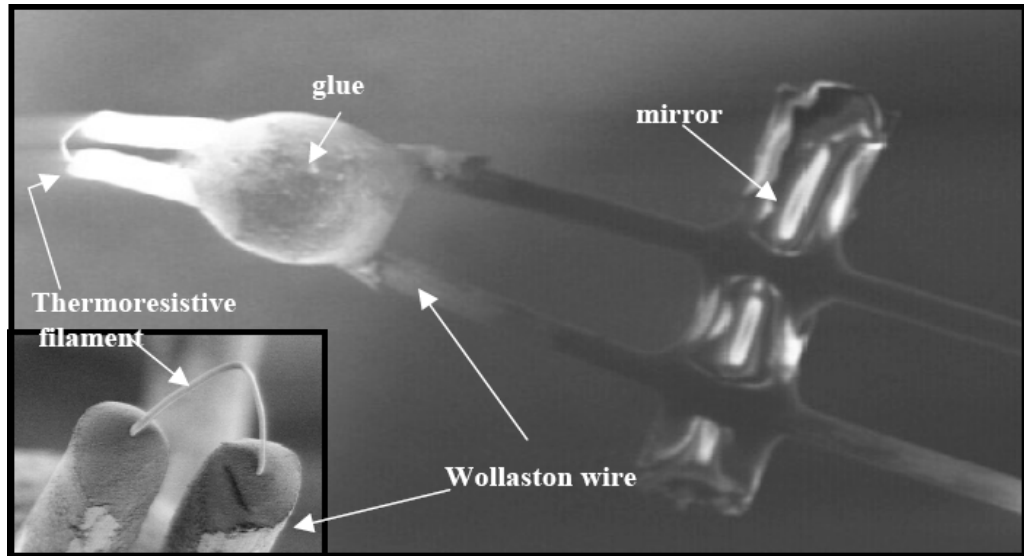


**Figure 5.1** SEM images of top view of the SThM probe cantilever and thermal element and magnified view of the thermal element [4].

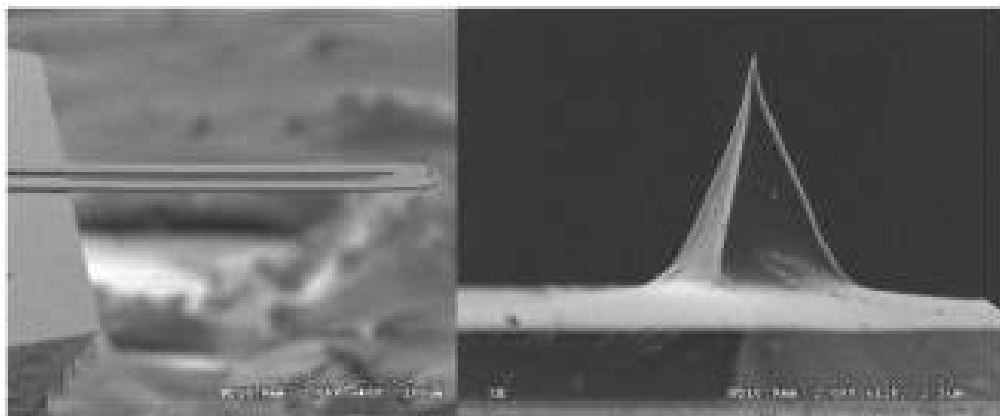


**Figure 5.2** SEM images of the AN-2 thermal probe used in nano-TA system and magnified view of the sharp probe (images from Anasys Instruments).

The effect of dehydration of lactose monohydrate crystals was investigated with the nano-TA system. In previous SThM measurements and literature, it had shown that lactose monohydrate samples displayed two peaks in the heating curve, the first due to dehydration, and the second due to melting [5].

So in this study, the thermal probe (AN-2) was stopped contacting and lifted up when the first peak appeared but not to move the probe away from the original position. The thermal measurement was then repeated on the same position to observe whether the first peak was present and whether the peak represents the lactose monohydrate dehydration.

## **5.3 Results and Discussions**

### **5.3.1 Young's Modulus Measurements on Materials Used for Tablet Formulation**

Twenty force-distance curves for each sample were collected. In one completed force curve, the approach and retract portions could be used to generate two gradients of loading forces versus indentation. The Hertz and Sphere-Plane model used in this work requires the total elastic deformations on the sample surfaces and no any deformations of the probe [6]. Hence the Young's modulus values should be derived from the process which is the most closest to elastic deformation. The retract curve, which have no loading forces were chosen to derive the Young's modulus values (Table 5.1).

**Table 5.1** Young's modulus values derived from retreat curves with AFM FESP probes

Sample	Young's modulus (GPa)
AZD 3409 HCl salt	0.53 (0.24)
AZD 3409 Malate salt	0.96 (0.37)
Lactose monohydrate	3.71 (0.67)
Avicel (MCC)	7.78 (3.01)
PVP	0.81 (0.15)
Crospovidone	0.29 (0.22)
Croscarmellose Sodium	0.048 (0.039)
Magnesium Stearate	0.019 (0.0036)

In table 5.1, the crystalline materials such as lactose monohydrate and MCC have higher E values, while the polymer materials such as crospovidone and croscarmellose sodium display lower E values. The Young's modulus is a parameter which relates the reversible deformation of material to applied stress, and associates with mechanical behaviour of material such as stiffness and strength [7]. Commonly, the ordered crystalline materials are harder than the polymers due to the strong interactions within the crystal structure. The Young's modulus for magnesium stearate is the smallest among all the samples. It should be noted that though for lubricant materials like magnesium stearate, the force measurements could be influenced by the very low friction forces. The loading forces on AFM probes could let probes slip on magnesium stearate surface and the slipping would further decrease the Young's modulus values in

the subsequent calculation.

There are various methods used to derive Young's modulus of material from tensile and compressive behaviour such as beam bending [8]. Most methods rely on the bulk material's response to stress which usually involves a relatively large amount of materials for testing. The AFM Young's modulus measurements use AFM probes as the nano-indentators to obtain the Young's modulus. This method only needs a small amount of materials, or even one single particle is enough for the Young's modulus determination. The results generated from single particles but not bulk materials would usually have small data variations (standard deviation) [9]. Another advantage of the AFM method is its high spatial resolution. Because of the use of sub-micron size of AFM probe indentator, any small heterogeneities on the sample surface will become detectable, as for example this has been exploited to find the amorphous domains at the surface of sorbitol [10].

### **5.3.2 HPMC and DCPD Young's Modulus with Temperature**

For HPMC, the Young's modulus was determined at each preset temperature.

The results are presented in Figure 5.3 and table 5.2

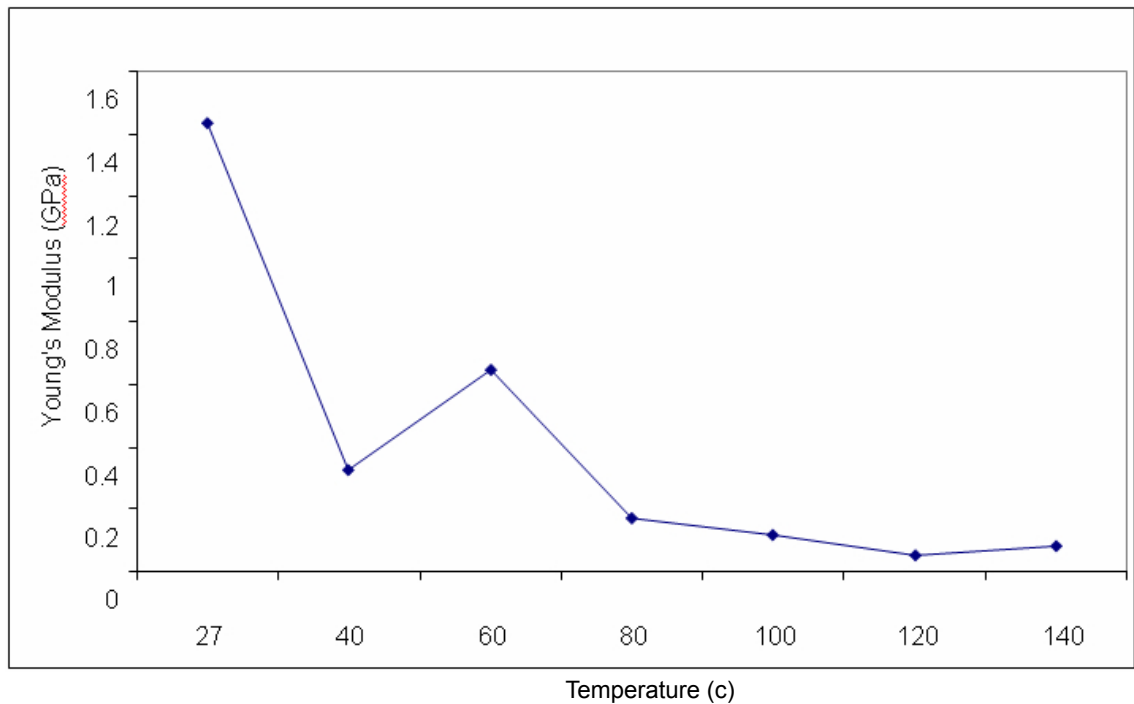


**Figure 5.3** The plot of E versus temperature results on HPMC.  $T_g$  temperature for HPMC is 120 °C.

**Table 5.2** Young's modulus of HPMC before and after heating and Young's modulus at  $T_g$  Temperature

Sample HPMC	Young's modulus (GPa)
Before heating (27 °C)	1.44 (0.50)
$T_g$ temperature (120 °C)	0.08 (0.05)
After heating (27 °C)	1.782 (0.50)

HPMC as a non crysalline solid material does not have a defined melting point. Amorphous materials including glass and polymers do not have a true melting point as there is no abrupt phase change at specific temperature. Instead, the change is gradual in terms of viscoelastic properties over a range of

temperature. That characteristic temperature at which changes in molecular organization can be observed is known as the glass transition temperature ( $T_g$ ) [11]. For polymers like HPMC, when the temperature is below  $T_g$ , the material is relatively brittle, when the temperature is above  $T_g$ , it becomes soft. So the mechanical properties such as Young's modulus would be expected to change from high to low over the range of the  $T_g$ .

At room temperature, HPMC has a Young's modulus value of 1.44 GPa. When the temperature rises, generally the Young's modulus declines. When the temperature was at the known  $T_g$  of 120 °C, the value of Young's modulus is 0.08 GPa. However, it is not possible to measure the Young's modulus after  $T_g$  because the deformation observed is no longer elastic and could not be fitted with the models employed (Figure 5.4). Another point is that the Young's modulus dramatically changes between 40 °C to 60 °C. A possible explanation could be that the moisture content within HPMC sample changed at this temperature. The changes of moisture can be associated with changes of the mechanical properties and the increase of water content usually decreases the value of Young's modulus [12-13]. It is possible that when the HPMC sample was heated from room temperature to 40 °C, that the moisture content with HPMC increased by absorbing the moisture in air [14].

From the data in table 5.2, the reversible nature the processes occurring at the

glass transition temperature can be confirmed in terms of Young's modulus. The Young's modulus value of HPMC after heating is similar to it before heating and much larger than it at the  $T_g$ .

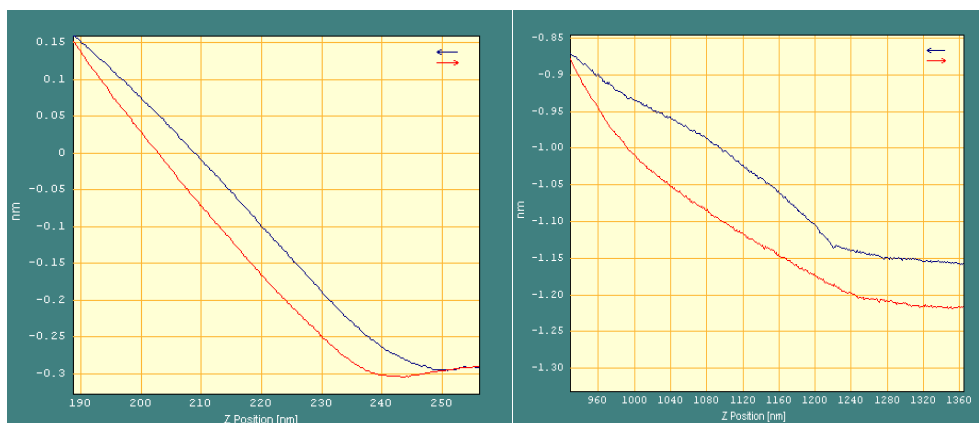


**Figure 5.4** Force-distance curves of HPMC at room temperature (left) and high temperature 140 °C (right). At high temperature, the retract force-distance curve is not applicable for linear gradient determination.

DCPD ( $\text{CaHPO}_4 \cdot 2\text{H}_2\text{O}$ ) is used as crystalline diluents in tablet formulation [15]. In the tablets containing DCPD, the dehydration of DCPD to its anhydrate form ACP ( $\text{CaHPO}_4$ ) during storage has been widely reported [16]. The dehydration can happen at low temperature (35 °C) and relative high humidity, but usually takes a long time (6 months) to occur under such conditions. It is well accepted that at higher temperature (>100 °C) the rate of dehydration of DCPD will increase. Although the nature of thermal pathway of DCPD to ACP is not well established, the DCPD-ACP phase transformation is known not to be just losing 2 molecules of lattice water but also involving forming an amorphous intermediate [17]. The rehydration of ACP to DCPD is known to be very difficult and hence the products of dehydration are stable.

The Young's modulus values of DCPD at room temperature and after heating for 30 minutes at 109 °C together with Young's modulus of ACP as control are listed in table 5.3.

**Table 5.3** Young's modulus values of DCPD before and after dehydration

DCPD Sample	Young's modulus (GPa)
DCPD	0.87 (0.60)
After heat	1.90 (0.54)
ACP control	1.75 (0.76)

The expected changes of crystal system from monoclinic for DCPD to triclinic for ACP [18] are not viewable in SEM images (Figure 5.5).

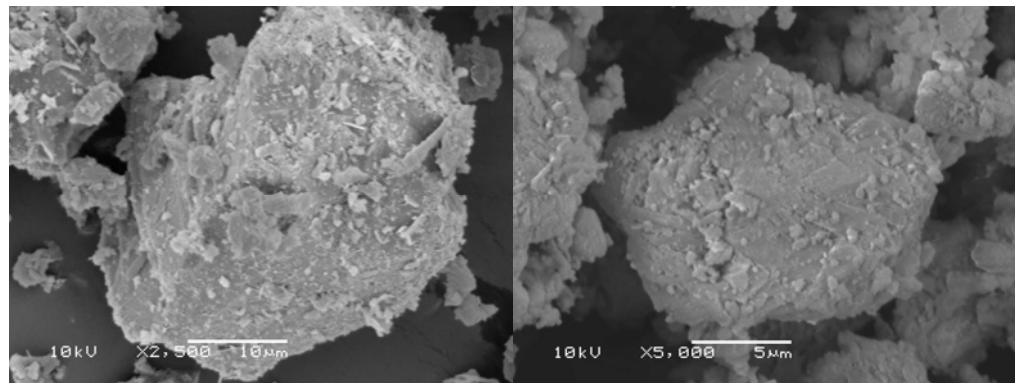


**Figure 5.5** SEM images of DCPD (left) and ACP (Right) samples used in Young's modulus measurements.

After heating to 109 °C for 30 minutes, the Young's modulus of the treated DCPD was 2 times higher than the untreated DCPD samples, the value being similar to those from an ACP control sample. Hence the treated DCPD sample

with the lost of lattice molecular H<sub>2</sub>O appears stiffer than the hydrated form. The amorphous intermediate was not found in the measurements. The characterizations in the flow and compression properties of DCPD and ACP have been documented in literature which also indicates that ACP is the material with high mechanical strength and the mean yield pressure of ACP is also 2 times higher than DCPD [19]. However, the dehydration of DCPD still needs to be confirmed by other methods such as X-Ray Diffractometry and thermal methods such as Differential Scanning Calorimetry.

### **5.3.3 Materials Melting Points Determined with SThM and Nano-TA System**

SThM was used to obtain the melting points of samples through local thermal analysis. After calibration, the original deflection-power curves could be transferred into the deflection-temperature curves which gave the information of melting points (Figure 5.6, 5.7). The heat generated by SThM passes to the sample surface through the thermal probe. The surface in most cases will expand on absorbing the heat, causing an upward deflection of the probe. When the temperature reaches the melting point of the sample, the surface will become soft and the probe will penetrate the surface which reflects on the deflection signal as an abrupt downwards turn of the deflection signal.

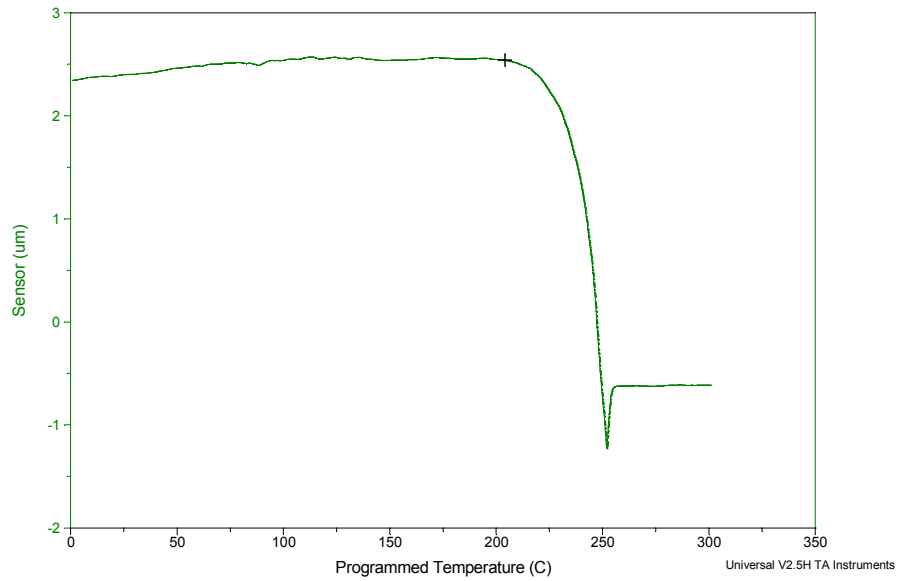


**Figure 5.6** A SThM local thermal analysis plot on AZD 3409 HCl salt. The melting point in the plot is 205.8 °C.

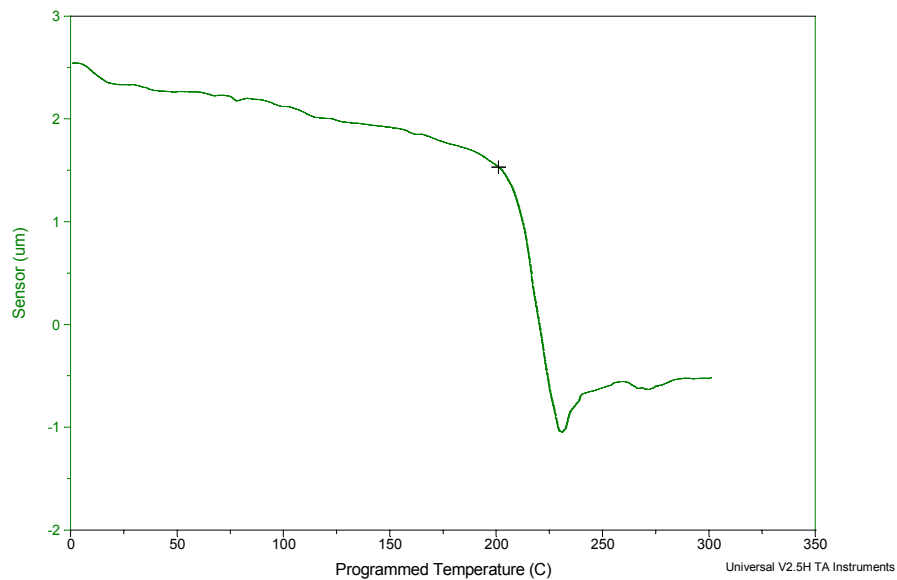


**Figure 5.7** A SThM local thermal analysis plot on AZD 3409 malate salt. The melting point in the plot is 199.3 °C.

The SThM local thermal analysis on the two API salts yields the melting points, for AZD 3409 HCl salt this is 205.2 (1.1) °C and for the AZD 3409 malate salt 199.6 (0.3) °C.

In the nano-TA system, the function and principle of SThM mode is the similar to the Explorer SThM, although the heater is now at the tip of the probe and not at its apex as in SThM. Other differences are in the size of probe and the rate of heating. The melting points of samples derived from the nano-TA system local thermal analysis are presented in table 5.4.

**Table 5.4** Melting points of materials from nano-TA system local thermal analysis

Sample	Melting Point, °C
AZD 3409 HCl salt	121.8 (0.3)
AZD 3409 malate salt	116.3 (0.2)
HPMC	(T <sub>g</sub> ) 153.3 (0.3)
Lactose monohydrate	160.7 (0.5), 207.5 (0.7)

The values of melting points of samples from nano-TA are not the same as those derived from Explorer SThM (Figure 5.6 and Figure 5.7), with those from nano-TA being considerably lower. As mentioned above, the scale and heating rate are not the same for two methods. The heating rate used in nano-TA system is usually below 10 °C/s, while in Explorer SThM the rate is usually around 10 °C/min. For thermal measurements, the rate of heat can influence the final results of melting points [20]. In the nano-TA system, the radius of contact hole which the probe made is about 50 nm (Figure 5.8) while in explorer SThM the radius is about 1 µm. The differences on the scale of

measurement may contribute to the discrepancy through the effects of confinement [21]. In nano-TA system, the measurement may be made on individual faces of the crystals rather than the large contact area in explorer SThM. The crystal faces are believed to have different melting point temperatures [22]. And finally, the calibration materials in nano-TA system and explorer SThM are different. In nano-TA system, the standard calibration samples are polymer films while the explorer SThM using crystalline standards. But the samples measured are not always as the same as the calibration samples in terms of crystalline and polymer. The differences on mechanical properties (expansion, softening) and thermal properties (heat of fusion, change of heat capacity) between calibration standards and measured samples [23] can influence the results of melting points determination in both nano-TA and explorer SThM system.

In table 5.4, lactose monohydrate sample had two readings. That is because there are two peaks existing in the plots of lactose monohydrate nano-TA results (Figure 5.9). The first peak in the thermal plot could possible be the dehydration temperature of lactose monohydrate [24]. However, it should be further confirmed with other thermal measurement techniques such as DSC.

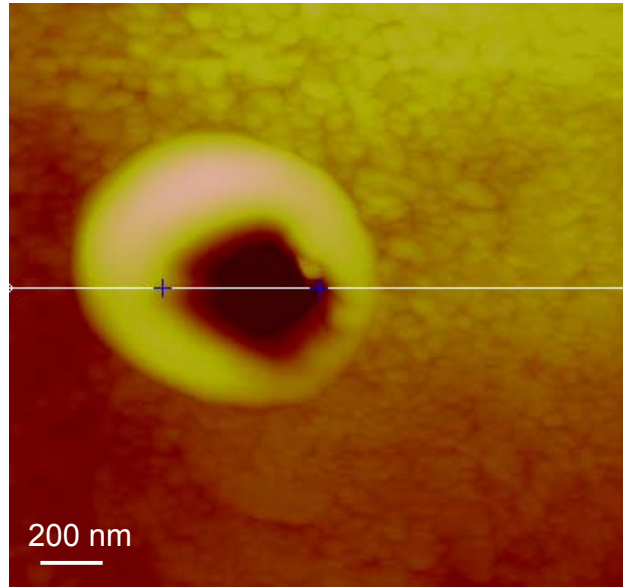


**Figure 5.8** A tapping mode image of a hole which nano-TA local thermal analysis made on lactose monohydrate surface. The radius of the hole is 219 nm as measured by Nanoscope (V7.0) section function.

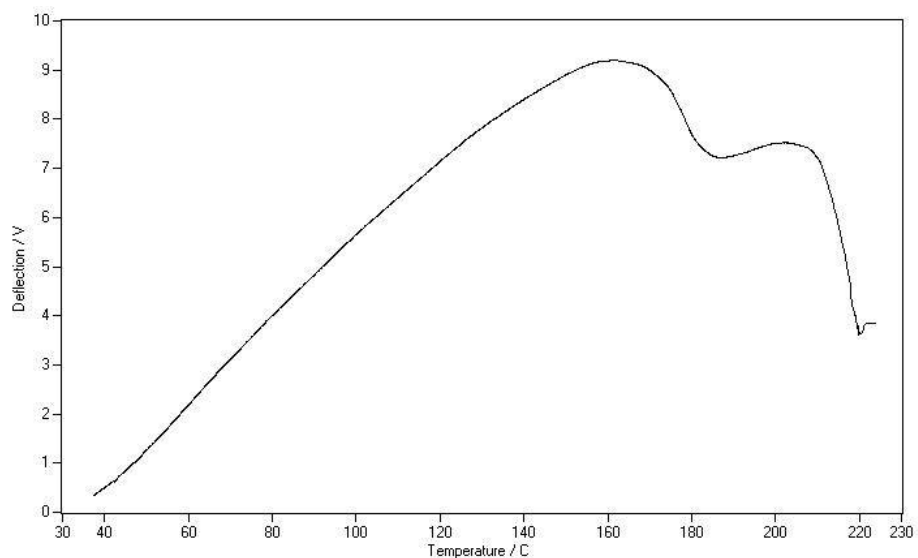


**Figure 5.9** A nano-TA local thermal analysis plot of lactose monohydrate. There are two peaks in the plot. The first peak is the dehydrate temperature at 160.7 °C. And the second peak is the melting temperature at 207.5 °C.

The DCS measurements were made on AZD 3409 HCl salt, malate salt, lactose monohydrate and DCPD. In the DSC study, the mass of samples put in pans

was 8-12 mg and the heating rate was 10 °C/min. The samples before measurements were all kept in the chamber at 25 °C for 10 minutes. The plots of heat flow (W/g) versus temperature were recorded. The melting point temperature then can be read out using TA universal analysis. The results are listed in table 5.5. The two peaks in plot of DSC (Figure 5.10) have further confirmed that the dehydration of lactose monohydrate at 151.65 °C which is very close to the first peak temperature 145.15 °C observed using Nano-TA system. Also the DSC results on DCPD confirm that the dehydration temperature is at 103.08 °C (Figure 5.11).

**Table 5.5** Melting points of materials measured by DSC method (onset temperature)

Sample	Melting point (°C)
AZD 3409 HCl salt	152.2
AZD 3409 malate salt	137.0
Lactose monohydrate	145.2, 207.9
DCPD	103.1, 177.2

The melting point temperatures in table 5.5 are relative higher than those in table 5.4. Except the factors such as heating rate [20] and scale of measurements [21], the phenomenon of premelting (or surface melting) where a quasi-liquid film can form on crystalline surfaces will lead to a lower melting point results with SThM than the bulk melting point with DSC [22].

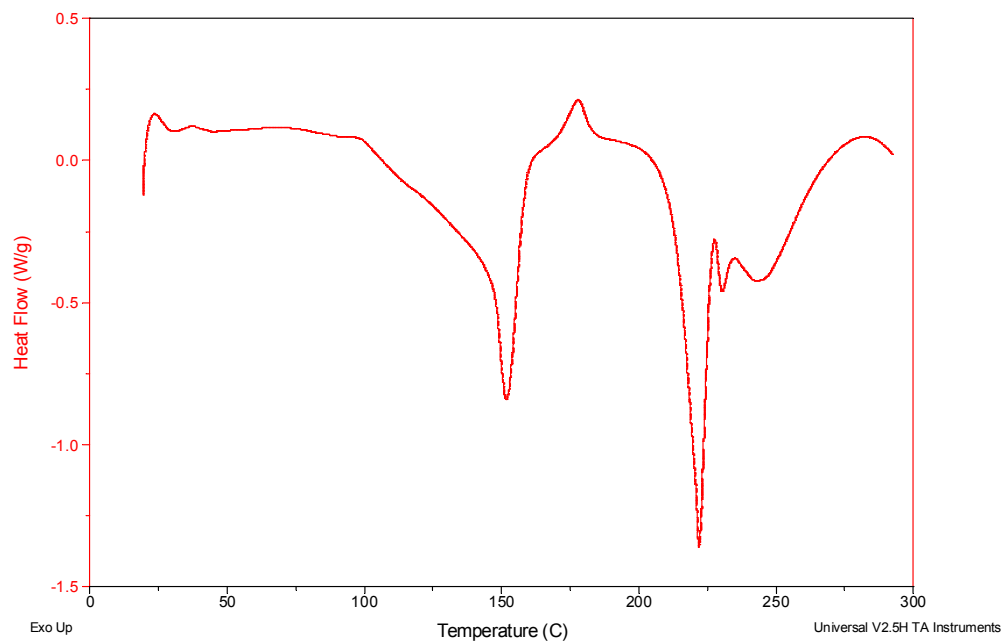


**Figure 5.10** A DSC plot of lactose monohydrate. The first peak is the crystal dehydration onset temperature at 145.2 °C and the second peak is the melting onset temperature at 207.9 °C.

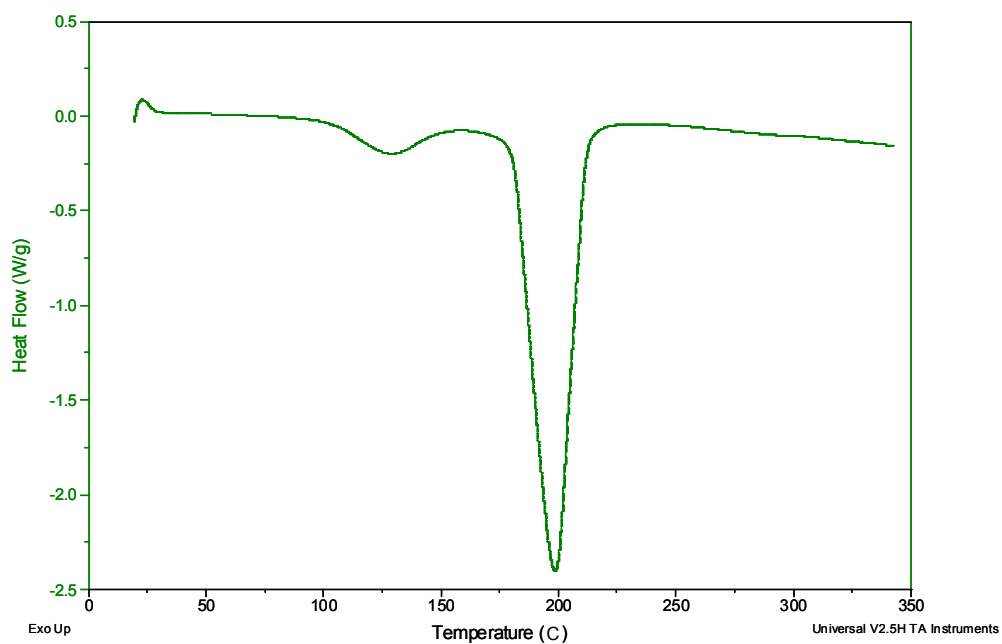


**Figure 5.11** A DSC plot of DCPD. The first peak is the crystal dehydration temperature at 103.1 °C and the second peak is the melting temperature at 177.2 °C.

### 5.3.4 Lactose Monohydrate Dehydration and Rehydration Study with the Nano-TA System.

In 5.3.3, the dehydration of lactose monohydrate was noticed using DSC and SThM. To avoid the influence of compressed sample surface required for SThM analysis, large re-crystallized lactose monohydrate crystals were prepared. The results (Figure 5.12) are very similar to those seen on the compressed samples, still two peaks were observed and the first peak at around 150 °C and the second peak at around 185 °C.

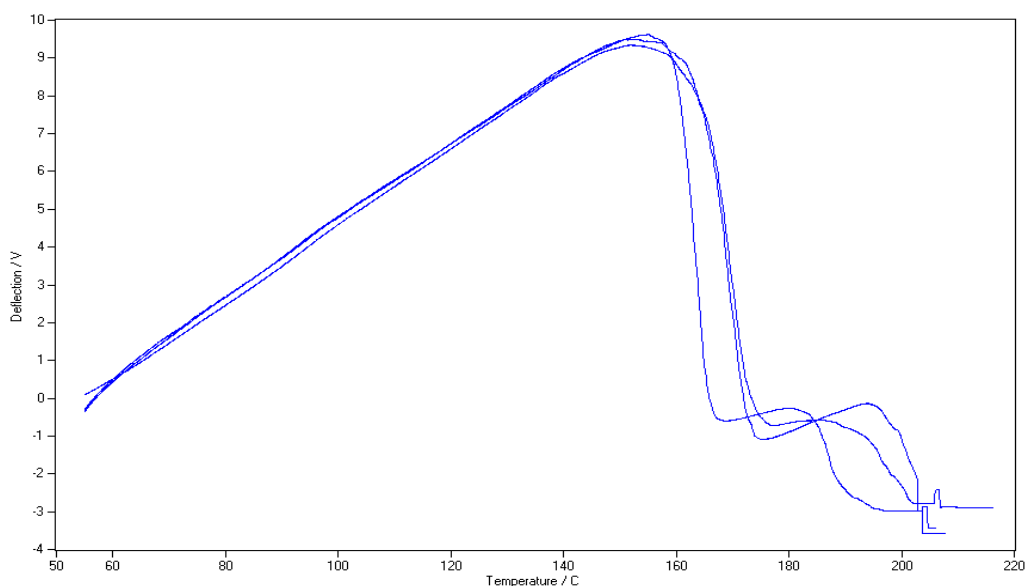


**Figure 5.12** Three local thermal analysis plots on re-crystallized lactose monohydrate crystal surface with nano-TA system. The first peak is at a temperature of around 150 °C and is related to dehydration and the second peak is at a temperature of around 185 °C for the melting point.

It confirms that the dehydration detected by nano-TA local thermal analysis is not the artificial fact caused by possible phase changes induced in the compression process. However, because the dehydration processes on the

crystal surface may involve in some changes of topography, the variations of final melting temperature are becoming larger.

To further this study the LTA was stopped and lifted up after the dehydration point reached, keeping the probe at the same spatial position and the restarting the LTA measurements at full range. The result (Figure 5.13) shows that the first peak representing the dehydration is now absent and only the second peak representing the melting of the anhydrous form is observed.

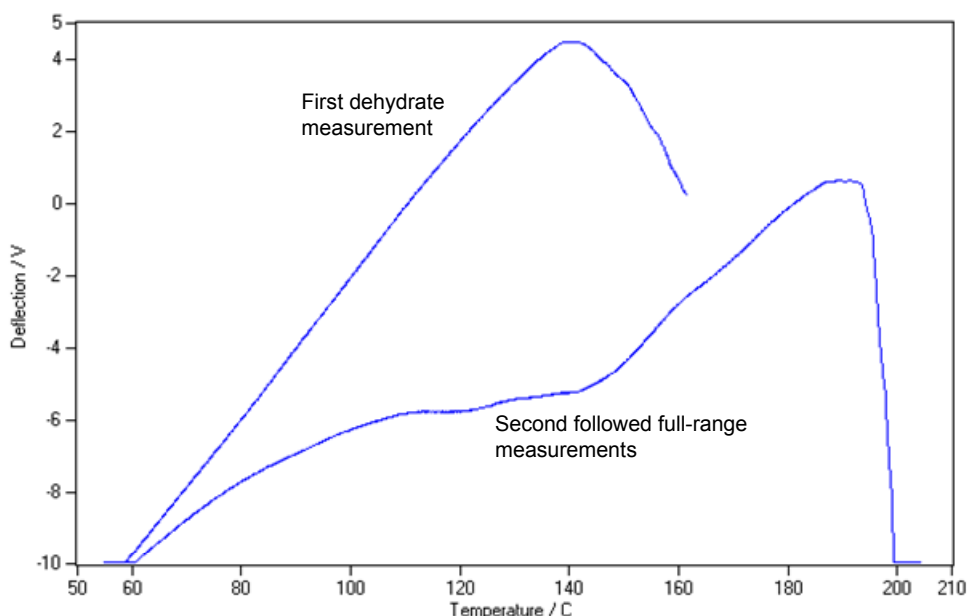


**Figure 5.13** Nano-TA local thermal analysis to confirm the dehydration of lactose monohydrate: the upper curve is the first measurement stopped at the dehydrate point (138 °C) and the lower curve is the followed measurement at the same position.

The rehydration of lactose crystals was also studied with nano-TA system local thermal analysis. A single re-crystallized lactose monohydrate crystal was measured with nano-TA local thermal analysis. The measurement was stopped

at the temperature of dehydration. To promote rehydration the sample was exposed to room humidity (35.4%) for 50 minutes before a second LTA measurement. Unlike the ACP which is not easily to rehydrate, anhydrous lactose is very likely to rehydrate [25]. Consistent with this literature, the rehydration of the lactose crystal (Figure 5.14) is observed by the nano-TA local thermal analysis.

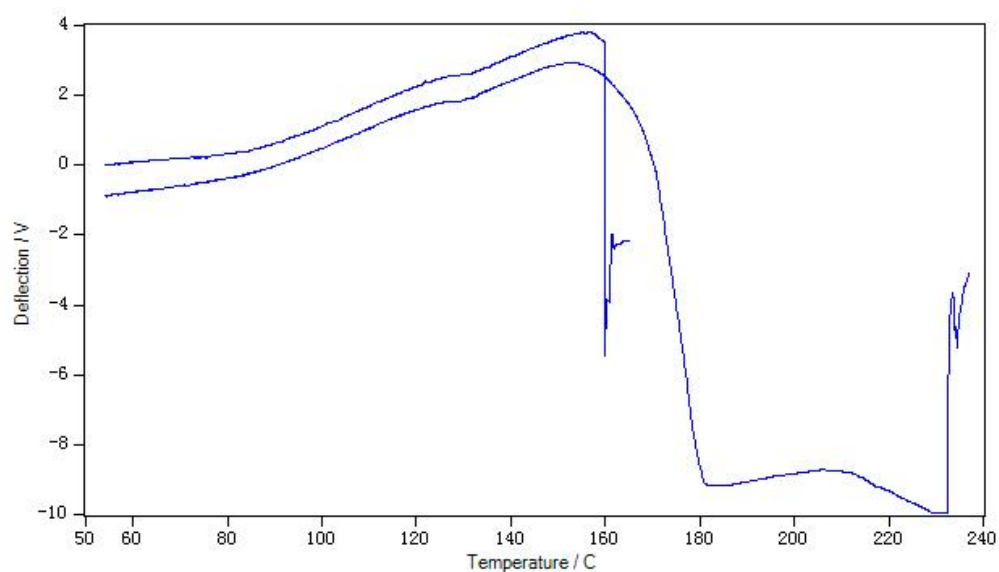


**Figure 5.14** Nano-TA local thermal analysis to confirm the rehydration of lactose monohydrate: the upper curve is the first measurement stopped at the dehydrate point (154 °C) and the lower curve is the followed measurement after 50 minutes at the same position. Dehydration point (150 °C) and melting point (209 °C) can be observed.

## 5.4 General Conclusions

In this chapter, the nanoscale measurements on some fundamental properties of a selection of pharmaceutical materials have been demonstrated. The Young's

moduli of materials used in tablet formulation have been measured with an AFM force measurement method. In the AFM force measurements, the AFM probe which is operated as a nano-indentator could acquire the Young's modulus on the material surface with sub-micron spatial resolution. In addition, the changes of material mechanical property with temperatures can also be studied with AFM and the hot-stage accessory. In particular the changes to Young's modulus on dehydration are demonstrated. The thermal properties of individual crystals are also measured by SThM and nano-TA. Both techniques are based on an AFM type approach and have the advantage of high spatial resolution. This is especially so with the nano-TA system. Some of the quantitative measurements between DSC, SThM and nano-TA are quite different. Reasons for this include the fact that the rates of heating in DSC, SThM and nano-TA system are very different, the masses studied and the methods by which signals are obtained.

The work in this chapter has opened a new window for materials identification based on the thermal and mechanical properties including Young's modulus, surface free energy and melting point at the sub-micron resolution on surface. This is now exploited in the following chapter.

## References

1. I. N. Sneddon. The relation between load and penetration in the axisymmetric boussinesq problem for a punch of arbitrary profile. *Int. J. Eng. Sci.* **3** (1965) 47.
2. M. Perkins, S. J. Ebbens, S. Hayes, C. J. Roberts, C. E. Madden, S. Y. Luk and N. Patel. Elastic modulus measurements from individual lactose particles using atomic force microscopy. *Int. J. Pharm.* **332** (2007) 168.
3. A. H. Kibbe. Handbook of pharmaceutical excipients. 3<sup>rd</sup> Edition. American Pharmaceutical Association. Washington DC (2000).
4. S. Gomès, N. Trannoy and P. Grossel. DC thermal microscopy: study of the thermal exchange between a probe and a sample. *Meas. Sci. Technol.* **10** (1999) 805.
5. M. D. Ticehurst, P. York, R. C. Rowe and S. K. Dwivedi. Characterisation of the surface properties of  $\alpha$ -lactose monohydrate with inverse gas chromatography, used to detect batch variation. *Int. J. Pharm.* **141** (1996) 93.
6. H. Hertz. On the contact of elastic solids. *J. Reine Angew. Math.* **92** (1881) 156.
7. C. Li, A. Ohmori and R. McPherson. The relationship between microstructure and Young's modulus of thermally sprayed ceramic coatings. *J. Mater. Sci.* **32** (1997) 997.
8. B. C. Hancock, G. T. Carlson, D. D. Ladipo, B. A. Langdon and M. P. Mullarney. Comparison of the mechanical properties of the crystalline and

- amorphous forms of a drug substance. *Int. J. Pharm.* **241** (2002) 73.
9. S. F. Yap, M. J. Adams, J. P. K. Seville and Z. Zhang. Single and bulk compression of pharmaceutical excipients: evaluation of mechanical properties. *Powder Technol.* **185** (2008) 1.
10. S. Ward, M. Perkins, J. X. Zhang, C. J. Roberts, C. E. Madden, S. Y. Luk, N. Patel and S. J. Ebbens. Identifying and mapping surface amorphous domains. *Pharm. Res.* **22** (2005) 1195.
11. J. Jackle. Models of the glass transition. *Rep. Prog. Phys.* **49** (1986) 171.
12. N. E. Marcovich, M. M. Reboredo and M. I. Aranguren. Dependence of the mechanical properties of woodflour-polymer composites on the moisture content. *J. Applied Polym. Sci.* **68** (1998) 2069.
13. G. E. Amidon and M. E. Houghton. The effect of moisture on the mechanical and powder flow properties of microcrystalline cellulose. *Pharm. Res.* **12** (1995) 923.
14. T. P. Labuza, A. Kaanane and J. Y. Chen. Effect of temperature on the moisture sorption isotherms and water activity shift of two dehydrate foods. *J. Food Sci.* **50** (2006) 385.
15. K. Kachrimanis, M. Petrides and S. Malamataris. Flow rate of some pharmaceutical diluents through die-orifices relevant to mini-tableting. *Int. J. Pharm.* **303** (2005) 72.
16. M. Landin, B. Perez-Marcos, M. Casalderrey, R. Martinez-Pacheco, J. L. Gomez-Amoza, C. Souto, A. Concheiro and R. C. Rowe. Chemical stability of

acetylsalicylic acid in tablets prepared with different particle size fractions of a commercial brand of dicalcium phosphate dihydrate. *Int. J. Pharm.* **107** (1994) 247.

17. T. Miyazaki, K. Sivaprakasam, J. Tantry and R. Suryanarayanan. Physical characterization of dibasic calcium phosphate dihydrate and anhydrate. *J. Pharm. Sci.* **98** (2009) 905.

18. S. V. Dorozhkin and M. Epple. Biological and medical significance of calcium phosphates. *Angew. Chem. Int. Ed.* **41** (2002) 3130.

19. C. Doldan, C. Souto, A. Concheiro, R. Martinez-Pacheco and J. L. Gomez-Amoza. Dicalcium phosphate dihydrate and anhydrous dicalcium phosphate for direct compression: a comparative study. *Int. J. Pharm.* **124** (1995) 69.

20. L. Bond, S. Allen, M. C. Davies, C. J. Roberts A. P. Shivji, S. J. B. Tendler, P. M. Williams and J. Zhang. Differential scanning calorimetry and scanning thermal microscopy analysis of pharmaceutical materials. *Int. J. Pharm.* **243** (2002) 71.

21. M. Alcoutlabi and G. B. McKenna. Effects of confinement on material behaviour at the nanometer size scale. *J. Phys.: Condens. Matter* **17** (2005) 461.

22. B. Pluis, A. W. D. van der Gon, J. W. M. Frenken and J. F. van der Veen. Crystal-face dependence of surface melting. *Phys. Rev. Lett.* **59** (1987) 2678.

23. H. Fischer. Calibration of micro-thermal analysis for the detection of glass

transition temperatures and melting points. *J. Therm. Anal. Calorim.* **92** (2008) 625.

24. S. Garnier, S. Petit, F. Mallet, M. N. Petit, D. Lemarchand, S. Coste, J. Lefebvre and G. Coquerel. Influence of aging, grinding and preheating on the thermal behaviour of  $\alpha$ -lactose monohydrate. *Int. J. Pharm.* **361** (2008) 131.

25. L. O. Figura and M. Epple. Anhydrous  $\alpha$ -lactose: a study with DSC and TXRD. *J. Thermal Anal.* **44** (1995) 45.

## **Chapter 6: Surface Energy and Thermal Nanoscale Characterization and Mapping of a Model Solid Formulation**

### **6.1 Introduction**

In pharmaceutical stability testing, the chemical and physical stability results of solid form products under the stress conditions (temperature, humidity, light) are strongly related with individual ingredients (APIs, excipients, container system and packing materials) [1]. The solid-state characterizations before formulation will help in selecting potential candidates from polymorphism crystals and avoiding unexpected phase transitions [2]. Therefore, the physical and chemical characterizations of APIs and excipients at early stage are essential for optimize consistent product performance. But the phase transitions can also be induced by processes of dosage form preparation and manufacturing [3] and other importance source of phase transitions is from API-excipients interactions [4]. Such transformations need be examined during or after the stress conditions testing. The changes of solid-state properties can be observed from the appearance (including color, shape, odor and integrity), mechanical properties (including friability, disintegration and hardness) and degradation of APIs or excipients [1]. The chromatographic methods such as High-Performance Liquid Chromatography (HPLC) [5] and Thin-Layer chromatography (TLC) [6] and spectroscopic methods such as Infra-Red

spectroscopy (IR), Attenuated Total Reflectance Infra-Red spectroscopy (ATR-IR), Near Infra-Red spectroscopy (NIR) [7], and Raman spectroscopy [6] are widely used to detect the chemical degradations and solid-state phase transitions. With the developments of drug delivery device, the distribution of APIs within the system during the stress storage conditions testing becomes interested since it relates with the function of the device and selection of proper excipients. Such distribution information can be acquired from a specific spectral feature in the NIR mapping [8] or from a combination of ions in the Time-of-Flight Secondary Ion Mass Spectrometry (ToF-SIMS) mapping [9]. The differences on the mechanical (surface free energy, Young's modulus) and thermal properties (melting point, transition temperature) between APIs and excipients, different polymorphism, and crystalline and amorphous can be employed to generate material's distribution map with the Scanning Probe Microscopy (SPM). In the extremely case where the phase transitions occur among polymorphs, solvates/hydrates and crystalline/amorphous forms [3], the discrepancy in mechanical and thermal properties may be more considerable and the only option to identify materials and generate distribution maps when the samples emitted fluorescence scattering during Raman measurements [10]. The distribution maps built on the high resolution sub-micron topography images obtained from SPM can meet the increasing demands for the characterizations of nano drug delivery systems [11].

In this chapter, the surface free energy and thermal property of materials are used as criteria for material's identification and distribution on a model binary formulation surface. The standard surface free energy and thermal property values are derived from AFM probe adhesion force measurements and nano-TA local thermal analysis on pure AZD 3409 malate salt and lactose monohydrate. The model binary formulations mixtures are made of AZD 3409 malate salt and lactose monohydrate in the weight ratios of 20:80, 50:50 and 80:20 w/w. The mixtures are well mixed using a heptane slurry method and compressed into 13mm discs. The surfaces of the discs are first characterized using ATR-IR, NIR, ToF-SIMS to detect any phase transitions during preparation processes and draw both material bulk and surface distribution maps on model binary discs. AFM probe adhesion force measurements and nano-TA local thermal analysis are carried out at the same position on the model binary disc's surface. The information of surface free energy and thermal properties at the same position are integrated to identify AZD 3409 malate salt and lactose monohydrate on the binary tablet surface.

## **6.2 Materials and Methods**

AZD 3409 malate salt and lactose monohydrate were mixed using a heptane slurry method in the weight ratios of 20:80, 50:50 and 80:20 w/w. The dry slurry mixtures (0.1g) were compressed using a 13 mm die. The binary mixture

discs were examined by ATR-IR with diamond transmitting crystal (Thermal Nicolet 6700, Fisher scientific, UK) on several positions and compared with IR (Thermal Nicolet 5700, Fisher scientific, UK) spectra of pure AZD 3409 malate salt and lactose monohydrate discs. The mixture discs were also analysed with NIR (NIR spectrometer PL10, Perkins, USA) and ToF-SIMS (ION-TOF GmbH, Münster, Germany) to locate material distribution at the bulk and surface.

The AFM (Enviroscope-AFM, Veeco) probe adhesion force measurements were made on pure sample discs to derive the surface free energy values as criteria. The positions of adhesion force measurements were recorded using AFM tapping mode imaging method. The surface free energy values derived from adhesion forces were located in the tapping image to generate a surface free energy map. Because the scale of adhesion forces measurements is usually within 100 nm, the integration of the contact area of force measurements and the tapping image should be valid.

The nano-TA (Anasys Instruments) local thermal analysis measurements were also made on pure sample discs to obtain the thermal properties (melting point temperature). The local thermal analysis measurements examined the surface of binary mixtures discs as the materials can be identified based on their melting points.

Finally, the two methods were applied together on the binary mixture discs. First, the nano-TA system was employed to make a large hole at certain area as a marker. Adhesion force measurements were then made around that area by relocating the marker hole in AFM tapping image. The force measurements were carried out in the position where the topography was significant and easily recognized and the relative distances from the marker hole were recorded. Then nano-TA LTA measurements were made on those positions by finding the marker hole in the tapping image and relocating to the relative distances from the marker. The melting points on these positions plus the surface free energy values were used together to identify materials on the model binary formulation surface.

## **6.3 Results and Discussions**

### **6.3.1 Characterization of Model Binary Mixtures Discs**

IR and ATR-IR spectra are usually used to detect any chemical or phase changes between two batches of samples [12]. In particular, ATR-IR can detect changes on a sample surface with minimum sample preparation. The spectra results are presented in Figure 6.1 and 6.2. The ATR-IR or IR spectra can be divided into two regions. The left half above  $2000\text{ cm}^{-1}$ , usually contains few peaks but useful diagnostic information. The right half below  $2000\text{ cm}^{-1}$ , contains many peaks, many of which are difficult to confidently assign to any

particular group. However, the complex pattern of peaks in the low wavenumber region (below  $1200\text{ cm}^{-1}$ ) is unique for a material (i.e. fingerprint region). In the ATR-IR spectra of powder and discs, the coincidences of peaks both in left half and fingerprint regions indicates that the powder and compressed discs are the same compounds and that no significant changes have occurred during the production of the disc[13].

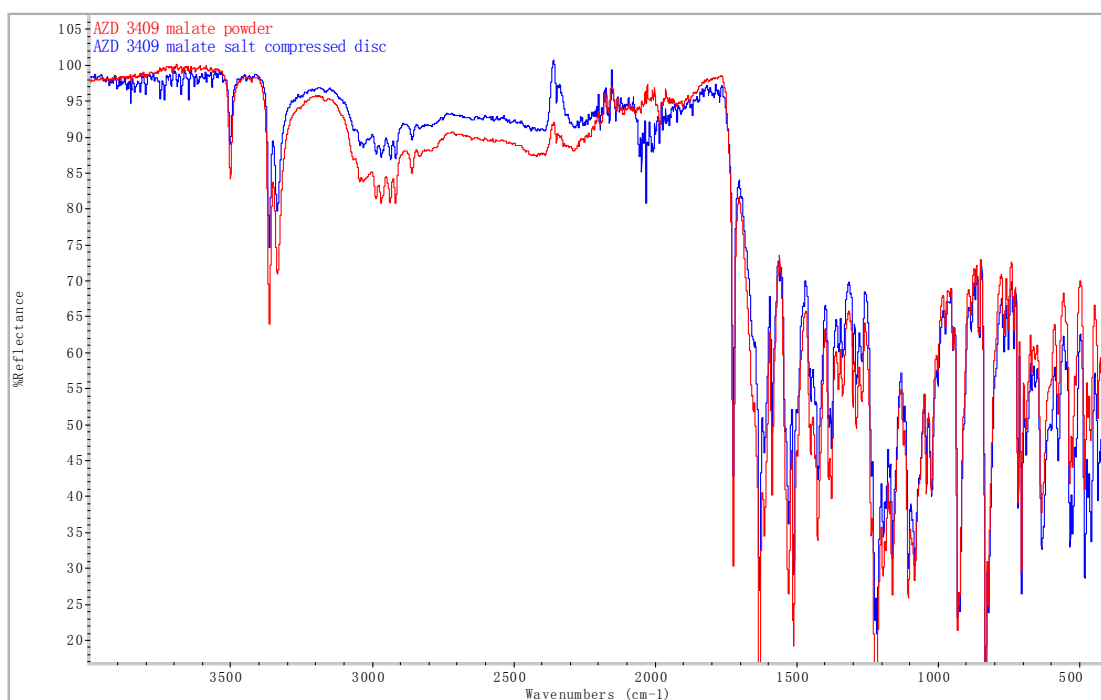


**Figure 6.1** ATR-IR spectra of AZD 3409 malate salt powder and compressed disc. The comparison between the two spectra shows that there are no changes of chemical components during the compression processes.

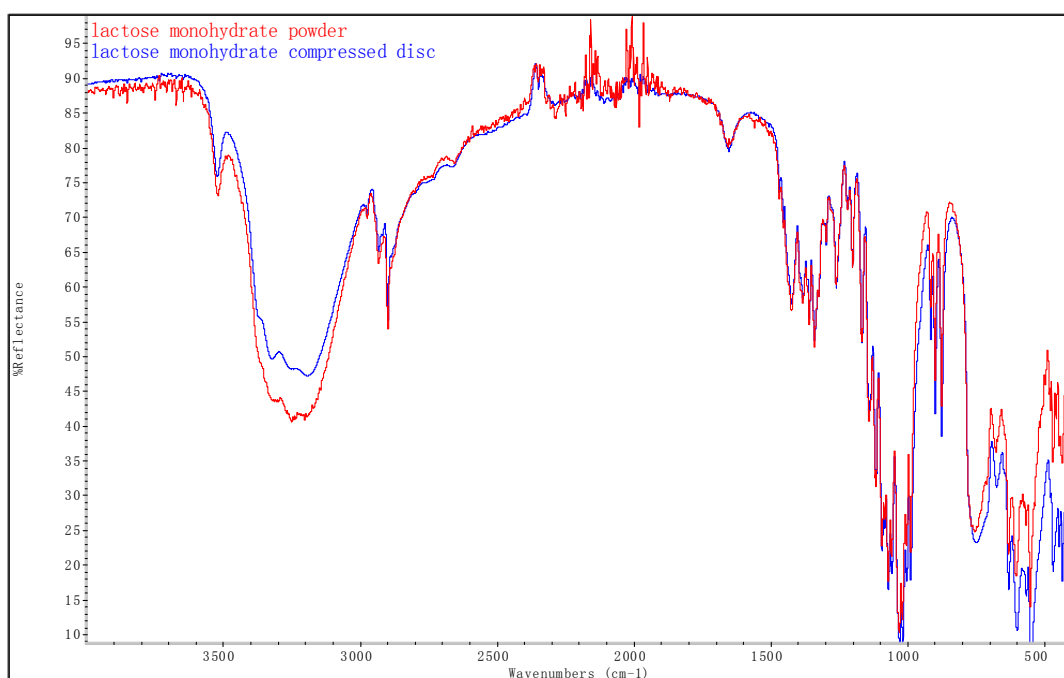


**Figure 6.2** ATR-IR spectra of lactose monohydrate powder and compressed disc. The comparison between two spectra shows that there are no changes of chemical components during the compression processes.

Five ATR-IR spectra were collected on each binary mixtures tablet surface. The average of five spectra was compared with the theoretical result derived from spectra math function. The spectra math calculated the theoretical spectrum from the spectrum of pure compressed material based on the weight ratio of two components in binary mixtures.

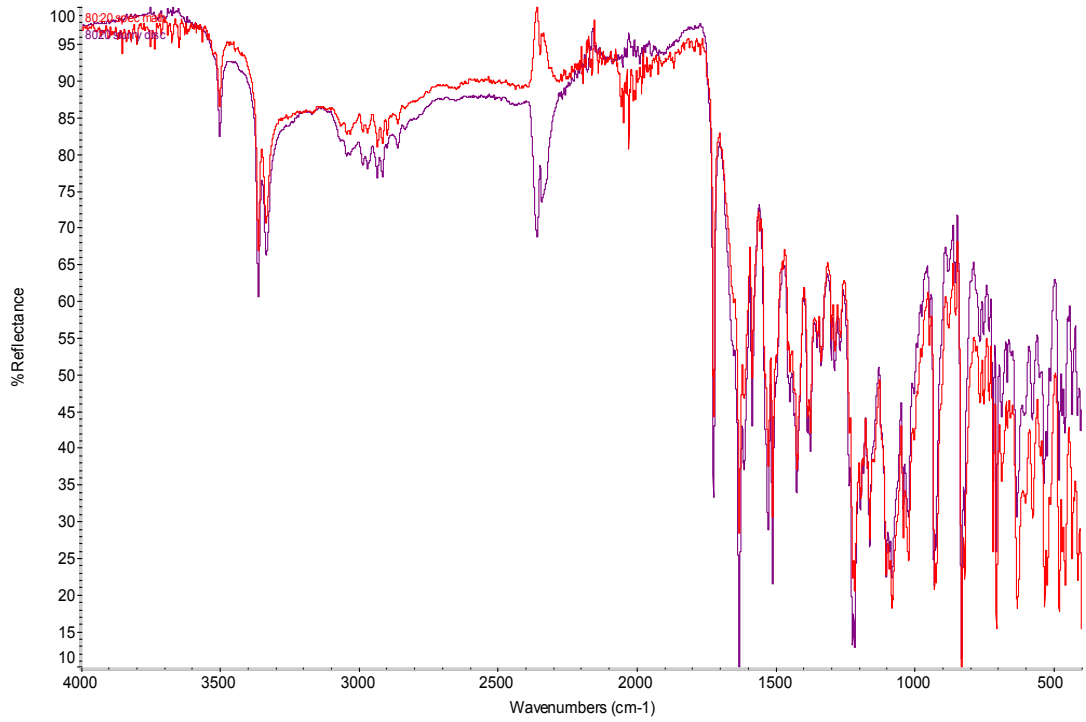


**Figure 6.3** Spectra math spectrum (red) and actual ATR-IR average spectrum from 5 measurements on 80: 20 w/w binary mixtures disc.

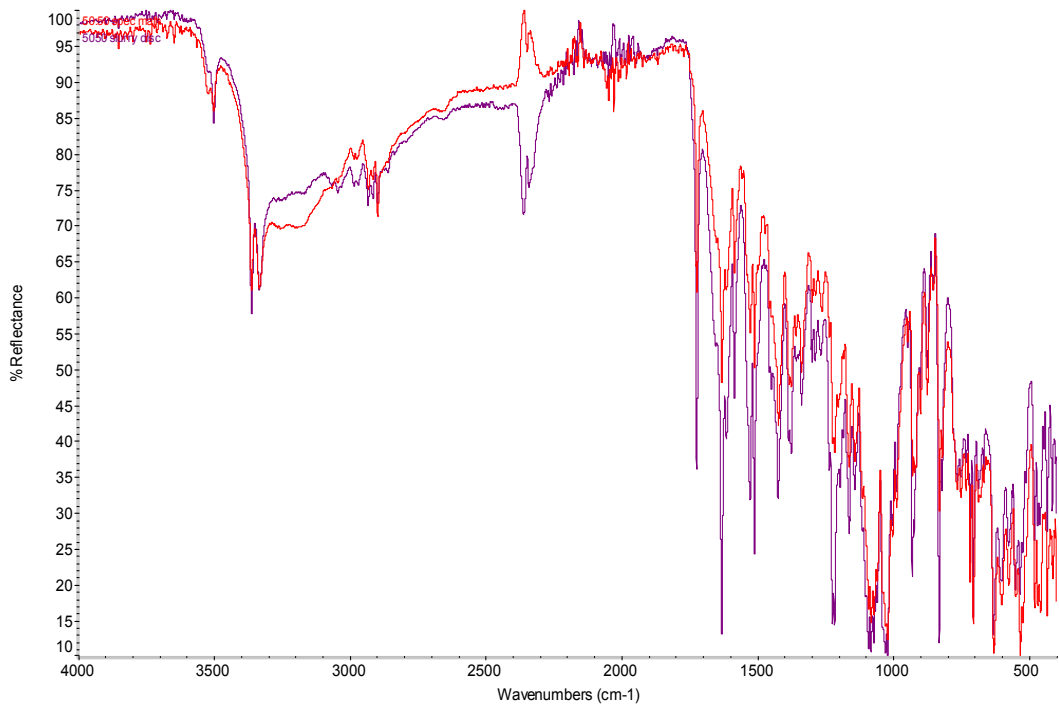


**Figure 6.4** Spectra math spectrum (red) and actual ATR-IR average spectrum from 5 measurements on 50: 50 w/w binary mixtures disc.

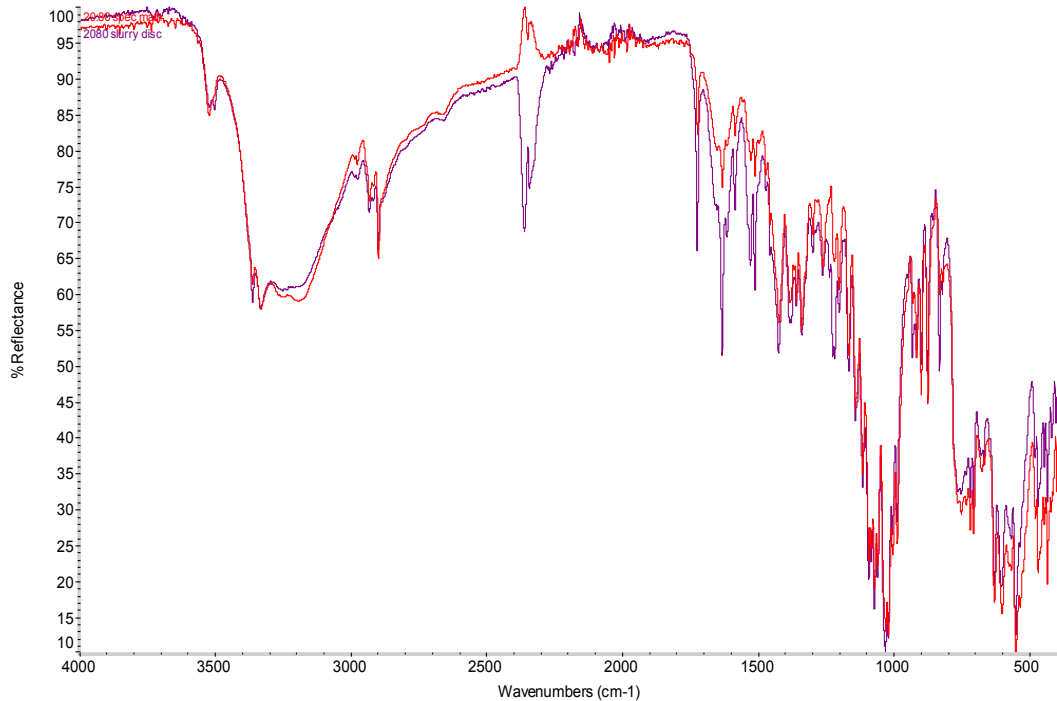


**Figure 6.5** Spectra math spectrum (red) and actual ATR-IR average spectrum from 5 measurements on 20: 80 w/w binary mixtures disc.

Comparison of the spectra math results and the ATR-IR spectra shows that the reflectance patterns are almost identical. The similarity indicates that the distribution of two materials at the surface and near surface is close to the bulk weight ratio.

NIR spectroscopy is a spectroscopic method using the near infrared band (800-2500 nm, wavenumber from 12821-4000  $\text{cm}^{-1}$ ) of the electromagnetic spectrum. The advantage of NIR is that near infrared radiation can penetrate deeper into samples (several hundreds micrometers) than mid infrared and hence provides more reflective data of the bulk. After calibration using a high reflectance ceramic standard, the NIR spectra of pure AZD 3409 malate salt

and lactose monohydrate were collected. The compressed disc made from a simple mixed powder with 50:50 w/w was also measured with NIR spectra mapping. The full spectra were then correlated with the pure material's NIR spectrum to generate two complementary NIR chemical images (Figure 6.6). The same measurements were made on compressed discs of slurry mixtures of 80:20 w/w, 50:50 W/w and 20:80 w/w. The results are presented in Figure 6.7, 6.8 and 6.9.

Because the bands in NIR are very broad and the spectra are much more complex than IR, it is difficult to assign specific peaks to chemical components. This is why the correlation (or principal components analysis) method was used in Figure 6.6-6.9. The clear differences between Figure 6.6 and 6.8 for the 50: 50 w/w mixture discs indicate that the heptane slurry mixing method achieves a more even material distribution in the discs. The NIR spectrum of pure lactose monohydrate shows a stronger signal than pure AZD 3409 malate salt because of the water in the crystal lattice. So in the 20:80 w/w slurry compressed disc where the lactose content is high, the signal of AZD 3409 malate salt is relatively weak and difficult to observe.

NIR spectroscopy is an effectively bulk technique and hence less related to surface properties and with a resolution (25  $\mu\text{m}$ ) much lower than AFM measurements. To help bridge this gap ToF-SIMS was employed to analyze the

surfaces of the slurry compressed discs.

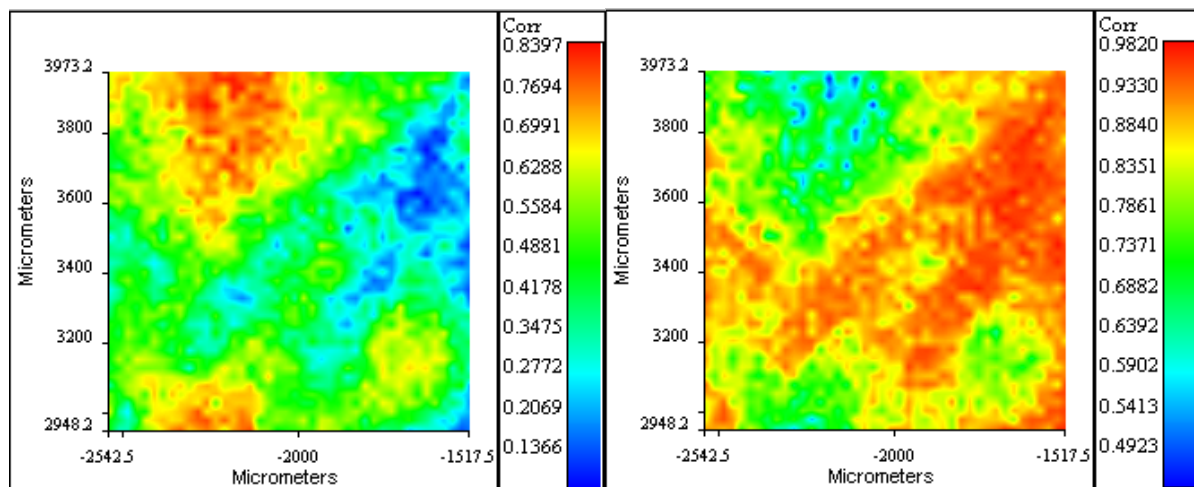


**Figure 6.6** the NIR chemical images (1x1 mm<sup>2</sup>) of a simple mixed compressed 50:50 w/w disc. Left map is the spectra correlated by AZD 3409 malate salt standard NIR spectrum. Right is the spectra correlated by lactose monohydrate standard NIR spectrum.

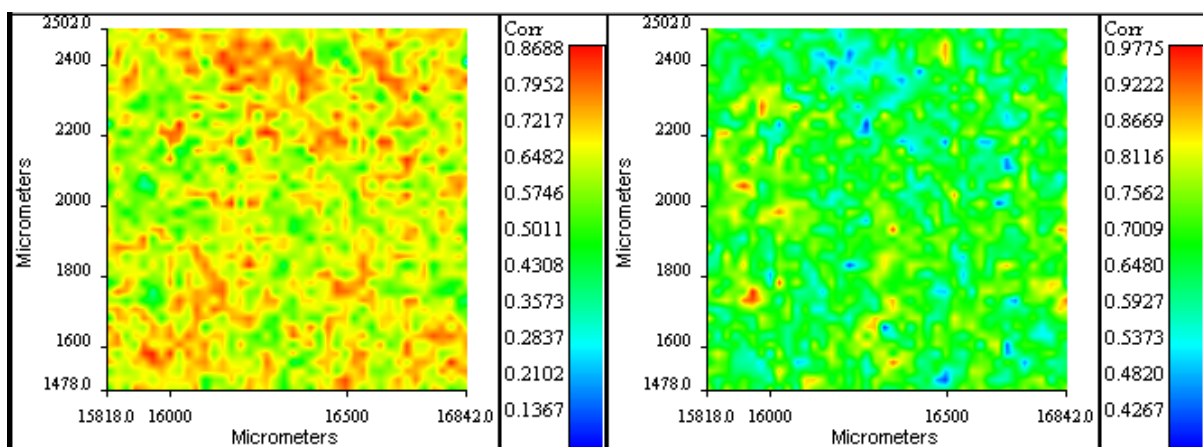


**Figure 6.7** The NIR chemical images (1x1 mm<sup>2</sup>) of a slurry mixed compressed 80:20 w/w of AZD 3409 malate salt: lactose disc. Left image is the spectra correlated by AZD 3409 malate salt standard NIR spectrum. Right is the spectra correlated by the lactose monohydrate standard NIR spectrum.

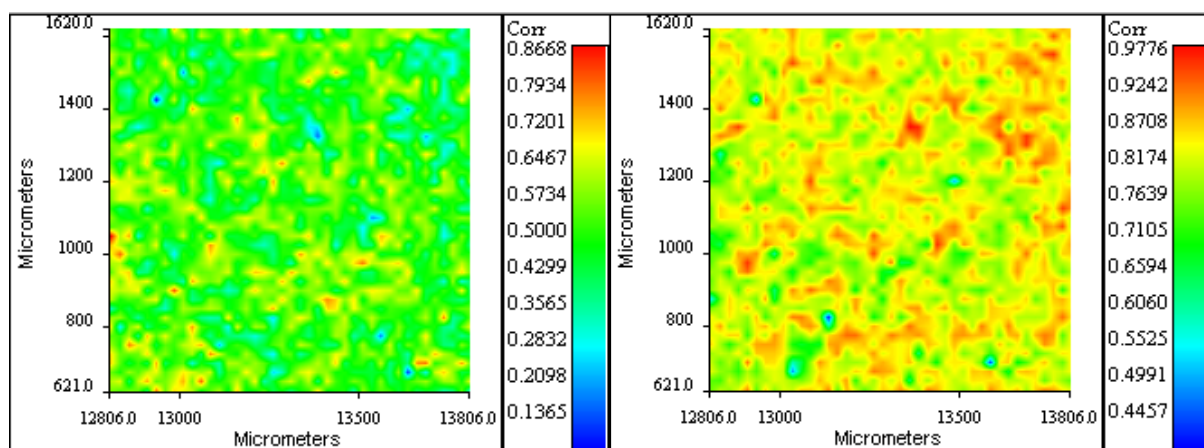


**Figure 6.8** The NIR chemical images ( $1 \times 1 \text{ mm}^2$ ) of a slurry mixed compressed 50:50 w/w of AZD 3409 malate salt: lactose disc. Left image is the spectra correlated by AZD 3409 malate salt standard NIR spectrum. Right is the spectra correlated by the lactose monohydrate standard NIR spectrum.

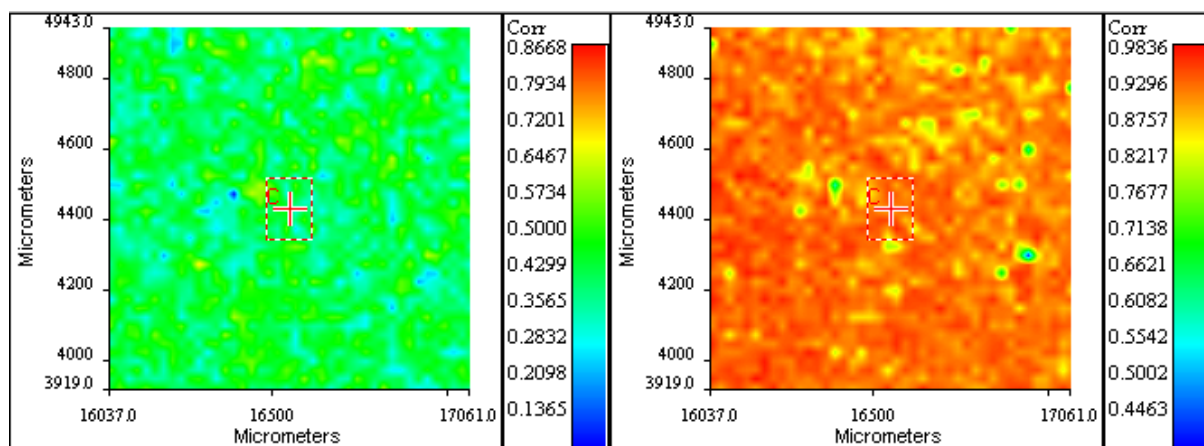


**Figure 6.9** The NIR chemical images ( $1 \times 1 \text{ mm}^2$ ) of a slurry mixed compressed 20:80 w/w of AZD 3409 malate salt: lactose disc. Left image is the spectra correlated by AZD 3409 malate salt standard NIR spectrum. Right is the spectra correlated by the lactose monohydrate standard NIR spectrum.

Before measurements on compressed discs, the ToF-SIMS was first calibrated using the spectra from a clean silicon wafer. The chemical imaging was carried out by rastering the micro-focused primary ion beam over the sample surface and collecting a mass spectrum at every pixel (256x256 pixel array over 400x400  $\mu\text{m}^2$  area) point. A total of 20 scans were made on one disc surface. The pure AZD 3409 malate salt and lactose monohydrate discs were measured first to obtain the mass spectra and find the characteristic ions in the positive and negative mass spectra. The count number of each peak was normalized with total ions. The results were used to examine the ion lists and avoid the possible cross-over. The ion lists used for TOF-SIMS distribution map of AZD 3409 malate salt and lactose monohydrate are displayed in table 6.1 and 6.2.

The heptane slurry mixture compressed discs and simple mixed compressed discs with 80:20, 50:50 and 20:80 w/w of AZD 3409 malate salt and lactose monohydrate were measured with ToF-SIMS chemical imaging. The maps of two materials, the total ions map and the distributions map are presented in Figure 6.10-6.15.

The maps of ToF-SIMS chemical imaging have further confirmed that the slurry mixed compressed discs have a more evenly distribution of AZD 3409 malate salt and lactose monohydrate on surface. There are no large material domains on the slurry compressed disc surface. The surface is hence suitable

for AFM probe force mapping. Because the contact area in AFM probe force measurements is very small, large domains on surface would make the measurements unrepresentative.

**Table 6.1** Ion list for AZD 3409 malate salt used in ToF-SIMS material identification

Positive ion list	Negative ion list
CN	F
C <sub>2</sub> N	CN
C <sub>3</sub> H <sub>7</sub>	NOH
C <sub>4</sub> H <sub>2</sub>	S
C <sub>4</sub> H <sub>3</sub>	HS
C <sub>4</sub> H <sub>4</sub>	H <sub>2</sub> S
C <sub>4</sub> H <sub>8</sub>	CH <sub>3</sub> S
C <sub>5</sub> H <sub>8</sub>	SNH <sub>2</sub>
C <sub>5</sub> H <sub>10</sub>	CH <sub>5</sub> S
C <sub>5</sub> H <sub>4</sub> N	SO <sub>2</sub>
C <sub>5</sub> H <sub>5</sub> N	
C <sub>6</sub> H <sub>8</sub>	
C <sub>2</sub> H <sub>8</sub> N	
C <sub>2</sub> H <sub>9</sub> SN	
C <sub>14</sub> H <sub>12</sub>	
C <sub>15</sub> H <sub>14</sub>	

**Table 6.2** Ion list for lactose monohydrate used in ToF-SIMS material identification

Positive ion list	Negative ion list
Na	C <sub>2</sub> O
C <sub>2</sub> H <sub>5</sub>	C <sub>2</sub> HO
CH <sub>3</sub> O	C <sub>2</sub> H <sub>2</sub> O
C <sub>4</sub> H <sub>9</sub>	C <sub>2</sub> H <sub>3</sub> O
C <sub>4</sub> H <sub>10</sub>	CHO <sub>2</sub>
C <sub>4</sub> H <sub>7</sub> O	C <sub>2</sub> H <sub>3</sub> O
C <sub>3</sub> H <sub>5</sub> O	C <sub>4</sub> H <sub>5</sub> O
C <sub>4</sub> H <sub>5</sub> O	C <sub>4</sub> H <sub>7</sub> O
C <sub>4</sub> H <sub>11</sub> O	C <sub>3</sub> H <sub>5</sub> O
C <sub>6</sub> H <sub>13</sub> O	C <sub>3</sub> H <sub>7</sub> O
	C <sub>5</sub> H <sub>4</sub> O
	C <sub>4</sub> H <sub>7</sub> O
	C <sub>5</sub> H <sub>5</sub> O
	C <sub>5</sub> H <sub>7</sub> O

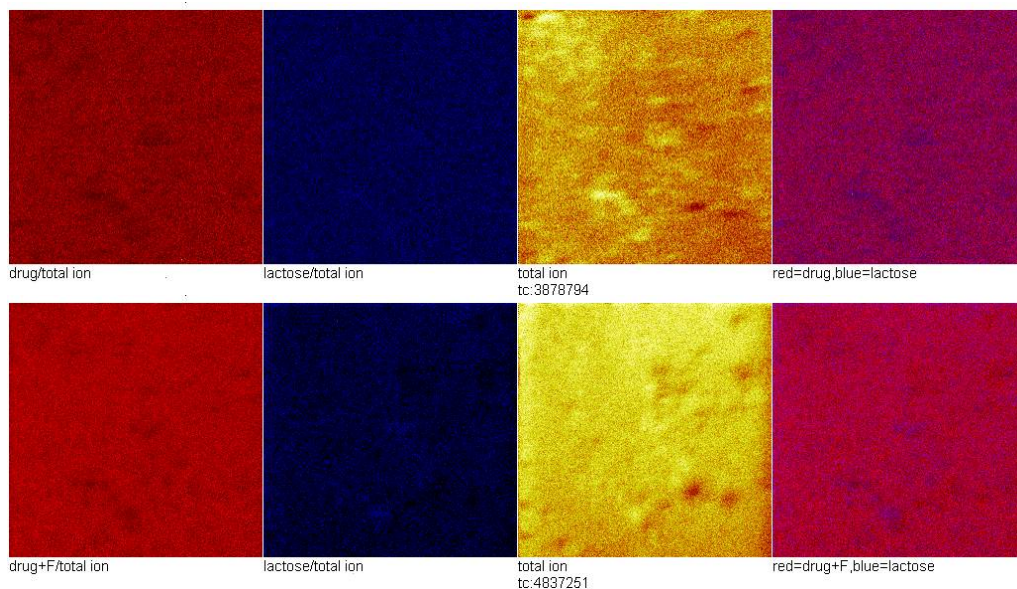


**Figure 6.10** ToF-SIMS 80:20 w/w simple mixed compressed disc distribution maps (scan size 400  $\mu\text{m}$  x 400  $\mu\text{m}$ ). Top four positive ions distribution maps: AZD 3409 malate salt, lactose monohydrate, total ion and cross distribution. Bottom four images are negative ions distribution maps.

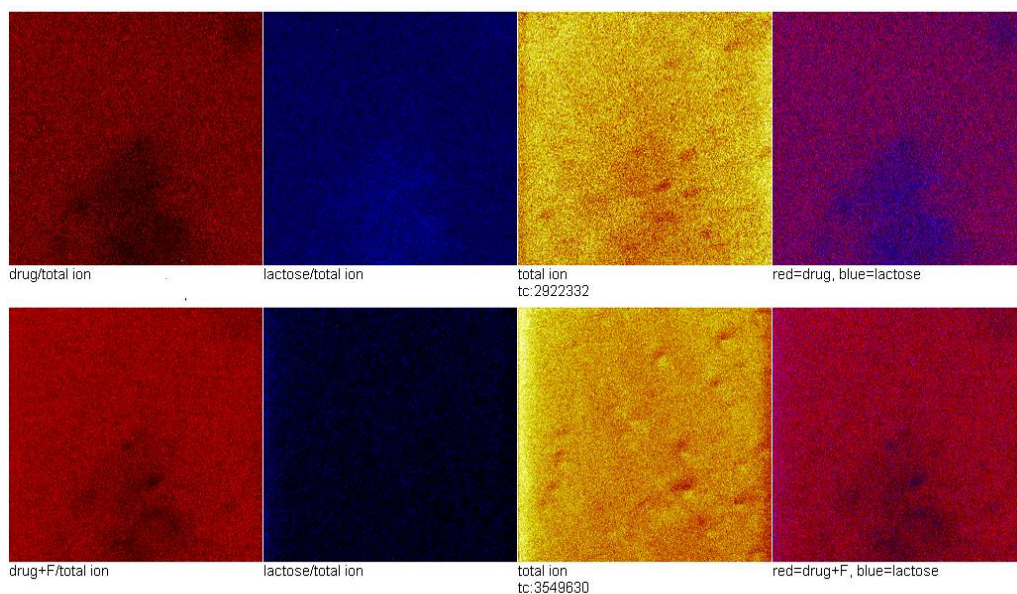


**Figure 6.11** ToF-SIMS 80:20 w/w slurry mixed compressed disc distribution maps (scan size 400  $\mu\text{m}$  x 400  $\mu\text{m}$ ). Top four positive ions distribution maps: AZD 3409 malate salt, lactose monohydrate, total ion and cross distribution. Bottom four negative ions distribution maps.

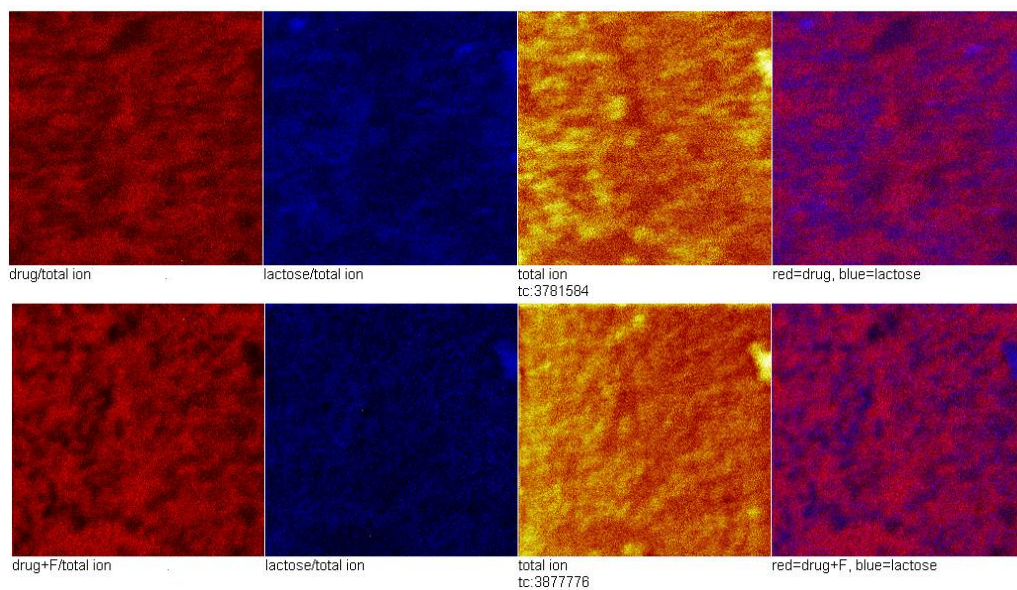


**Figure 6.12** ToF-SIMS 50:50 w/w simple mixed compressed disc distribution maps (scan size 400  $\mu\text{m}$  x 400  $\mu\text{m}$ ). Top four positive ions distribution maps: AZD 3409 malate salt, lactose monohydrate, total ion and cross distribution. Bottom four images are negative ions distribution maps.

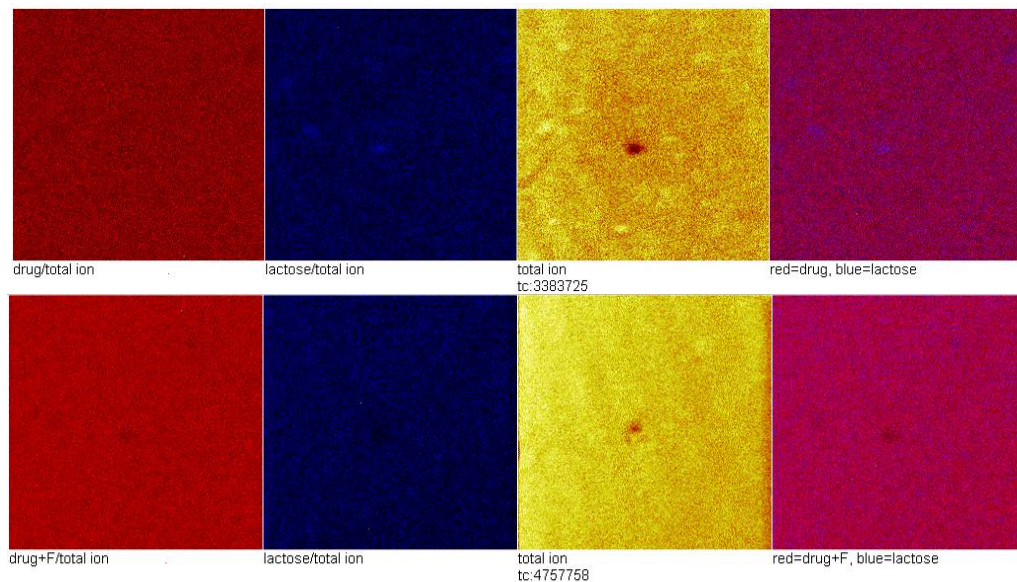


**Figure 6.13** ToF-SIMS 50:50 w/w slurry mixed compressed disc distribution maps (scan size 400  $\mu\text{m}$  x 400  $\mu\text{m}$ ). Top four positive ions distribution maps: AZD 3409 malate salt, lactose monohydrate, total ion and cross distribution. Bottom four images are negative ions distribution maps.

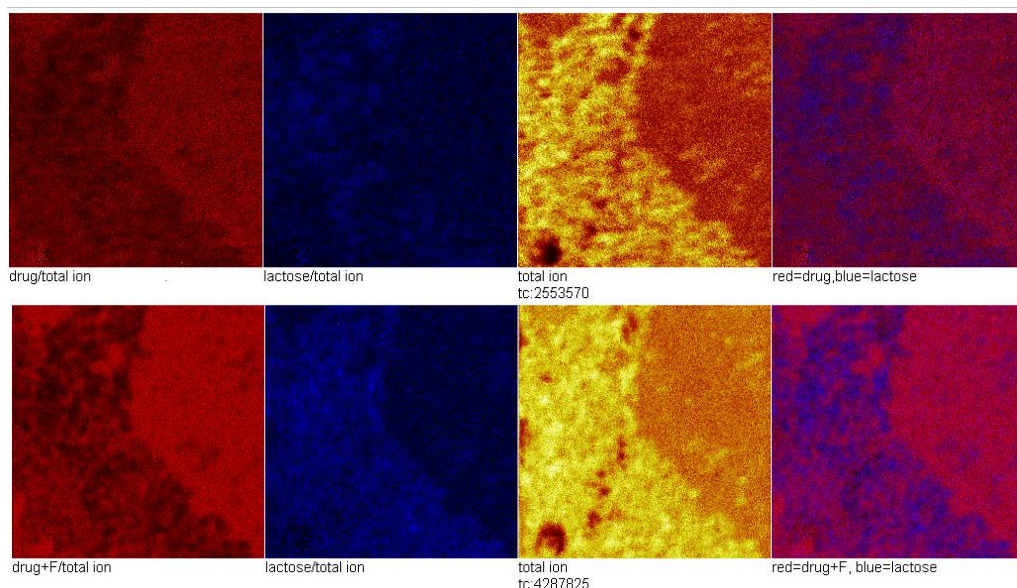


**Figure 6.14** ToF-SIMS 20:80 w/w simple mixed compressed disc distribution maps (scan size 400  $\mu\text{m}$  x 400  $\mu\text{m}$ ). Top four positive ions distribution maps: AZD 3409 malate salt, lactose monohydrate, total ion and cross distribution. Bottom four images are negative ions distribution maps.

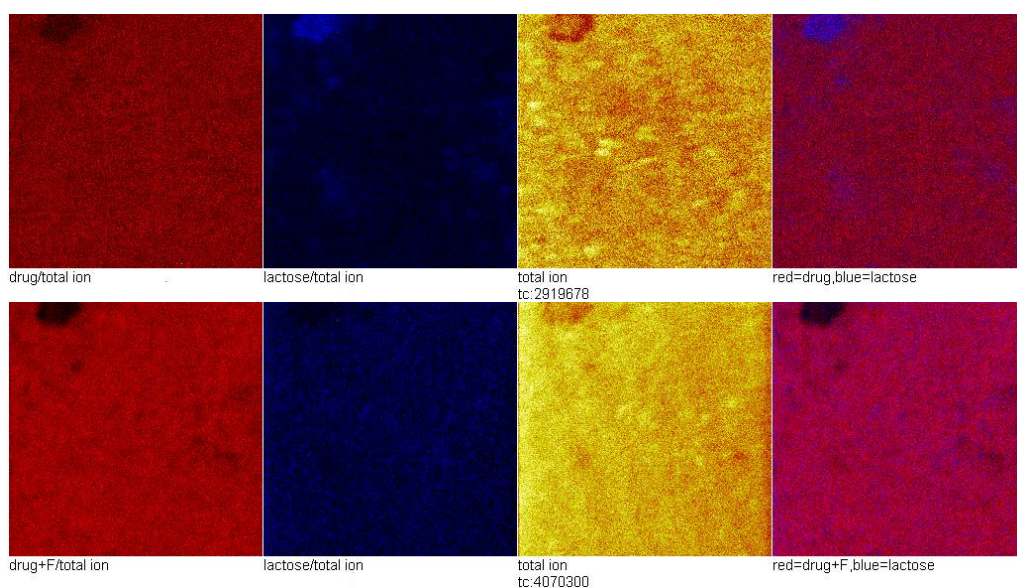


**Figure 6.15** ToF-SIMS 20:80 w/w slurry mixed compressed disc distribution maps (scan size 400  $\mu\text{m}$  x 400  $\mu\text{m}$ ). Top four positive ions distribution maps: AZD 3409 malate salt, lactose monohydrate, total ion and cross distribution. Bottom four images are negative ions distribution maps.

### 6.3.2 Force Mapping on a Binary Model Formulation

The force measurement in force mapping is essentially a spatial mapping version of individual adhesion force measurements. Firstly the AFM tapping images were taken with FESP probes followed by adhesion force measurements on the area. The FESP probe is not the premier choice for tapping mode imaging, but the force mapping needs the sensitivity of FESP probe in adhesion force measurements and the probe should keep at the same position. So it is not possible to change the probe after imaging since even changes of a few microns will lose the pre-determined area (Figure 6.16).

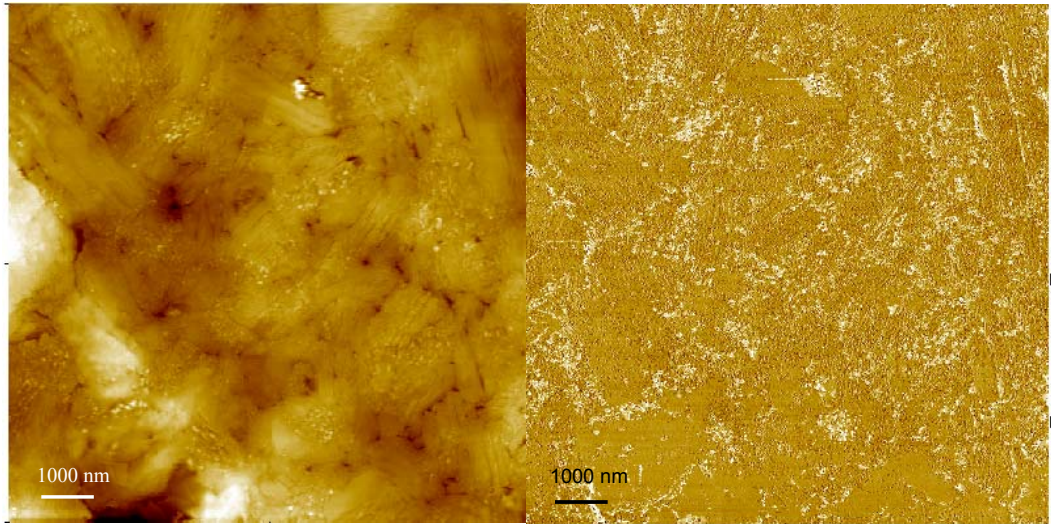


**Figure 6.16** Tapping topography and phase images of 50:50 w/w slurry compressed disc with FESP probe before force measurements. Scan size is  $10 \times 10 \mu\text{m}^2$ .

Then the function of auto force measurements with the Nanoscope controller was used to collect the force-distance curves on the imaging area. In this manner, the movement of probe is more precisely controlled than it in a manual setup. So in the auto run setup, the array of 10 columns multiply 10 rows meant

that a total of 100 force curves were collected. The step size between each column and row was 500 nm so the total force measure area was  $5 \times 5 \mu\text{m}^2$ . The force measurements were designed to allow the classification of materials based on the surface free energy values (Figure 6.17).

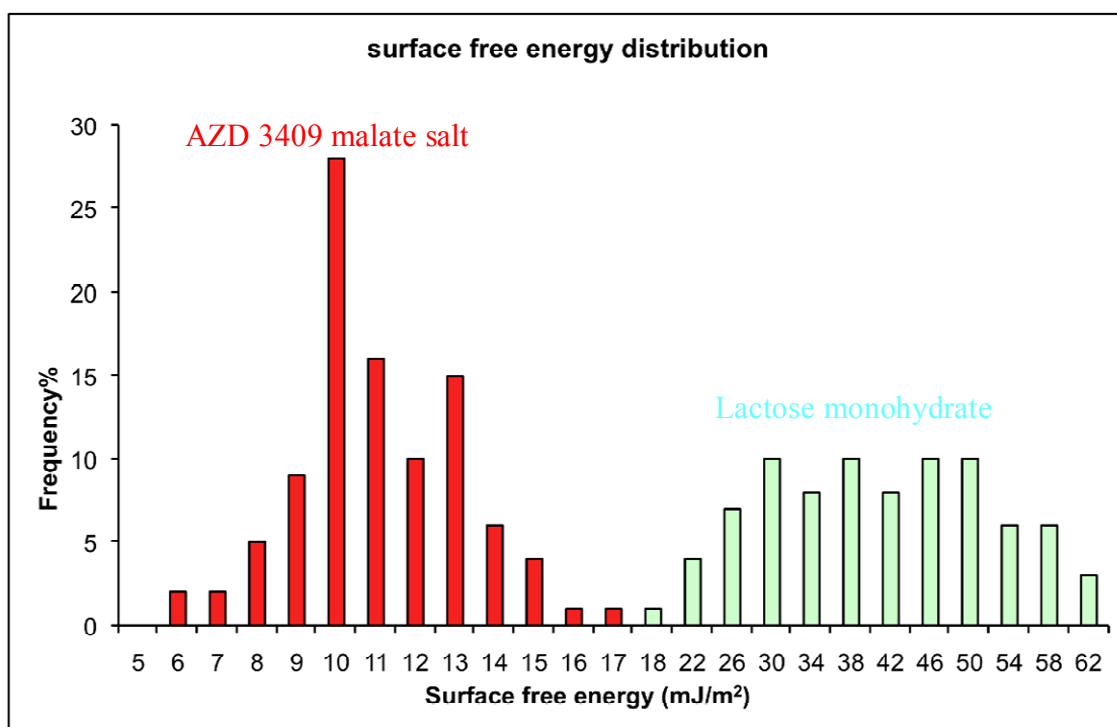


**Figure 6.17** Surface free energy measurements on pure AZD 3409 malate salt and lactose monohydrate discs. 100 surface free energy values were derived from the force-distance curves of each sample. The values were plotted as histogram. The average surface free energy values for AZD 3409 malate salt is  $10.7 (2.2) \text{ mJ/m}^2$ ; for lactose monohydrate is  $38.6 (11.2) \text{ mJ/m}^2$ .

Finally, because the array of surface free energy and tapping image have the same position, the two images could be combined together to create the force map (Figure 6.18). So in the force map, two kinds of information are provided:

in the high resolution topography of measured area, single particles with clear

boundaries can be observed. And the positions of force measurements can be located in the topography image. The particles now can be identified as AZD 3409 malate salt or lactose monohydrate based on their surface free energy values.

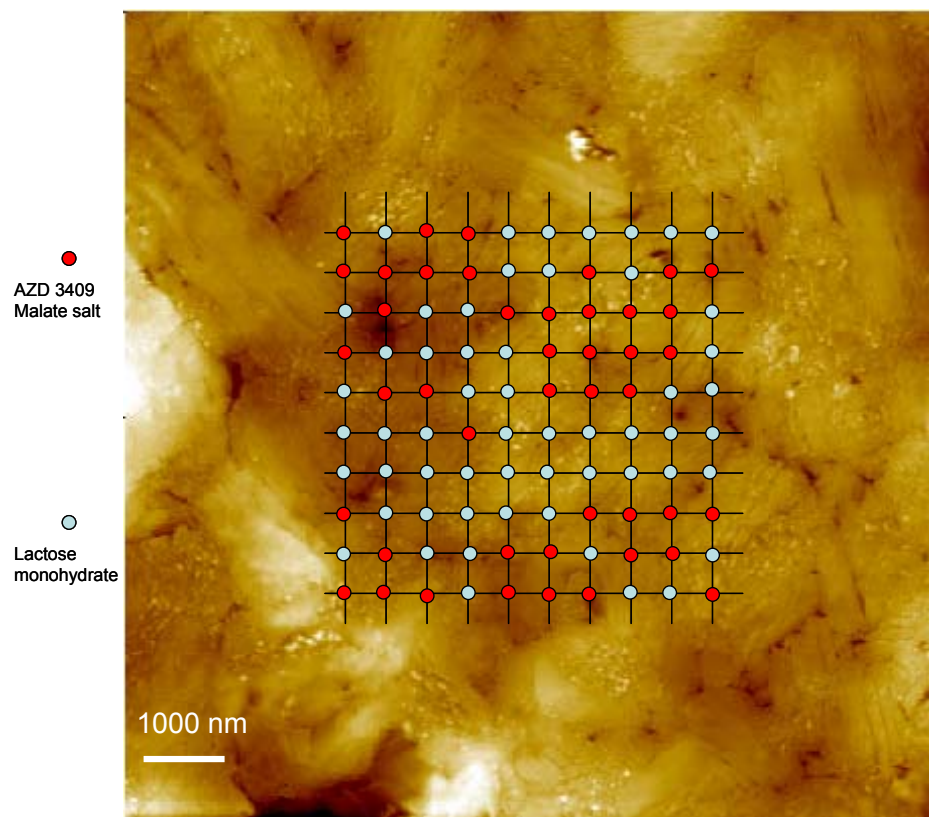


**Figure 6.18** Force map on 50:50 w/w slurry compressed disc. The scan size of tapping topography image is  $10 \times 10 \mu\text{m}^2$  and the scan size of force measurements is  $5 \times 5 \mu\text{m}^2$ . Each position was classified into the two materials present based on its surface free energy value.

The same measurements were made on all three weight ratio discs and the final force maps together with original surface free energy histograms are presented in Figures 6.19-6.21.

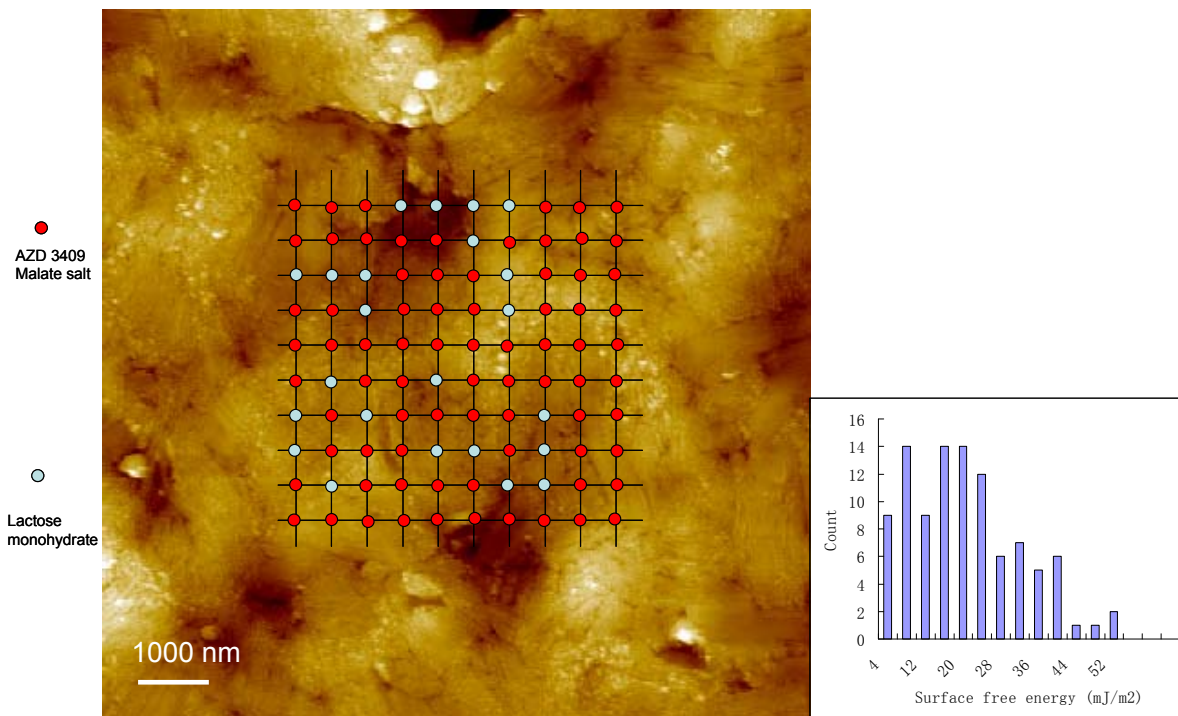


**Figure 6.19** Force map of 80:20 w/w slurry compressed disc. Scan size is  $10 \times 10 \mu\text{m}^2$  and scan size of force measurements is  $5 \times 5 \mu\text{m}^2$ . 100 force measurements were collected.

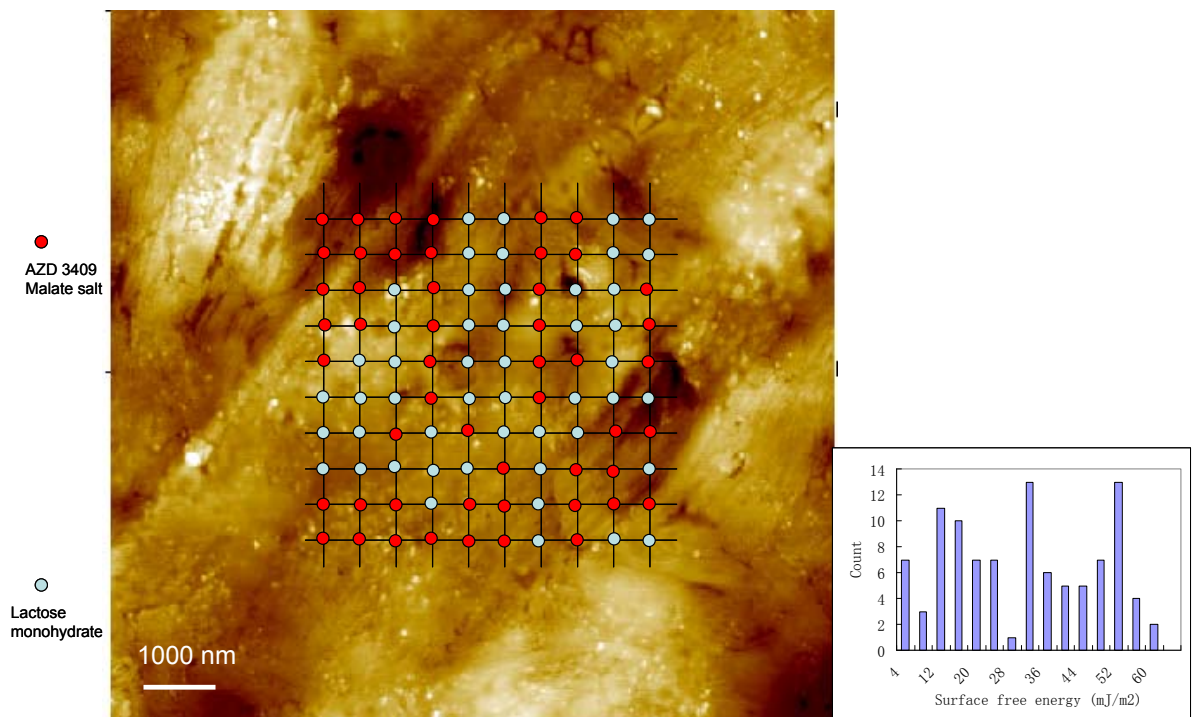


**Figure 6.20** Force map of 50:50 w/w slurry compressed disc. Scan size is  $10 \times 10 \mu\text{m}^2$  and scan size of force measurements is  $5 \times 5 \mu\text{m}^2$ . 100 force measurements were collected.

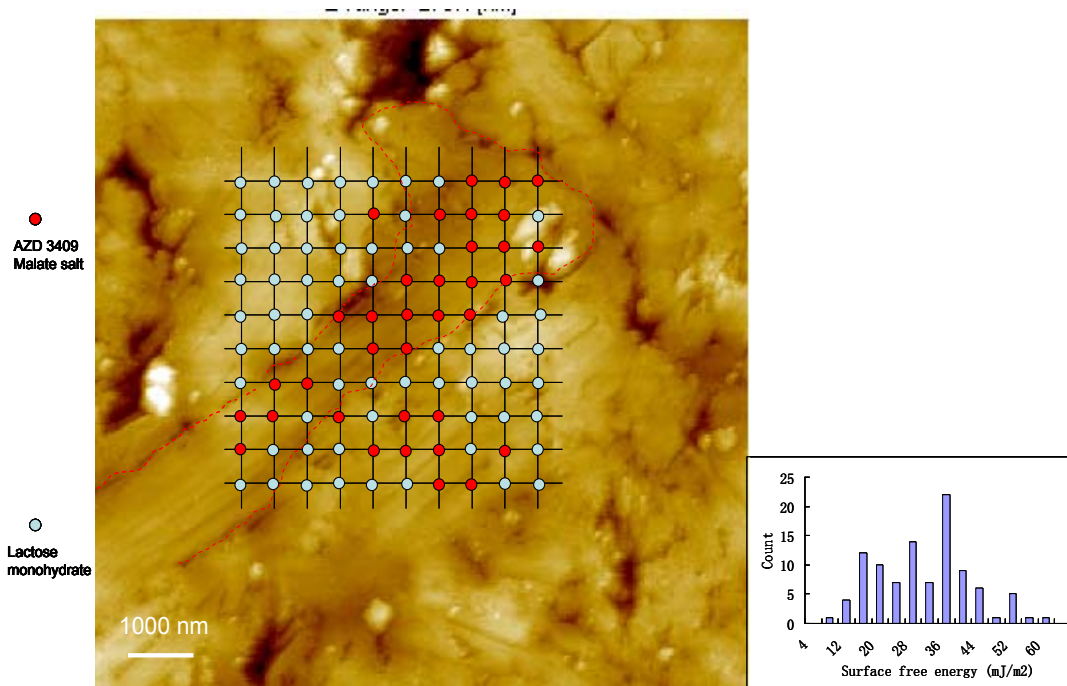


**Figure 6.21** Force map of 20:80 w/w slurry compressed disc. Scan size is 10x10 μm<sup>2</sup> and scan size of force measurements is 5x5 μm<sup>2</sup>. 100 force measurements were collected.

The three force maps clearly reveal the positions of each material in the binary mixtures disc surface with nanometer resolution. It is, for example, clear to see in figure 6.21 where a single large particle of AZD 3409 malate salt is between two lactose monohydrate particles. It is not possible to find such information simply with AFM tapping imaging methods or AFM force measurements alone. The force map can provide the information of distribution for materials with different physical and mechanical properties at high lateral resolution (sub 100 nm). The anhydrous polymorphisms and amorphous regions which are not applicable to mass spectroscopy such as ToF-SIMS [14] can be detected by AFM force mapping method from the differentiation of mechanical properties [15]. And the high resolution of AFM force mapping method can help finding

the amorphous or phase transition regions on single particle surface. It can be applied to investigate the transformation during the processing and stress conditions stability test with tiny amount of materials. Although Raman spectroscopy can also provide material distribution even with polymorphisms information based on the ability of probing lattice vibrations [16], the low lateral resolution (500nm) of normal Raman had limited the applications in chemical imaging. The methods such as tip-enhanced [17] and near-field optical microscopy [18] have improved the resolution of Raman chemical imaging up to 100 nm, but the requirement of monochromatic source of radiation in Raman spectroscopy measurements made this method not applicable for the samples emitting fluorescence scattering. In such case, AFM force mapping method will be a proper replacement.

AFM imaging and force measurements functions have been previously combined. For example, the pulsed force mode (PFM) imaging method and force volume mode can also obtain images based on the differences in adhesions (or mechanical properties) [19, 20]. However, these methods require the samples have relatively flat surfaces and large contrast in mechanical differences in the system. Hence, in most applications these methods were employed for polymer film and biomolecular measurements [21]. The same measurements on slurry compressed discs have been done with pulse force mode imaging method (data not shown). The results, which are poor with low

resolution, indicating that for the binary compressed discs the PFM imaging method cannot contribute much useful information. In addition, the method is a semi-quantity method which does not provide the surface free energy values but only relative magnitude of adhesion forces.

### **6.3.3 Thermal Mapping on a Binary Model Formulation**

Thermal maps were made followed the procedures of the force mapping method. Although, the AN-2 thermal probe used in nano-TA system has a very sharp tip radius, the thermal measurements usually dig a relatively larger hole than the tip radius due to heat transfer into the sample. So the thermal measurements were only made on a few interesting positions.

A tapping mode image taken with AN-2 probe before thermal measurements is presented as Figure 6.22. Clearly several single particles can be observed. The thermal measurements were then carried out at one the single particle in the middle of image.

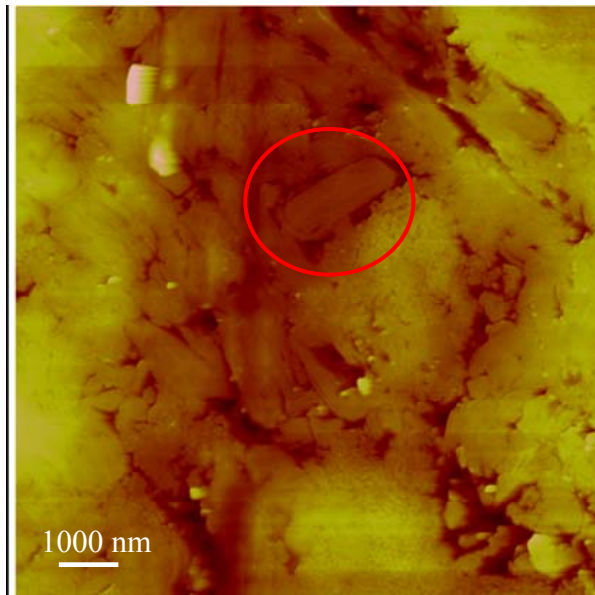


**Figure 6.22** Tapping topography image of 20:80 w/w slurry disc with AN-2 thermal probe before thermal measurements. The single particle which is going to be measured is marked.

After the thermal measurement, the position of the single particle was re-analyzed by tapping mode imaging with an AN-2 thermal probe (Figure 6.23).

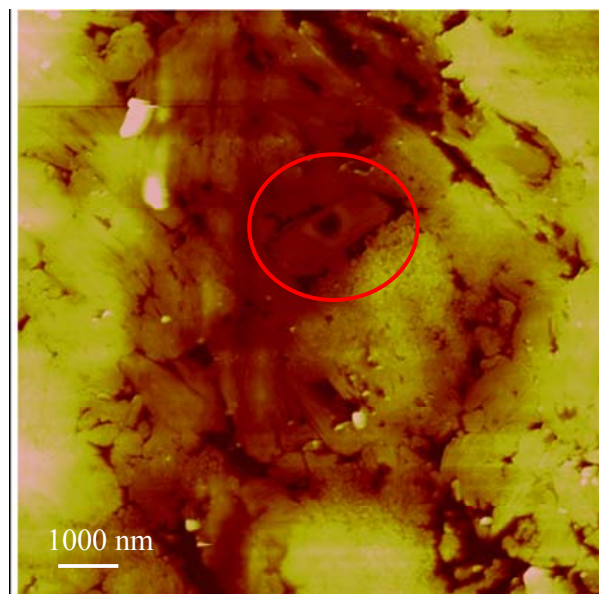


**Figure 6.23** Tapping topography image of a 20:80 w/w slurry disc with an AN-2 thermal probe after thermal measurement. The hole made by

thermal measurement can be seen. The corresponding LTA trace is presented as Figure 6.24.

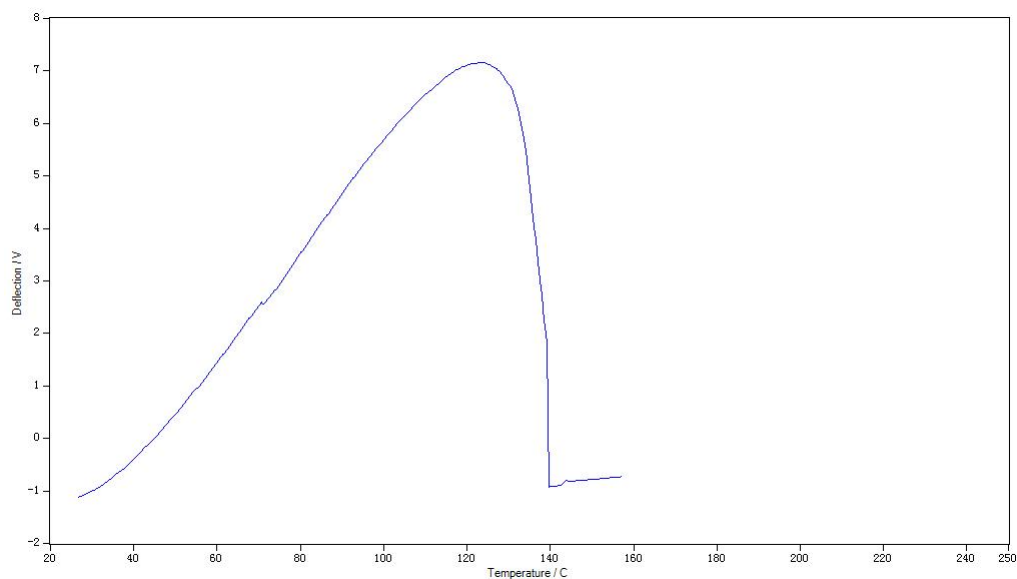


**Figure 6.24** Nano-TA local thermal analysis on the single particle circled in figure 6.22. The melting point temperature is 123.2 °C which indicates the single particle is the AZD 3409 malate salt (See table 5.4).

From the LTA data in Figure 6.24, the highlighted single particle is composed of the AZD 3409 malate salt based on melting point results. The same measurements were made on other positions where both AZD 3409 malte salt and lactose monohydrate were found (Figures 6.25-6.27). As the results in Figure 6.25, two materials are distinguished by their different local thermal analysis results. Each material is clearly identified by its thermal property in binary formulation. Due to the high resolution of AN-2 thermal probe, the positions of materials are located in tapping image as well.

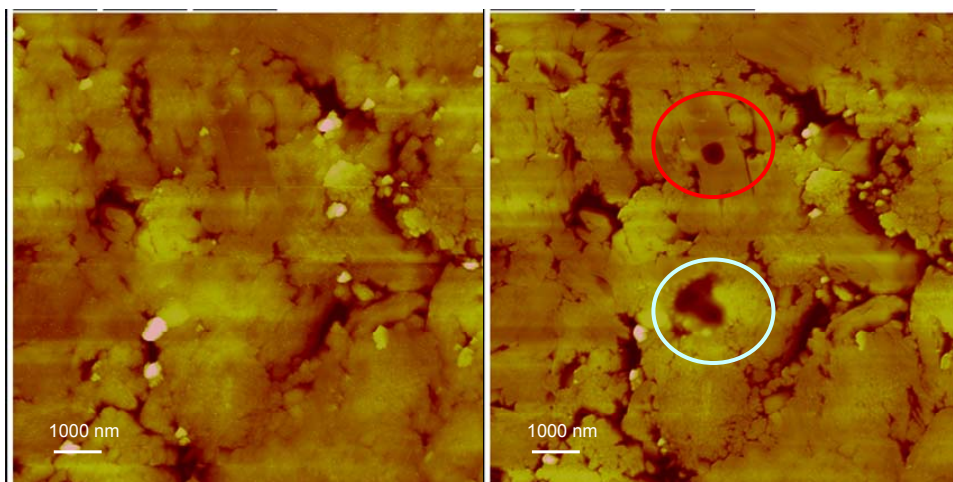


**Figure 6.25** Tapping topography images before (Left) and after (Right) thermal measurements. Nano-TA local thermal analysis show that single particle with red circle is AZD 3409 malate salt (Figure 6.26), while position with light turquoise circle is lactose monohydrate (Figure 6.27).

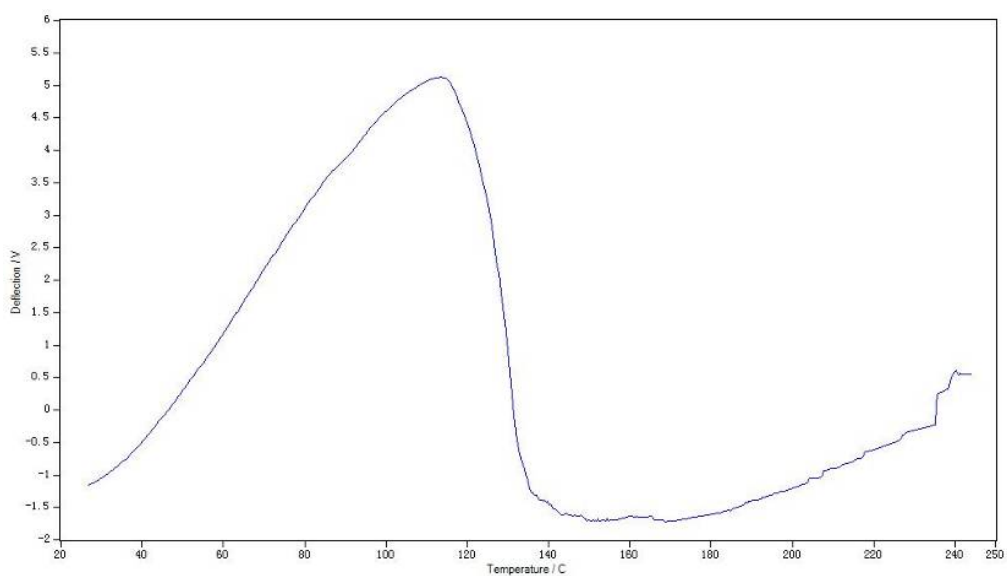


**Figure 6.26** Nano-TA local thermal analysis on the particle with red circle. The melting point temperature is 113.2 °C for AZD 3409 malate salt.

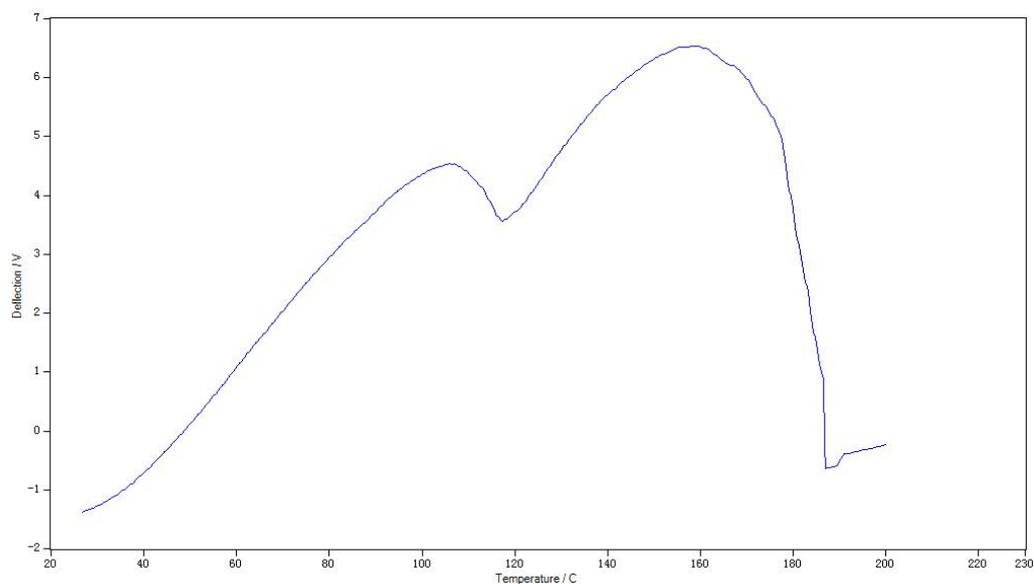


**Figure 6.27** Nano-TA local thermal analysis on the position with light turquoise circle. The melting point temperature is 161.2 °C. While the dehydrate point temperature is found at 106.4 °C.

### 6.3.4 Force and Thermal Correlation Mapping on a Binary Model Formulation

The force measurements were first carried out on the surface of a 20:80 w/w slurry compressed disc. Several positions were selected to obtain force-distance curves based on the criteria of easy recognizable and single particles (Figure 6.28). To cope with the relatively large measurement area in the thermal measurements, 100 force measurements with the FESP probe on each position were taken within a  $1 \times 1 \mu\text{m}^2$  area. The average surface free energy values of 100 measurements were processed for material identification (Table 6.3).

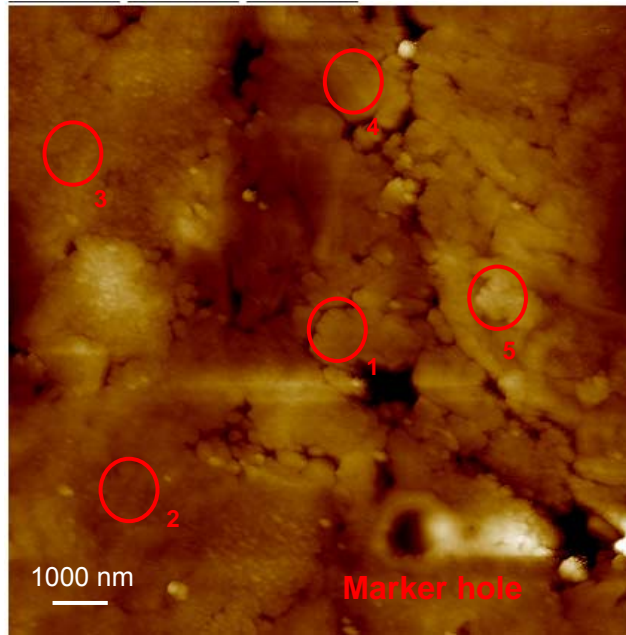


**Figure 6.28** AFM tapping topography image of 20:80 w/w slurry disc with a FESP probe. The marker hole was made with nano-TA thermal measurement early for easy position relocation with tapping imaging. 5 positions were measured with AFM force measurements.

**Table 6.3** Surface free energy values in Figure 6.25 5 measure positions

Unit: mJ/m<sup>2</sup>

Position	Surface free energy values
1	46.0 (12.2)
2	45.8 (14.9)
3	41.6 (10.0)
4	26.0 (3.6)
5	48.8 (15.2)

Considering the results in table 6.3, there are four positions apart from position

No. 4 with high surface free values, which could classify these areas into the range of lactose monohydrate. Position No. 4 has a much smaller surface free energy values than other four positions. But the value is slightly higher than pure AZD 3409 malate salt. The method to obtain the surface free energy at each position may actually exceed the boundaries of the single particle, so lactose monohydrate particles around position No. 4 may contribute to the calculated value, which will skew the average surface energy to a high value.

To examine the possibility that the thermal measurements we carried out are at the same positions. The marker hole was used for relocation the relative positions. They were easily recalled with an AN-2 thermal probe tapping image (Figure 6.29).

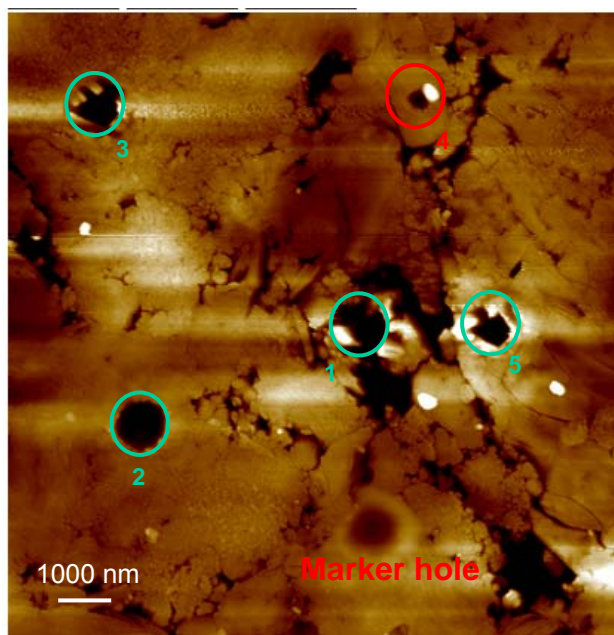


**Figure 6.29** AFM tapping topography image of 20:80 w/w slurry disc with AN-2 Thermal probe. 5 positions were measured with Nano-TA local thermal analysis.

The results of nano-TA local thermal analysis confirm that the single particle at position No. 4 is the AZD 3409 malate salt in terms of its melting point (Figure 6.30).

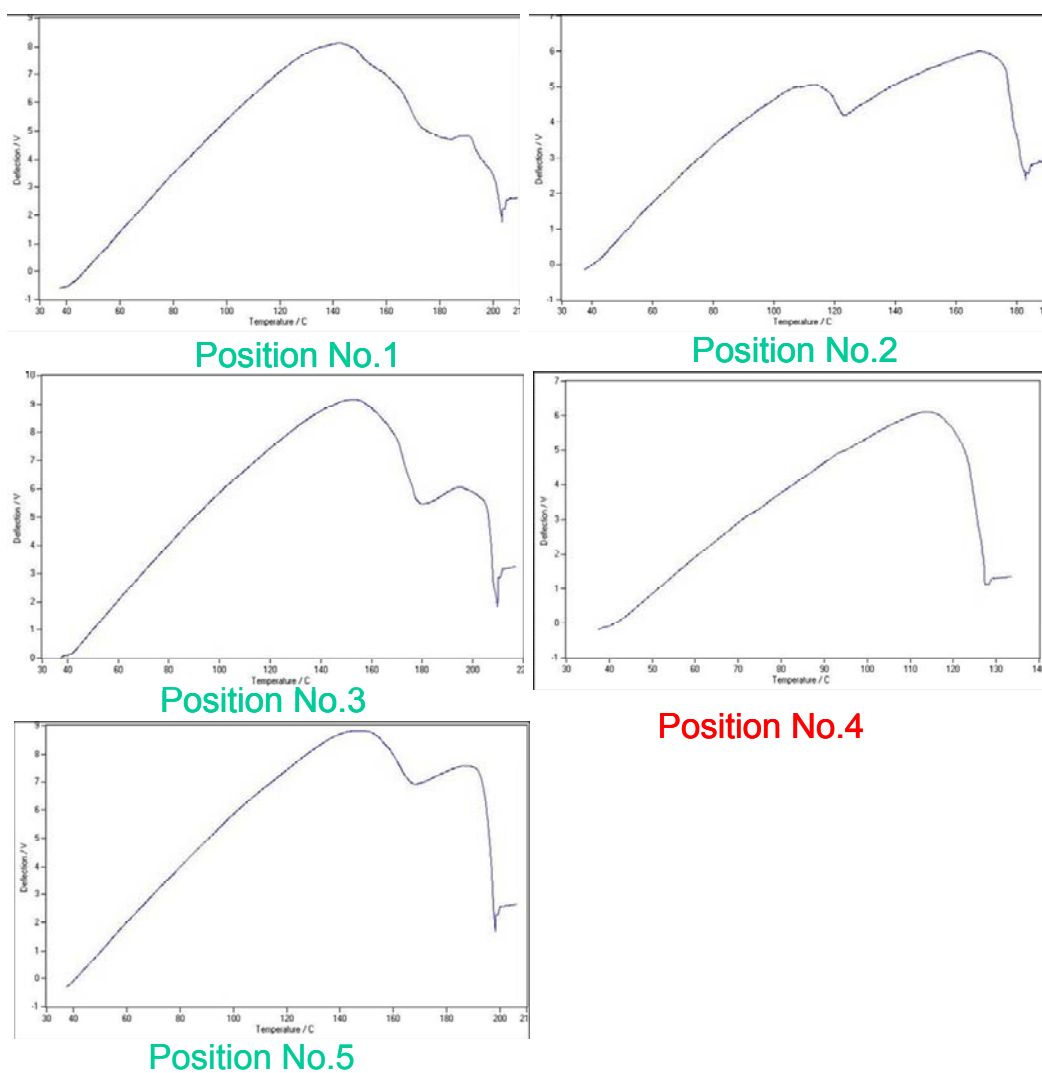


**Figure 6.30** Nano-TA local thermal analysis measurements on 5 positions. At position No.1 dehydration temperature is 141.8 °C, melting temperature is 190.8 °C. At position No.2 dehydration temperature is 111.3 °C, melting temperature is 167.6 °C. At position No.3 dehydration temperature is 152.8 °C, melting temperature is 195.3 °C. At position No.5 dehydration temperature is 149.9 °C, melting temperature is 189.4 °C. At position No. 4 only melting temperature was observed at 113.4 °C.

The attempts to correlate the AFM force measurements and nano-TA thermal measurements have been proved to be successful. In all the measurements, two approaches have provided the same information on material identification. The materials in binary formulation have been visually identified based on the surface free energy values and thermal properties. Those results are broadly consistent with the measurements on pure materials. This proof of principal work could now be extended to more complex formulations and has the potential to be employed in the early stage solid state stability testing to identify the appearance of new species at surface or at solid-solid interfaces.

#### **6.4 General Conclusions**

A model binary formulation of AZD 3409 malate salt and lactose monohydrate has been studied. A heptane slurry method could achieve a more even material distribution both in bulk and surface than simple mixing. This is confirmed by ATR-IR, NIR chemical imaging and ToF-SIMS chemical imaging methods. AFM force measurements and imaging methods have been combined together to obtain the AFM force maps on the model formulation discs. The materials are identified within the discs based on their surface free energy values. Complementary measurements have also been carried out using nano-TA local thermal analysis. The thermal maps help identify the materials based on their thermal properties. The correlation of force measurements and thermal

measurements at the same positions on the model formulation disc have further confirmed the validity of both methods and more importantly provides a new method which can investigate the material distribution with high spatial resolution on solid formulation surface and detect the heterogeneous species appearance and location during the stability testing. In the future, the work could be applied to more complex solid systems to solve the formulation problems with tiny amounts of materials.

## References

1. B. R. Matthews. Regulatory aspects of stability testing in Europe. *Drug Dev. Ind. Pharm.* **25** (1999) 831.
2. J. Wardrop, D. Law, Y. Qiu, K. Engh, L. Faitsch and C. Ling. Influence of solid phase and formulation processing on stability of Abbott-232 tablet formulations. *J. Pharm. Sci.* **95** (2006) 2380.
3. G. G. Z. Zhang, D. Law and E. A. Schmitt. Phase transformation consideration during process development and manufacture of solid oral dosage forms. *Adv. Drug Dev. Rev.* **56** (2004) 371.
4. J. Du and S. W. Hoag. The influence of excipients on the stability of the moisture sensitive drugs aspirin and niacinamide: Comparison of tablets containing lactose monohydrate with tablets containing anhydrous lactose. *Pharm. Dev. Technol.* **6** (2001) 159.
5. M. E. Gil-Alegre, J. A. Bernabeu, M. A. Camacho and A. I. Torres-Suarez. Statistical evaluation for stability studies under stress storage conditions. *II Farmaco* **56** (2001) 877.
6. R. Bate, R. Tren, K. Hess and A. Attaran. Physical and chemical stability of expired fixed dose combination artemether-lumefantrine in uncontrolled tropical conditions. *Malaria J.* **8** (2009) 33.
7. K. Kamada, S. Yoshimura, M. Murata, H. Murata, H. Nagai, H. Ushio and K. Terada. Characterization and monitoring of pseudo-polymorphs in manufacturing process by NIR. *Int. J. Pharm.* **368** (2009) 103.

8. D. E. Bugay. Characterization of solid-state: spectroscopic techniques. *Adv. Drug Dev. Rev.* **48** (2001) 43.
9. A. Belu, C. Mahoney and K. Wormuth. Chemical imaging of drug eluting coatings: combining surface analysis and confocal Raman microscopy. *J. Controlled Release* **126** (2008) 111.
10. B. Chase. Fourier transform Raman spectroscopy. *Microchimica Acta* **93** (1987) 81.
11. N. G. Portney and M. Ozkan. Nano-oncology: drug delivery, imaging, and sensing. *Anal. Bioanal. Chem.* **384** (2006) 620.
12. C. Gendrin, Y. Roggo and C. Collet. Pharmaceutical applications of vibrational chemical imaging and chemometrics: A review. *J. Pharm. Biomed. Anal.* **48** (2008) 533.
13. P. R. Laity, R. E. Cameron. A small-angle X-ray scattering study of powder compaction. *Powder Technol.* **188** (2008) 119.
14. D. E. Bugay. Characterization of the solid-state: spectroscopic techniques. *Adv. Drug Dev. Rev.* **48** (2001) 43.
15. H. G. Brittain. Polymorphism in pharmaceutical solids vol.95. Marcel Dekker, New York, 1999.
16. J. R. Ferraro. Low-frequency vibrations of inorganic and coordination compounds. Plenum Press. New York. 1971.
17. R. M. Stöckle, Y. D. Suh, V. Deckert and R. Zenobi. Nanoscale chemical analysis by tip-enhanced Raman spectroscopy. *Chem. Phys. Lett.* **318** (2000)

131.

18. S. Webster, D. N. Batchelder and D. A. Smith. Submicron Resolution measurement of stress in silicon by near-field Raman spectroscopy. *Appl. Phys. Lett.* **72** (1998) 1478.

19. H. Krottil, T. Stifter, H. Waschipky, K. Weishaupt, S. Hild and O. Marti. Pulsed force mode: a new method for the investigation of surface properties. *Surf. Interf. Anal.* **27** (1999) 336.

20. C. C. Dupont-Gillain and I. Jacquemart. Patterned collagen layers on polystyrene: direct probing using AFM in the adhesion mapping mode. *Surf. Sci.* **539** (2003) 145.

21. N. H. Green, S. Allen, M. C. Davies, C. J. Roberts, S. J. B. Tendler and P. M. Williams. Force sensing and mapping by atomic force microscopy. *Trac-Trends Anal. Chem.* **21** (2002) 64.